

UNIVERSITÀ DEGLI STUDI DI MILANO BICOCCA

Facoltà di Scienze Matematiche Fisiche e Naturali
Dipartimento di Fisica G. Occhialini
Corso di Dottorato in Fisica e Astronomia
XXIV Ciclo A.A. 2009-2011



FAST NEUTRON INSTRUMENTATION FOR BEAM DIAGNOSTICS

Marica Rebai
Matr. 725266

Supervisor: Prof. Giuseppe Gorini
Coordinator of PhD School: Prof. Giberto Chirico

January 20, 2012

*Così tra questa immensità s'annega il pensier mio:
e il naufragar m'è dolce in questo mare.
(G. Leopardi)*

CONTENTS

Abstract	vii
List of papers	xi
1 Introduction	1
1.1 Neutron irradiation experiments	1
1.1.1 Single Event Effects	1
1.1.2 The ISIS neutron source	6
1.1.3 ChipIr beam	9
1.2 Fast neutron monitor for deuterium beams	10
1.2.1 The Padova Research on ITER Megavolt Accelerator (PRIMA): SPIDER and MITICA	11
1.2.2 A first step for the Injector: SPIDER	11
2 Diamond detector prototypes test	19
2.1 Diamond detectors	19
2.1.1 Neutron detection using diamonds	20
2.1.2 Diamond detectors developed: SDD and FDD	21
2.1.3 Time of Flight technique	23
2.2 Time of flight measurements with a SDD	24
2.2.1 The experimental set-up	24
2.3 Biparametric measurements with SDD and FDD	28
2.3.1 The electronic chain	28

2.3.2	The experimental set-up at ISIS	31
2.3.3	Biparametric measurement with the SDD	32
2.3.4	Biparametric measurement with the FDD	34
2.4	Conclusions from diamond detector prototype tests	38
3	Results from diamond detector measurements at high rates	39
3.1	The new detector set-up	39
3.2	Results	41
3.2.1	Energy calibration	43
3.2.2	t_{ToF} vs E_d contour plot and projections	47
3.2.3	Comparison with ROTAX	50
3.2.4	Biparametric analysis	52
3.2.5	Beam profile measurements	55
3.3	Conclusions	57
4	Simulations of neutron production and transport in SPIDER	59
4.1	Simulations of deuterium beam interaction	59
4.1.1	Deuterium implantation profile	60
4.1.2	Ion Energy Loss	61
4.1.3	Ion damage and deuterium concentration in the beam dump	62
4.2	Neutron production in SPIDER beam dump	66
4.2.1	Neutron emissivity	67
4.2.2	Source brightness	69
4.3	Neutron transport in the SPIDER beam dump	71
4.3.1	Simulations	71
4.3.2	Anisotropy and spatial resolution	73
4.3.3	Neutron scattering in the beam dump	75
4.3.4	Neutron scattering in the SPIDER materials	76
4.3.5	Neutron spectrum	79
4.3.6	Contribution of a single beamlet	81
5	The CNESM detection system	85
5.1	Fission Diamond Detectors for SPIDER	85

5.2	Neutron Detection with nGEM: the diagnostic system	87
5.2.1	Gas Electron Multiplier detectors	87
5.2.2	Single and Triple GEM	88
5.2.3	High Voltage and Readout signal	90
5.2.4	The neutron detection principle with GEMs	91
5.3	Simulation of the nGEM cathode	93
5.3.1	Energy deposited in the nGEM gas	94
5.3.2	nGEM detector spatial resolution	98
5.4	Experiments with the first nGEM prototype	100
5.4.1	Experimental set up	100
5.4.2	First prototype results	102
5.4.3	Detector directional response	102
5.5	Comparison between simulation and experimental results . . .	104
6	Conclusions and outlook	107
	Bibliography	121
	Synopsis of attached papers	131
	Acknowledgments	191

Abstract

This thesis concerns the development of fast neutron instrumentation for beam diagnostic. Two kind of detectors have been developed. The first is a diamond detector for fast neutron measurements at the ChipIr beamline of the ISIS spallation neutron source (Didcot, UK). ISIS is a 50Hz-pulsed source in which neutrons are produced by 800 MeV protons interacting on a heavy metal target. The second is a Gas Electron Multiplier (GEM) detector developed for measurements of the neutron emission map in the deuterium beam prototype facility for the ITER fusion reactor under construction at the RFX site (Padova).

Measurements of the so-called Single Event Effects (SEE) are the main application of the ChipIr beamline. SEEs are a potential threat to the robustness of integrated circuits featuring dimensions of tens of nanometers. SEEs occur when a highly energetic particle causes a disruption of the correct operation of an electronic component by striking its sensitive regions. Recent studies have shown that the neutron component above 1 MeV of the cosmic ray radiation is the primary contribution to SEEs for heights < 10 km. In order to evaluate the sensitivity of electronic devices to SEEs, fault-tolerant design techniques must be employed, and extensive analyses are needed to qualify their robustness. Experiments with atmospheric neutrons can be carried out but, due to the low intensity, they require very long periods of data acquisition. Neutron sources represent an opportunity due to the availability

of high intensity fluxes which allow for accelerated irradiation experiments. Recent experiments performed at ISIS on the VESUVIO beamline demonstrated the suitability of ISIS for this kind of application. The new ChipIr beamline will provide an atmospheric-like neutron spectrum with a multiplication factor around 10^8 . A crucial task for ChipIr design is the development of a neutron beam monitor for measurements of the neutron fluence in the MeV energy range. The detector developed in this thesis as a beam monitor for ChipIr is a Single-crystal Diamond Detector (SDD). Neutron detection using diamonds is based on the collection of the electrons/holes pairs produced by the energy deposited in the crystal following neutron reactions with carbon. First tests were performed in 2009 using a prototype SDD. The device features a p-type/intrinsic/metal Schottky barrier structure where the active (intrinsic) detection layer is obtained by chemical-vapour deposition. Both Time of Flight (ToF) only and biparametric (ToF and pulse height) measurements were successfully performed. Measurements were also performed using a Fission Diamond Detector (FDD). A FDD is a device based on a single crystal diamond coupled to a natural uranium converter foil. The biparametric data collection allowed us to distinguish events from ^{235}U , ^{238}U and from carbon break-up reactions inside the diamond. Limitations to quantitative analysis due to the initial choice of detector thickness and instrumental settings were highlighted by the tests.

In a new set of experiments performed in July 2010, April 2011 and October 2011 a new fast neutron detector was tested. The measurements showed three characteristics regions in the biparametric spectra:

- background events of low pulse heights induced by gamma-rays;
- low pulse height events in the neutron ToF region corresponding to E_n in the range 2.4-5.7 MeV which are ascribed to elastic scattering on ^{12}C ;
- large pulse height events in the ToF region corresponding to $E_n > 6$ MeV which are ascribed to $^{12}\text{C}(n, \alpha)^9\text{Be}$ and $^{12}\text{C}(n, n')^3\alpha$ reactions.

Neutron energy information was found to be contained both in the pulse

height and in the ToF data, which suggests that SDDs are good candidate detectors for spectroscopy in fast neutron irradiation experiments. The use of diamond detectors as beam monitors requires further characterization of their response to monoenergetic neutrons.

The second detector developed in this thesis is a nGEM detector able to map the neutron intensity produced in the SPIDER/MITICA beams at the Consorzio RFX in Padova.

The ITER neutral beam test facility under construction in Padova will host two experimental devices: SPIDER, a 100 keV negative hydrogen/deuterium beam, and MITICA, a full scale, 1 MeV deuterium beam. A number of diagnostics will be deployed in the two facilities to qualify the beams. The aim of this thesis was to design a neutron diagnostic for SPIDER, as a first step towards the application of this diagnostic technique to MITICA.

The proposed detection system is called CNESM which stands for Close-contact Neutron Emission Surface Mapping. CNESM is placed right behind the beam dump, as close as possible to the neutron emitting surface. It shall provide the map of the neutron emission on the surface of the beam dump. The latter is a rectangular panel made of water cooled pipes used to stop the incoming beam. The CNESM diagnostic system uses nGEM as neutron detectors. These are Gas Electron Multiplier detectors equipped with a cathode that also serves as neutron-proton converter. The diagnostic was designed on the basis of simulations of the different steps, from the deuteron beam interaction with the beam dump to the neutron detection in the nGEM. The deuteron deposition inside the dump was simulated with the TRIM code in order to provide the deposition profile. Neutron emission occurs via fusion reactions between the deuterium beam and the deuterons implanted in the beam dump surface. Neutron scattering in the beam dump was simulated using the MCNPX code.

The nGEM cathode is at about 30 mm from the beam dump front surface. It is composed of two layers (polyethylene + aluminum) each $\approx 50 \mu\text{m}$ thick. The aluminum layer stops all protons that are emitted from the polyethylene at an angle higher than 40° relative to the normal to the cathode surface.

This means that most of the detected neutrons at a point of the nGEM surface are emitted from the corresponding $40 \times 22 \text{ mm}^2$ beamlet footprint on the dump front surface. The nGEM readout pads (area $20 \times 22 \text{ mm}^2$) will record a useful count rate of $\approx 5 \text{ kHz}$ providing a time resolution of better than 1 s. Each nGEM detector maps the neutron emission from a group of 5×16 beamlets: as many as 16 nGEM detectors would be needed to cover the entire beam dump.

The effect of the directional detector response due to the Al foil is to decrease the FWHM value to about 30 mm. This level of spatial resolution is adequate for unfolding the neutron source intensity from the 2D event map in the nGEM detector. The first nGEM detector prototype was tested at the FNG neutron source in Frascati, where the directional response of the nGEM cathode to neutrons was verified. The successful design of the CNESM neutron diagnostic for SPIDER provides the basis for its application to MITICA ($\times 100$ larger neutron fluxes expected), where it will be particularly useful to resolve the horizontal beam intensity profile.

List of papers

- I. **M.Rebai**, G. Gorini, E. Perelli Cippo, A. Pietropaolo, M. Tardocchi, A. Fazzi, E. Milani, G. Verona Rinati, C. Andreani, R. Senesi, C. D. Frost, E. M. Schooneveld, N. J. Rhodes, R. Bedogni and A. Esposito, “Development of high energy neutron counters for the CHIPIR beamline at ISIS-TS2”, PSI-Report ISSN-Nr. 1019-6447, XIX ICANS Proceeding Conference, Grindelwald - Switzerland, 2010.

- II. A. Pietropaolo, C. Andreani, **M. Rebai**, L. Giacomelli, G. Gorini, E. Perelli Cippo, M. Tardocchi, A. Fazzi, G. Verona Rinati, C. Verona, M. Marinelli, E. Milani, C. D. Frost and E. M. Schooneveld, “Single-crystal diamond detector for time-resolved measurements of a pulsed fast-neutron beam”, *Eur. Phys. Letters*, **92**, 68003, 2010 ¹.

- III. **M. Rebai**, C. Andreani, A. Fazzi, C.D. Frost, L. Giacomelli, G. Gorini, E. Milani, E. Perelli Cippo, A. Pietropaolo, G. Prestopino, E. Schooneveld, M. Tardocchi, C. Verona and G. Verona Rinati, “Fission diamond detector tests at the ISIS spallation neutron source”, *Nucl. Phys B (Proc. Suppl.)*, **215**, 313-315, 2011 ².

- IV. L. Giacomelli, **M.Rebai**, A. Fazzi, E. Perelli Cippo, M. Tardocchi, A.

¹Paper reprinted with permission from the Europhysics letters;
©Europhysics Letters-European Physical Society.

²Paper reprinted with permission from Elsevier B. V .;
©Elsevier B.V.

Andreani, C. Frost, A. Pietropaolo, E. Schooneveld and G. Gorini,
“Diamond detector for high rate monitors of fast neutron beams”, to
appear in Proceedings of the International Workshop on Fusion Neu-
trons and Sub-critical Nuclear Fission (FUNFI) held at Villa Monastero,
Varenna (Italy) September 12-15, 2011.

- V. **M.Rebai**, G.Croci, M. Cavenago, M. Dalla Palma, G. Gervasini, F.
Ghezzi, G. Grosso, F. Murtas, R. Pasqualotto, E. Perelli Cippo, M.
Tardocchi, M. Tollin and G. Gorini,
“A neutron diagnostic for high current deuterium beams”, accepted for
publication in *Rev. Sci. Instrum.*, 2011.
- VI. G. Croci, **M. Rebai** G. Claps, M. Cavenago, M. Dalla Palma, G. Ger-
vasini, G. Grosso, F. Murtas, R. Pasqualotto, E. Perelli Cippo, M.
Tardocchi, M. Tollin, G. and Gorini,
“nGEM neutron diagnostic for high power deuterium beams”, submit-
ted to *Journ. of Instrum.*, December 2011.

Papers not included in this thesis

- I. L. Giacomelli, C. Andreani, A. Fazzi, C.D. Frost, G. Gorini, E. Perelli
Cippo, A. Pietropaolo, **M. Rebai**, H. Schuhmacher, M. Tardocchi, C.
Verona, G. Verona Rinati and A. Zimbal,
“Diamond detectors for fast neutron irradiation experiments”, *Nucl.*
Phys B (Proc. Suppl.), **215**, 242-246, 2011.
- II. A. Pietropaolo, C. Andreani, **M. Rebai**, L. Giacomelli, G. Gorini, E.
Perelli Cippo, M. Tardocchi, A. Fazzi, G. Verona Rinati, C. Verona,
Marco Marinelli, E. Milani, C. D. Frost and E. M. Schooneveld,
“Fission diamond detectors for fast neutron ToF spectroscopy”, *Eur.*
Phys. Letters, **94**, 62001, 2011.
- III. G.Croci, **M.Rebai**, M.Dalla Palma, G.Gervasini, G.Grosso, F.Murtas,
R.Pasqualotto, E.Perelli Cippo, M.Tardocchi, M.Tollin and G.Gorini,
“A new GEM based neutron diagnostic concept for high flux neutron

beam”, to appear in Proceedings of the International Workshop on Fusion Neutrons and Sub-critical Nuclear Fission (FUNFI) held at Villa Monastero, Varenna (Italy) September 12-15, 2011.

- IV. **M. Rebai**, L. Giacomelli, C. Andreani, A. Fazzi, C. D. Frost, E. Perelli Cippo, A. Pietropaolo, N. Rhodes, M. Tardocchi, E. Schooneveld and G. Gorini,
“Diamond detector for beam monitors of fast neutrons at spallation sources”, submitted to *Journ. of Instrum.*, December 2011.
- V. G. Croci, **M. Rebai**, M. Dalla Palma, G. Gervasini, G. Grosso, F. Mur-
tas, R. Pasqualotto, E. Perelli Cippo, M. Tardocchi, M. Tollin and G.
Gorini,
“A new GEM based neutron diagnostic concept for high power deute-
rium beams”, accepted by *IEEE Nucl. Sci. Symp. Proc. Sup.*, 2011.

Chapter 1

Introduction

This thesis concerns the development of fast neutron instrumentation for beam diagnostic. Two kind of detectors have been developed. The first is a diamond detector for fast neutron measurements at the ChipIr beamline of the ISIS spallation neutron source (Didcot, UK). ISIS is a 50Hz-pulsed source in which neutrons are produced by 800 MeV protons interacting on a heavy metal target. The second is a Gas Electron Multiplier (GEM) detector developed for measurements of the neutron emission map in the PRIMA deuterium beam prototype facilities for the ITER fusion reactor under construction at the RFX site (Padova). The ChipIr and PRIMA projects, their motivations and objectives, and their neutron measurement requirements are presented in this chapter.

1.1 NEUTRON IRRADIATION EXPERIMENTS

1.1.1 SINGLE EVENT EFFECTS

Electronic devices are exposed to various types of radiation, such as energetic α particles, protons, neutrons and muons. The radiation may produce effects in electronics with consequences from temporary loss of data (*soft* errors) to catastrophic failure (*hard* errors). These effects in microelectronics are called Single Event Effects (SEEs)([1][2][3]). As the name implies a sin-

gle event effect is due to a single radiation event. The most common type of radiation-induced error is the *soft* error. The error is *soft* when the device (e.g. a memory) is not permanently damaged, and will store new data correctly. Soft errors include many types of different failure modes. In the commercial microelectronics devices for ground application the most common soft error is the Single Event Upset (SEU). SEUs are errors in which an individual memory component is directly corrupted by radiation. It consists of a flip in the logic state of a single bit.

Type of radiation-induced SEEs

The terrestrial environment is dominated by two different mechanisms (alpha particles and cosmic rays) that generate (directly or as secondary reaction products) energetic ions responsible for inducing soft errors. The magnitude of the disturbance an ion causes depends on the Linear Energy Transfer (LET) of that ion. The LET is defined as $LET = \frac{dE}{dx} \cdot \frac{1}{\rho}$ where dE/dx is the energy loss in the material and ρ its density. The value of the LET, usually expressed in $\text{MeV} \cdot \text{cm}^2/\text{mg}$ units depends on the charge/mass of the ion passing in matter, its energy and on the material. Typically, more massive and energetic particles in denser materials have the highest LET. The reverse-biased junction is the most charge-sensitive part of a circuit. When the ionization track traverses or comes close to the depletion region, carriers are rapidly collected by the electric field creating a large current/voltage transient at that node. However, the collected charge is only a part of the problem: the device sensitivity to this excess charge needs to be taken into account. This sensitivity depends primarily on the node capacitance, operating voltage, and the strength of feedback transistors [4]. The rate at which soft errors occur is called the Soft Error Rate (SER). The unit of measure commonly used with SER and other *hard* reliability mechanisms is the Failure In Time (FIT). One FIT is equivalent to one failure in 10^9 device hours. Soft errors have become a huge concern in advanced computer chips because, if uncorrected, they produce a failure rate which is higher than all the other

reliability mechanisms combined. As an example, taken from [5] a typical failure rate for a hard reliability mechanism (such as gate oxide breakdown) is about 1/50 FIT; the aggregate failure rate is typically in the 50/200 FIT range. Without mitigation, the SER can easily exceed 50 000 FIT/chip.

Soft errors due to α particles and neutrons are a growing concern for integrated circuits as the technology scaling tends to decrease the cell dimension and the operating voltage [4]. α particles were shown to be the dominant cause of soft errors in DRAM devices [6]. The most common sources of α particles are from the naturally occurring ^{238}U , ^{235}U , and ^{232}Th . These impurities emit α particles at specific discrete energies over a range from 4 to 9 MeV. When an α particle travels through a material, it loses its kinetic energy. In silicon, the range for a 10-MeV α particle is $<100\ \mu\text{m}$. There are two fundamental approaches to reducing the SER from α particles in integrated circuits: purification of all production materials and methods that reduce the probability that α particles emitted from impurities will reach the sensitive devices. If the manufacture of the electronic is purified, the contribution to SEEs due to α particles can be reduced substantially. The SER is, under these conditions, dominated by cosmic background radiation.

The cosmic radiation has a galactic origin. When it interacts with the Earth atmosphere a secondary cascade of particles is produced. At the sea level particle the flux is composed mainly of neutrons, protons, muons and pions, see Figure 1.1. Because of their intense flux and high LET, neutrons represent the most important part of cosmic radiation producing single event upsets. The cosmic differential neutron flux is shown in Figure 1.2 [7]: above 1 MeV at the sea level the neutron flux is $\approx 20\ \text{n/cm}^2/\text{h}$.

Neutron-induced SEEs

Neutrons, being uncharged, do not directly generate ionization in silicon, but they interact elastically and inelastically with the nuclei in the chip material producing charge particles. At high energies (in the MeV region), inelastic

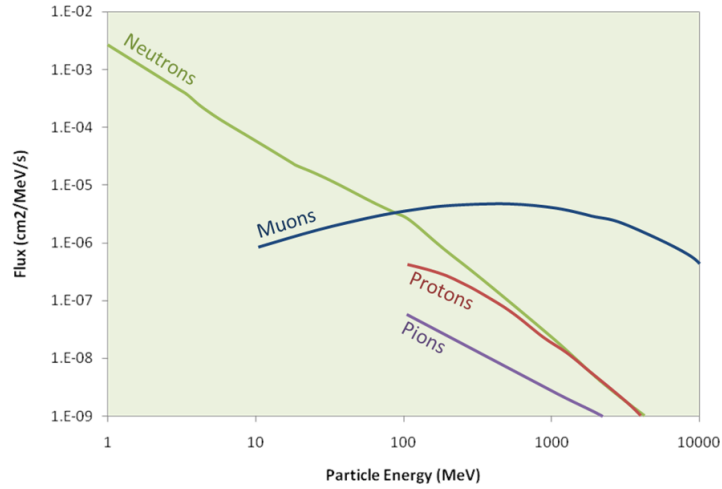


Figure 1.1: Comparison between the neutron, proton, muon and pion flux at sea level. The neutron flux is the most intense.

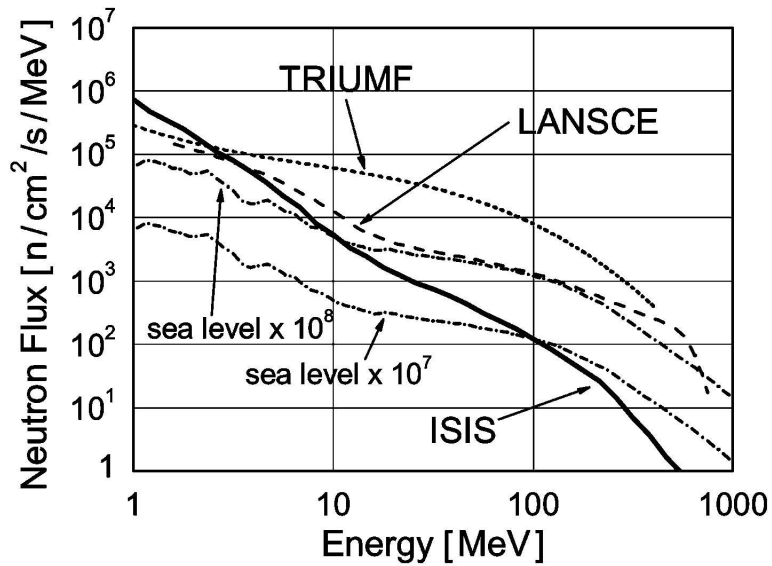


Figure 1.2: Neutron flux above 1 MeV in different neutron facilities compared with the atmospheric one [7].

collisions are more effective and may lead to a series of direct reactions, called intranuclear cascades, which are characterized by the ejection of individual nucleons and heavy ions that more likely induce SEE into the device (Figure 1.3). The most important reactions due to high energy neutrons are reported

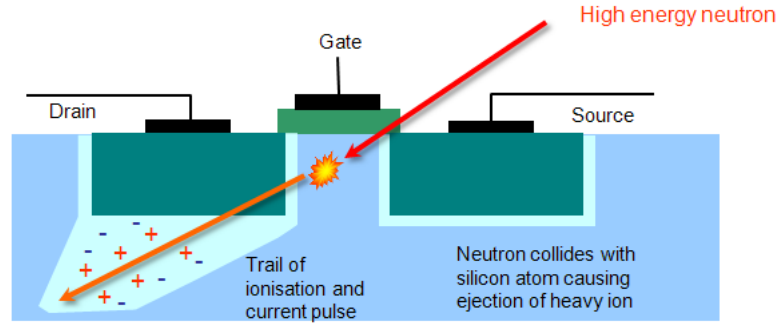


Figure 1.3: High energy neutron interaction in an electronic chip. An ionizing charge particle is produced by elastic or inelastic reaction on silicon atoms. The collected charge by the transistor may produce a soft error.

in Table 1.1.

Reaction product	Energy Threshold [MeV]
$^{25}\text{Mg} + \alpha$	2.75
$^{28}\text{Al} + \text{p}$	4.00
$^{27}\text{Al} + \text{D}$	9.70
$^{24}\text{Mg} + \text{n} + \alpha$	10.34
$^{27}\text{Al} + \text{n} + \text{p}$	12.00
$^{26}\text{Mg} + {}^3\text{He}$	12.58
$^{21}\text{Ne} + 2 \alpha$	12.99

Table 1.1: Reaction products and thresholds for the $\text{n} + {}^{28}\text{Si}$ reaction.

How can we investigate SEEs?

Unlike α particles, the cosmic neutron flux at the chip cannot be reduced significantly e.g. by shielding, keep-out zones, or high purity materials. Cosmic

ray SER must therefore be dealt with by reducing the device sensitivity, either by design or process modifications. Fault-tolerant design techniques are employed, and extensive analyses are needed in order to qualify the robustness of the devices and systems. Experiments with atmospheric neutrons at different altitudes can be carried out, but due to low intensity, they require very long periods of data acquisition. Therefore, neutron sources represent an opportunity due to the availability of high intensity fluxes, which allow for accelerated irradiation experiments. Dedicated facilities are available all around the world, such as LANSCE [8] and TRIUMF [9], in order to investigate the SEEs incidence on chips. In Figure 1.2 the atmospheric neutron flux is compared to neutron facilities spectrum. LANSCE is a multidisciplinary facility for science and technology. At the Los Alamos Meson Physics laboratory a 800 MeV high-power linear accelerator is used to accelerate both protons and negative hydrogen ions with pulsed beam. A neutron spectrum which is rather similar to that of neutrons produced in the atmosphere by cosmic rays, but with a neutron flux 10^8 times higher than the natural one at sea level.

Irradiation tests of semiconductor devices are also performed at the Neutron Irradiation Facility (NIF) of TRIUMF, Vancouver, Canada. NIF is mainly dedicated to testing avionics and ground-based electronic systems. The neutrons are produced by an intense proton beam from a 500 MeV cyclotron, striking an aluminum beam stop immersed in a cooling water tank. NIF has an energy spectrum well matched to the atmospheric one, although somewhat softer than the one at LANSCE. A dedicated beam line for chip irradiation experiments at the ISIS spallation neutron source, named ChipIr, is under construction, [10]. The present ISIS neutron spectrum above 1 MeV is reported in Figure 1.2 [7].

1.1.2 THE ISIS NEUTRON SOURCE

As said before, ISIS [11] is a pulsed neutron source sited at the Rutherford Appleton Laboratory (RAL), Didcot (UK) (Figure 1.4), and has been used so far for condensed matter studies. Neutrons are produced by proton-



Figure 1.4: Photo of the ISIS spallation neutron source area, Didcot, UK.

induced spallation on a Tungsten-Tantalum target. Protons are produced in two bunches, 70 ns wide and 322 ns apart (Figure 1.5), and are accelerated through a Linac and a synchrotron up to 800 MeV, with a frequency of 50 Hz. Neutrons are produced in two target stations: TS-1 (40 Hz) is the older one and it is equipped with 26 beam lines, TS-2 (10 Hz) was built in 2009 and is the target at which ChipIr beam line will be installed. A schematic view of the ISIS-TS1 is reported in Figure 1.6.

After neutrons are produced in the target, they are moderated and they are focused into the various beam lines. The nature of the moderators is different from one beamline to another so that they provide a neutron spectrum specific for each beamline. For example, the VESUVIO beamline moderator is made with a 2 cm thick, 300 K liquid water layer, thus providing a neutron spectrum which is sub-moderated. The VESUVIO beam line is commonly employed for condensed matter studies, exploiting neutrons in the epithermal region (above 1 eV). The VESUVIO neutron spectrum is shown in Figure 1.7. The spectrum above 1 MeV features a $1/E^\alpha$ characteristic, with α equal to about 0.9 [12]. The VESUVIO spectrum integrated above 10 MeV yields $7.86 \cdot 10^4 \text{ n} \cdot \text{cm}^{-2}\text{s}^{-1}$ according to MCNP simulations. Recent experiments performed at the VESUVIO beam line demonstrated the suitability of ISIS for SEEs experiments and motivated the construction of a dedicated beam-

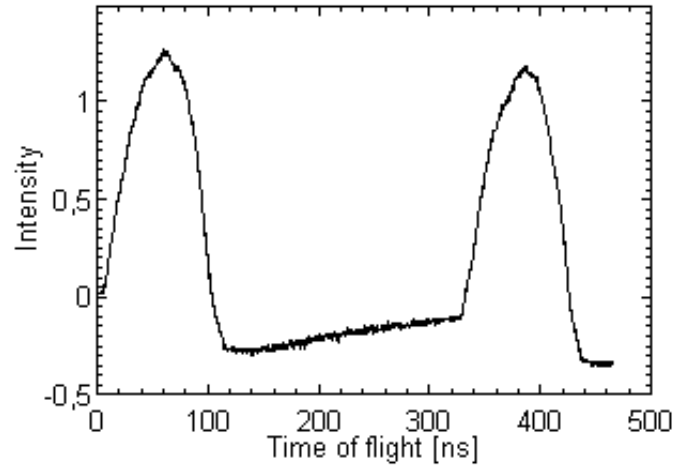


Figure 1.5: The proton bunch profile, the bunch are 60 ns wide and 322 ns apart. Neutron will be produced with the same temporal structure.

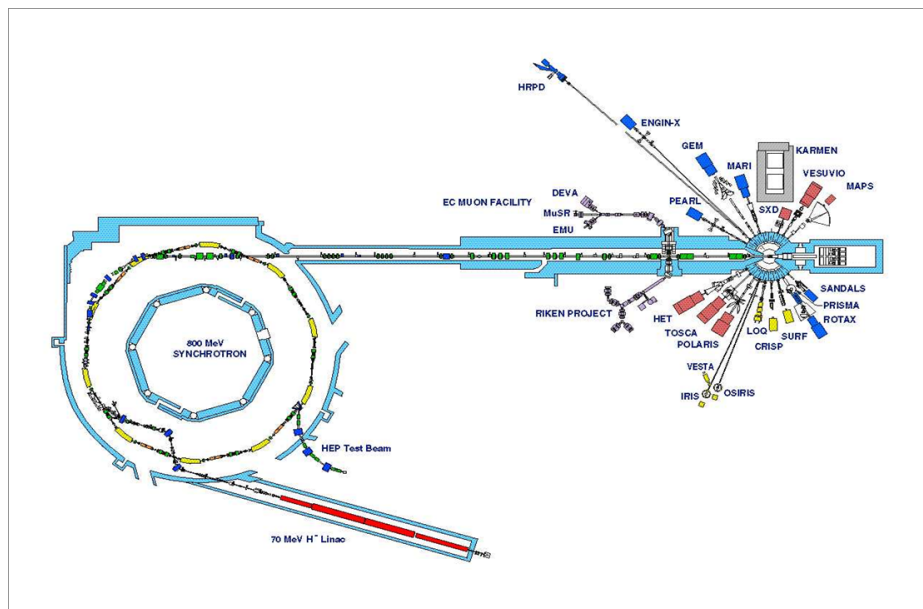


Figure 1.6: Schematic view of the ISIS facility, including the synchrotron, the extractor and the beam lines.

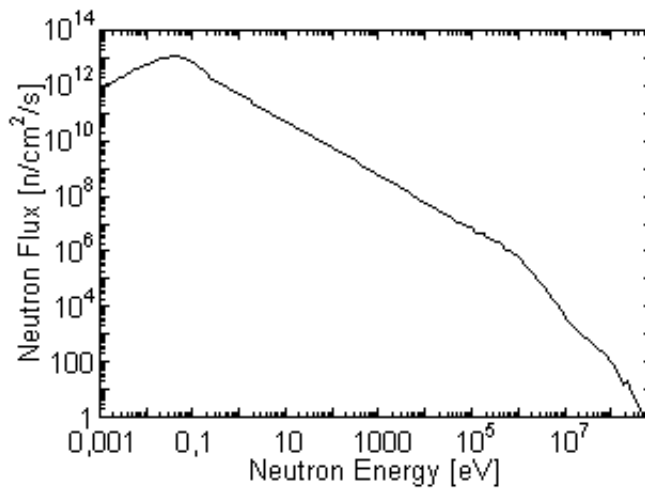


Figure 1.7: VESUVIO neutron spectrum simulated with MCNPX [7].

line: ChipIr.

1.1.3 CHIPIR BEAM

The ChipIr construction was finally approved for construction in 2010 [13]. A CAD model of the beam line is reported in Figure 1.8 [10]. The target is placed in the left part of the figure, under the biological shielding shown as a white cylinder. Neutrons are collimated in the target using a beryllium reflector, and then they are lead to the beam line. The blockhouse (experimental hall) is shown in green. Behind the blockhouse is the beam stop (in purple). The neutron spectrum of ChipIr will be different from the *common* ISIS neutron spectra, shown in Figure 1.2 and 1.7. It will be optimized in order to match the shape of the atmospheric neutron spectrum in the MeV region. In particular, a thermal neutron filter will be used to remove this component from the beam. ChipIr will have a special composite moderator that sits within a channel cut out of the current beryllium reflector. The spectrum will be optimized using special filters in order to better reproduce the atmospheric neutron field. ChipIr will provide a flux above 1 MeV equal to $1.49 \cdot 10^7 \text{ n} \cdot \text{cm}^{-2} \cdot \text{s}^{-1}$. That means 150 times more intense

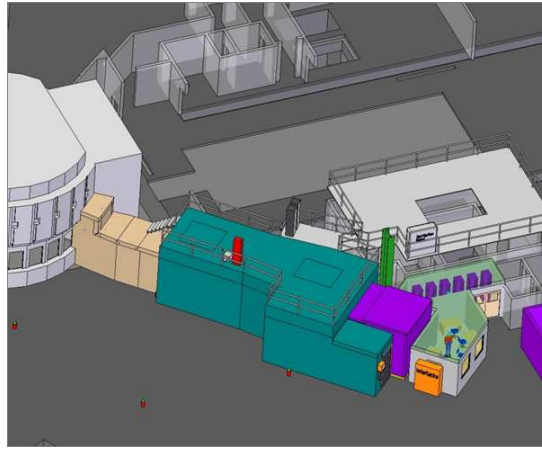


Figure 1.8: CAD model of the CHIPIR beam line [10].

then the present ISIS-TS1 flux and 25 times more than the neutron flux at LANSCE. The user community has proposed two modes of operation: a collimated neutron beam within a containment blockhouse (this is a standard approach adopted by other facilities), and a beam line that additionally provides a large, reasonably isotropic flood of neutrons by the use of additional movable secondary scatterers. The last option will be unique to ChipIr and allow very large systems to be tested.

An important task for ChipIr design is the development of a neutron beam monitor for flux measurements in the MeV energy range. The detector developed in this thesis as a beam monitor for ChipIr is a Single-crystal Diamond Detector (SDD) in which neutron detection occurs by measuring the charge particles produced by neutron interactions with carbon. Chapters 2 and 3 and Papers I - IV present the detector development and the main results of detector tests performed at ISIS.

1.2 FAST NEUTRON MONITOR FOR DEUTERIUM BEAMS

The International Thermonuclear Experimental Reactor (ITER)[14] is a large international project aimed at demonstrating the production of energy from the controlled thermonuclear fusion of deuterium and tritium for a period of

about 30 minutes. The ITER plasma will be heated with a mix of heating systems for a total of 50-70 MW injected into the plasma. About one half of this power will be supplied using Neutral Beam Injectors (NBI) injecting 1 MeV neutral deuterons in the plasma. The underlying technology is still under development. An experimental facility for the NBI prototype tests is under construction at the Consorzio RFX in Padova.

1.2.1 THE PADOVA RESEARCH ON ITER MEGAVOLT ACCELERATOR (PRIMA): SPIDER AND MITICA

PRIMA identifies all the R&D activities that will be realized and hosted at the Consorzio RFX [15]. The facility will host two experimental devices: MITICA, the full injector prototype, and SPIDER, a 100 kV negative D/H RF source. MITICA (Megavolt ITER Injector & Concept Advancement) will be developed in order to be able to emit a beam of neutral particles of deuterium accelerated up to 1 MeV, with a total beam current of 40 A. The beam will be able to transfer a power of 16 MW to the plasma for one hour. SPIDER (Source for Production of Ion of Deuterium Extracted from RF plasma) is an experiment whose goal is to develop the know how on negative ion sources and optimize in terms of production and uniformity the negative ion production. SPIDER will be equipped with a source for negative ions that, once optimized, will be duplicated for MITICA.

1.2.2 A FIRST STEP FOR THE INJECTOR: SPIDER

In Figure 1.9 a CAD model of the SPIDER experiment is shown. The vacuum vessel is composed of four segments, of which two are cylindrical and are of 4 meters diameter, plus two closing caps. The total length of the vacuum vessel is about 5.5 m. In the image the vessel, the source and the stopping system are shown. Deuterium is provided by a plasma produced by means of 8 inductive radiofrequencies generators (1MHz) in a chamber covered with a surface having 1280 holes (the purple panel). The dimension of the holes

will be of about 12 mm, with a pitch distance of 20 mm and 22 mm in the horizontal and vertical directions, respectively. Ions are extracted through the holes and then accelerated up to an energy of 100 keV. In SPIDER two stopping systems will be hosted (shown through the V-panels). The first one, closer to the source, is a diagnostic system able to operate for short periods (up to 10 s), realized in graphite fibers (black panels). The second system (yellow) is copper made, it is water-cooled and its main aim is to neutralize the beam and absorb the thermal load calculated in 7 MW per hour at the maximum performance conditions. This system is called beam dump and a CAD model shown in Figure 1.10 illustrates its main components. It is made of two sets of hypervapotrons stacked vertically (Figure 1.10(a)) supported with a mechanical frame (Figure 1.10(b)). A cross section of the hypervapotron is shown in Figure 1.11, where quotes are in mm. The hypervapotron is made up of a CuCrZn-alloy (with an elemental composition of about 99% Cu) (brown layers) in which cooling water circulates (light blue). The beam dump is placed at a distance of 2.28 to 2.72 meters from the accelerator exit, and the deuterium beam impinges onto it with an incident angle of 30° (Figure 1.12).

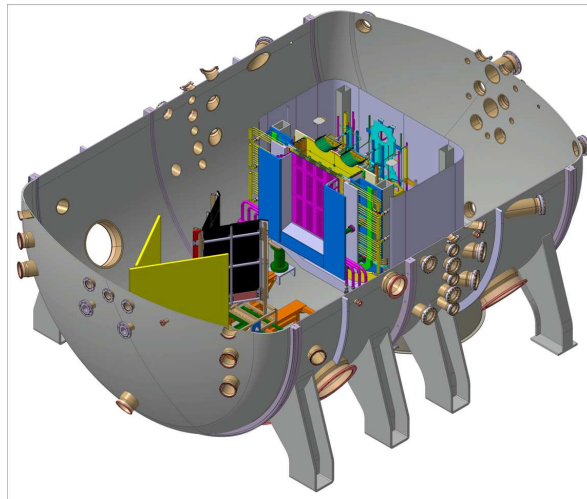


Figure 1.9: SPIDER experimental area: the source and the stopping system are shown. The main stopping system, called beam dump, is shown in yellow.

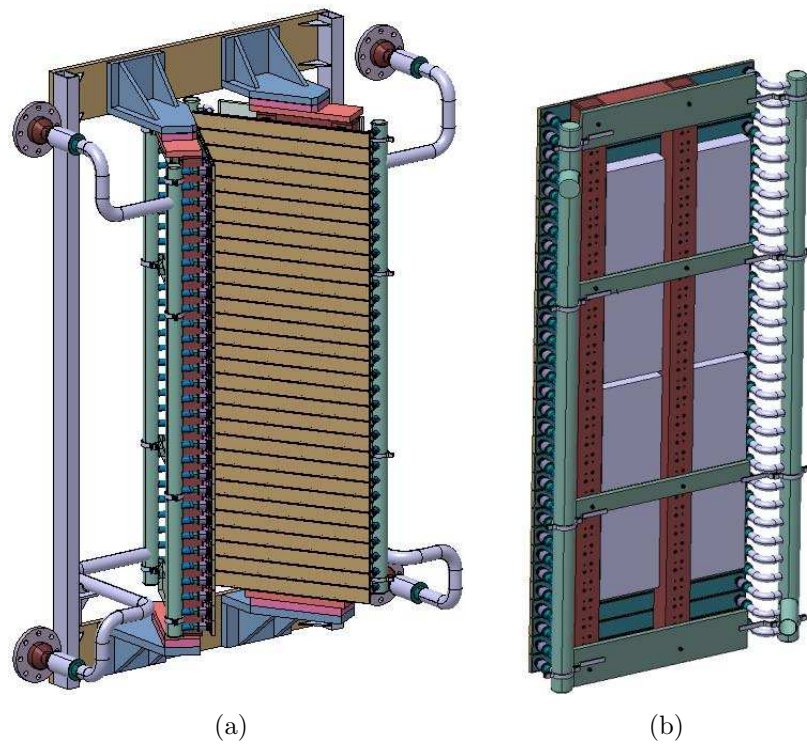


Figure 1.10: CAD model of the SPIDER beam dump: hypervapotrons are arranged in two panels as shown in (a). Each panel is supported on the back by a steel frame with columns (b).

As said before, the deuterium beam is extracted through a grid with 1280 holes. In particular, the holes are arranged in 16 groups, and each group

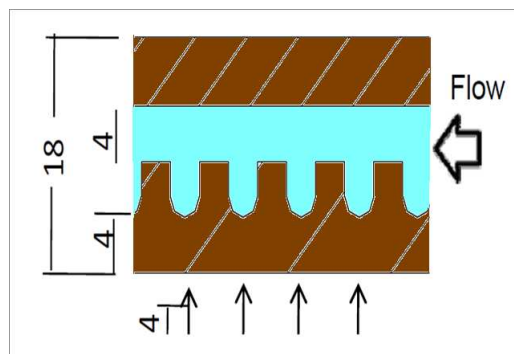


Figure 1.11: Cross section of a hypervapotron in the SPIDER beam dump, quotes are in mm.

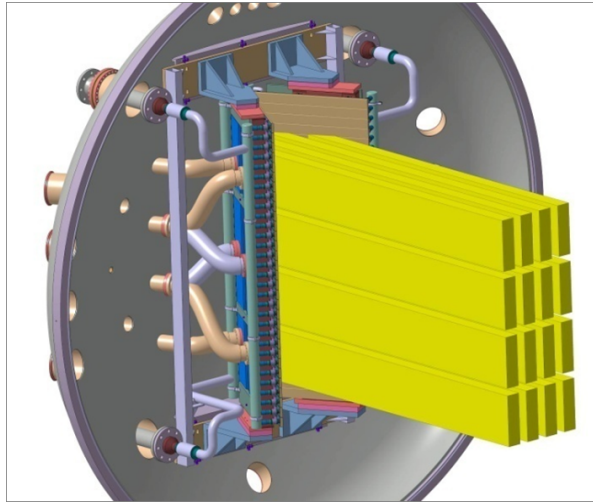


Figure 1.12: The SPIDER beam dump area: the beam impinges on the beam dump surface with an incident angle of 30° .

has 80 holes in a matrix arrangement of 5×16 . The SPIDER beam is thus made of 1280 beamlets impinging on the beam dump surface. The beamlet footprint on the beam dump surface is an ellipse $40 \times 22 \text{ mm}^2$ in the horizontal and vertical direction respectively. The power of each beamlet is maximum at its center and decays from the center according to a Gaussian distribution. The power density (in MW/m^2) contour plot is shown in Figure 1.13. The beamlet centres start at coordinate $(0,0)$ and are spaced by 40 mm and 22 mm in the horizontal and vertical directions, respectively. The power density profile is maximum at the beamlet centres and minimum halfway between them.

In the beam dump a large amount of neutrons will be produced via fusion reaction between the incoming deuterium beam and the deuterium adsorbed in the beam dump ($\text{D}(d,n)^3\text{He}$ reaction). Neutron emissivity and transport in the beam dump will be described in detail in chapter 4: emissivity and transport have been evaluated on the basis of simulations of the different steps, from the implanted deuterium profile density to the neutron scattering in the beam dump materials. The deuteron deposition inside the dump was simulated with the TRansport of Ions in Matter (TRIM)[16] code in

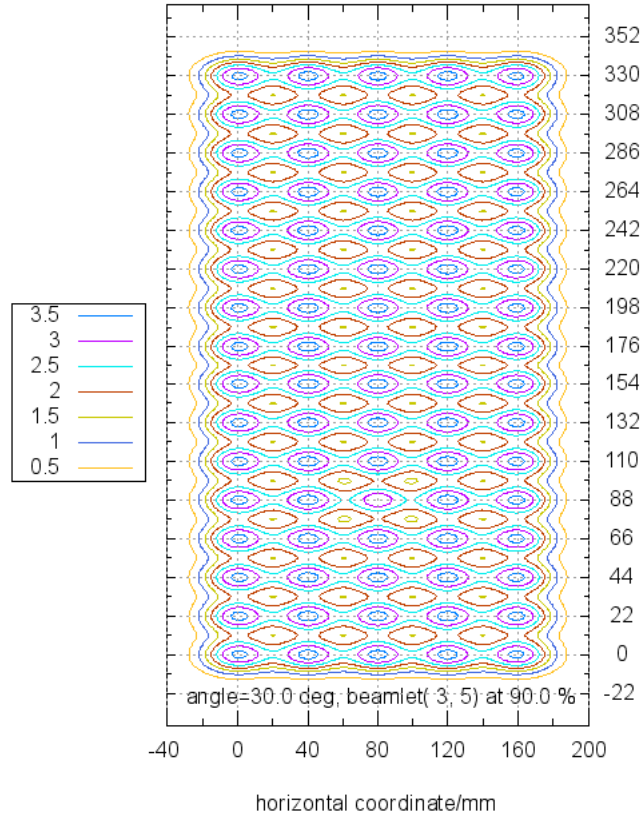


Figure 1.13: Contour plot of the power density profile of a 5X16 beamlet matrix hitting the beam dump. The power density levels are in MW/m².

order to provide the deposition profile. Neutron emissivity as a function of the penetration depth was calculated analytically using the DD reaction cross section. Neutrons are produced up to a penetration depth equal to $\approx 1\mu\text{m}$, and to reach the detector have to cross a thickness of about 17 mm. Scattering effects in the beam dump cannot be ignored, and they were simulated using the Monte Carlo N-Particle eXtended (MCNPX) code [17]. Neutron measurements on SPIDER were studied in order to provide a beam assessment concept that could satisfy the following requirements:

- it should serve a well defined purpose as a diagnostic of SPIDER and provide information with a clear impact on the optimization of the SPIDER beam quality;

- it should be practical in terms of engineering integration in the device;
- it should be affordable, possibly by allowing a modular design where additional resources could be attracted and used as they become available to complete/enhance the detection system during the lifetime of the SPIDER and MITICA experiments;
- the new diagnostic concept should be carried over to MITICA.

The detection system is called CNESM (Close-contact Neutron Emission Surface Mapping) and it will be placed right behind the beam dump, as close as possible to the neutron emission surface, as indicated in Figure 1.12. Figure 1.14 represents the top view of the beam dump area with the beam dump (brown), the incoming beam (yellow) and the detector box (green box). In

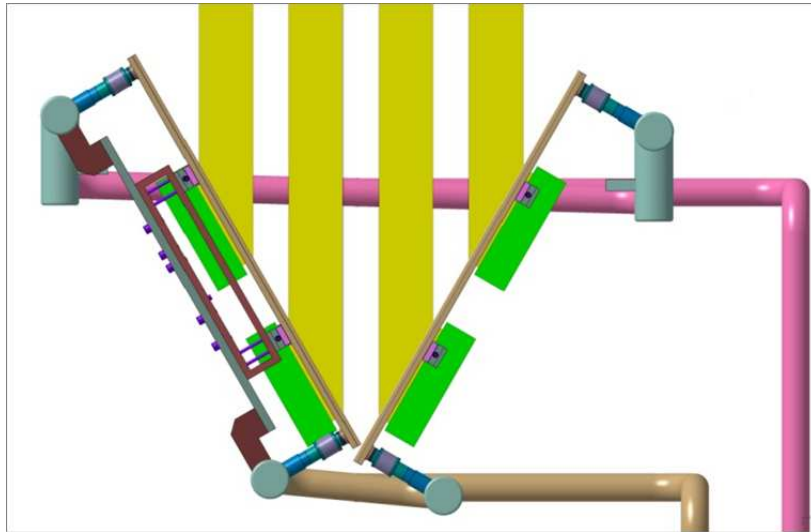


Figure 1.14: Top view of the SPIDER beam dump area: the detector boxes are shown in green.

chapter 5 a description of the CNESM diagnostic system is provided. The CNESM diagnostic system is mainly based on a *neutron GEM* (nGEM) detector able to provide the map of neutron emission from the beam dump with a spatial resolution approaching the size of an individual beamlet footprint. This is obtained by ensuring that most of the detected neutrons at a point of

the nGEM surface are emitted from the corresponding $40 \times 22 \text{ mm}^2$ beamlet footprint on the dump front surface. The nGEM detector can provide very useful information of the beam intensity map which is the goal of CNESM on SPIDER and a first step towards the installation of CNESM on MITICA where it will provide unique information on the horizontal beam profile.

Chapter 2

Diamond detector prototypes test

Diamond is widely used in many applications due to their unique properties. Due to the high refraction index (2.42 compared to 1.5 for glass), diamond is used as gems. It is one of the hardest materials in nature and thus found many application in industry (e.g. drilling). A more recent application is its use as radiation detector material due to its radiation hardness, allowing for long life operation in harsh environments, and high band gap, allowing for good energy resolution at room temperature.

2.1 DIAMOND DETECTORS

Diamond is an insulating material with a very large band gap, 5.5 eV. It can be operated as the other semiconductors of the IV group, such as Si and Ge, by applying electrical contacts to opposite faces of the crystal. Diamond detectors can be used in extreme conditions where other detectors cannot: they can be operated at high temperatures (250-300 °C) and in environment where the radiation level is very high (for example the CMS experiment at LHC [18]). Due to their high band gap, they are characterized by low Johnson noise and by very low dark current. A charge particle or a photon with energy above the band gap, crossing the diamond, produces electron/hole pairs ($E_{e-h}=13$ eV) which are separated by the electric field between the electrodes and then collected. Diamond detectors are characterized by a fast

response time of several nanoseconds (comparable to Si and Ge). Measurements reported in [19] show a good energy resolution: 0.4% at the 5.5 MeV alpha peak of ^{241}Am . In Table 2.1 the most important diamond characteristics are reported.

	Si	Ge	CVD-Diamond
Atomic Number Z	14	32	6
Density [g/cm ³]	2.33	5.33	5.47
Band Gap [eV]	1.1	0.6	5.5
Electron Mobility [cm ² /V · s]	1350	3900	1800
Hole Mobility [cm ² /V · s]	480	1900	1200
Breakdown field [MV/cm]	0.3	0.1	10

Table 2.1: Diamond characteristics compared to those of Si and Ge [20].

By microwave Chemical Vapour Deposition (CVD) diamonds can be produced with an active thickness ranging from few microns up to 500 μm [21][22][23].

2.1.1 NEUTRON DETECTION USING DIAMONDS

Neutron detection using diamonds is based on the collection of the electrons/holes pairs produced by charged particles generated by neutron reactions with carbon. The most important reactions producing charge particles are:

- the elastic channel, in which a neutron hits a carbon atom. The carbon atom recoils with an energy equal to $E_R^{\text{max}} = \frac{4A}{(1+A)^2}(\cos^2\theta)E_n$, where θ is the recoiling angle and $A=12$.
- the $^{12}\text{C}(n, \alpha)^9\text{Be}$ reaction, in which a neutron breaks the carbon nucleus into an alpha particle and a ^9Be atom. The energy threshold of this reaction is 6.17 MeV, the Q-value being negative and equal to -5.7 MeV.

- the $^{12}\text{C}(n,n')3\alpha$ reaction, in which the carbon nuclei break up into three alpha particles. The energy threshold of this reaction is 7.9 MeV, the Q-value is -7.3 MeV.

The cross sections of these reactions are reported in Figure 2.1 [24]. The

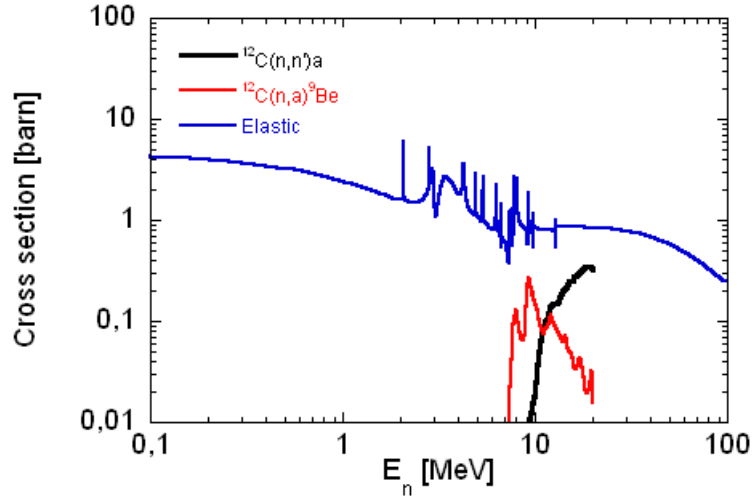


Figure 2.1: Cross sections of the most important neutron induced reactions with carbon [24].

elastic cross section is the most important in the neutron energy range 1-6 MeV, where the reaction $^{12}\text{C}(n, \alpha)^9\text{Be}$ (n-alpha reaction) and $^{12}\text{C}(n,n')3\alpha$ (n-3alpha reaction) cannot take place. These channels are the most efficient in the neutron energy range above 10 MeV because the energy released in diamond is greater respect to the energy released by carbon elastic recoil. The n-alpha and the n-3alpha reactions cross sections are well known only up to 20 MeV [24].

2.1.2 DIAMOND DETECTORS DEVELOPED: SDD AND FDD

Diamond detector prototypes tested in 2009 and 2010 were produced at the University of Roma Tor Vergata by the CVD technique (see Figure 2.2) [21][22][23]. The detector is realized using a High Pressure High Temperature (HPHT) single crystal diamond as substrate. Two CVD-diamond layers

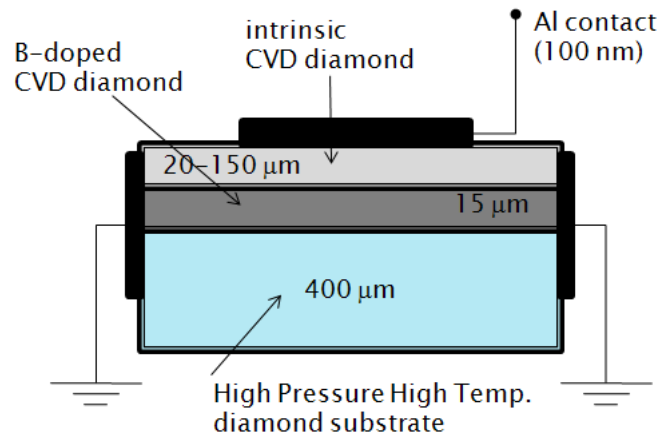


Figure 2.2: Scheme of the configuration of a diamond detector realized at the University of Roma Tor Vergata. From bottom to top: High Pressure High Temperature substrate, B-doped CVD diamond, intrinsic CVD diamond, Al contact.

are deposited onto the HPHT diamond: the first one is a Boron-doped layer (15 μm), the second is the intrinsic diamond layer with a thickness up to 150 μm . The last layer is the Al contact used to polarize the detector. The active detector area is few mm^2 .

In figure 2.3 a photo of the device is reported. The first prototypes are based

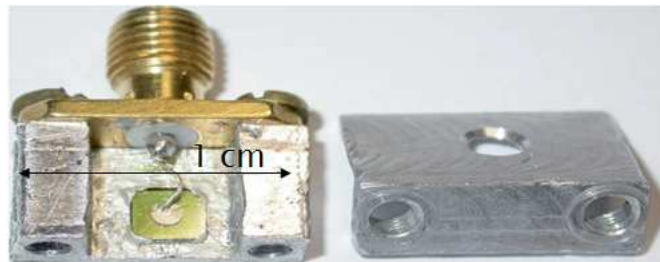


Figure 2.3: Photo of diamond detector produced at the University of Roma Tor Vergata.

on a SDD in which the intrinsic layer are: 70 μm for the first detector (SDD-70), 150 μm for the second one (SDD-150), and 24 μm (SDD-24) for the last one.

These detectors were tested by placing them directly in the neutron beam.

Diamonds SDD-70 and SDD-150 have been coupled to an electronic chain able to measure the neutron Time of Flight only; diamond SDD-24 was coupled to an electronic chain providing biparametrical information (Time of Flight and Energy). In the next section an introduction on the performed measurements will be provided; the results obtained with SDD-70 and SDD-150 are reported in detail in papers I and II. In the third section of this chapter the description of biparametrical measurements performed using the SDD-24 will be given.

Another detector was developed using a single crystal diamond detector facing a uranium foil. The uranium foil was a sheet of $2 \text{ mm}^2 \times 25 \text{ }\mu\text{m}$ of natural uranium placed inside the detector top, shown in Figure 2.3. Natural uranium is made of 99.3 % of ^{238}U and 0.7 % of ^{235}U . The presence of the uranium foil allows for the detection both of neutrons interacting with carbon nuclei and of fission fragments originated by neutron interaction in uranium. In the third section of this chapter a detailed description of such a detector, called Fission Diamond Detector (FDD), is provided. In paper III the most important results obtained with the FDD are summarized.

2.1.3 TIME OF FLIGHT TECHNIQUE

ISIS is a pulsed source. In pulsed facilities the Time of Flight (ToF) technique is a powerful method to determine the neutron energy. Once the flight path (the distance between the neutron source and the detector) is fixed there is a unique connection between neutron energy and the neutron travel time. This can be written as:

$$E_n[\text{eV}] = \left(\frac{72.2985 \cdot L_0[\text{m}]}{t_{\text{ToF}}[\text{ }\mu\text{s}]} \right)^2 \quad (2.1)$$

where L_0 is the neutron flight path and t_{ToF} its Time of Flight. t_{ToF} in a pulsed neutron source can be easily calculated because the neutron generation time, T_0 , is well-known. At ISIS the T_0 is determined by a digital NIM signal which represents the time in which the protons are extracted from the synchrotron and reach the target. t_{ToF} is calculated by making the difference

between the T0 and neutron arrival time (T_{stop}).

Unfortunately the electronic chain of the T0 is very slow. This means that the T0 signal arrives at the SDD electronic chain with a 5 μ s delay respect to fast neutrons. This delay is not a problem for measurements in the thermal and epithermal neutron energy range where flight times are typically 1 ms. However for fast (MeV) neutrons this delay is problematic because the T_{stop} signal occurs before the T0 (T_{start}). Suitable solutions were adopted in this thesis in order to correlate the neutron signal to the relative delayed T0.

2.2 TIME OF FLIGHT MEASUREMENTS WITH A SDD

The very first results using a SDD are reported in paper I: the experiment was performed at the VESUVIO beamline using SDD-70. These results showed the capability of diamond detectors to measure fast neutrons from a pulsed neutron source. The detector was placed directly into the neutron beam, and the time of flight was measured using a fast digital scope and a fast preamplifier. The same electronic chain was used in measurements, described in this section, performed on the ROTAX beamline in December 2009 with the SDD-150 detector.

2.2.1 THE EXPERIMENTAL SET-UP

ROTAX is a test beamline whose moderator is a 95 K methane moderator, the flight path is about 14 meters and the neutron flux is about 10^6 n/cm² · s. A photo of the ROTAX experimental hall is shown in Figure 2.4. The experiment was performed using a SDD coupled to an electronic chain able to preserve the fast response of the diamond detector. A $V_{bias} = 100$ V was applied to SDD-150. The signal from the detector was amplified using a fast preamplifier with an integration time of few ns. The used preamplifier was a DBA III inverting preamplifier with a total gain of 38 dB. More details on such preamplifier can be found in [25]. The signal from the preamplifier was detected using a digital scope (2.3GHz bandwidth and 50GHz sampling rate). A typical signal from the DBA III preamplifier, acquired during the



Figure 2.4: Photo of the experimental set-up (neutrons are coming from the right).

detector calibration with α particles from a ^{241}Am source, is shown in Figure 2.5. The signal pulse width (FWHM) is ≈ 2.5 ns. More relevant is the pulse rise time, which is about 1 ns; the signal decay time is about 10 ns with an amplitude of about 320 mV.

The Time of Flight was calculated by the digital scope by making the dif-

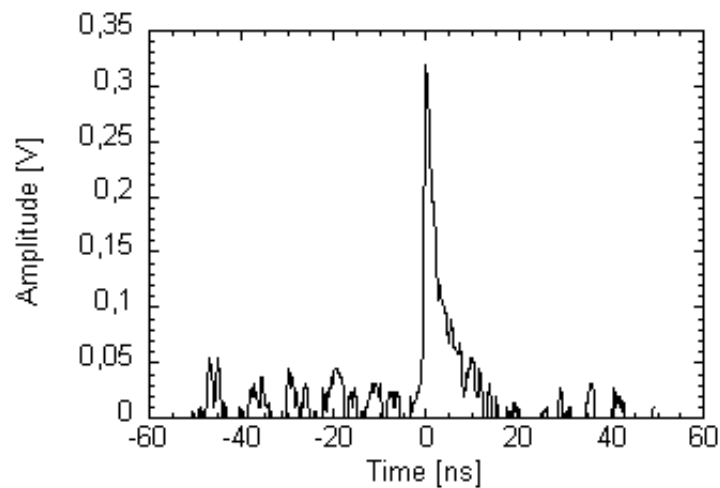


Figure 2.5: Signal pulse recorded by the SDD irradiated with α particles from a ^{241}Am source. The SDD was connected to a DBA III preamplifier and a fast digital scope.

ference between the diamond signal and the T0. Triggering was performed

both on the diamond signal and the T0, the acquisition window was $5.5 \mu\text{s}$ wide in order to allow for the calculation of the difference between the T0 and the diamond signal triggers. The t_{ToF} spectrum was calculated directly by the scope, allowing a direct comparison between the acquired data.

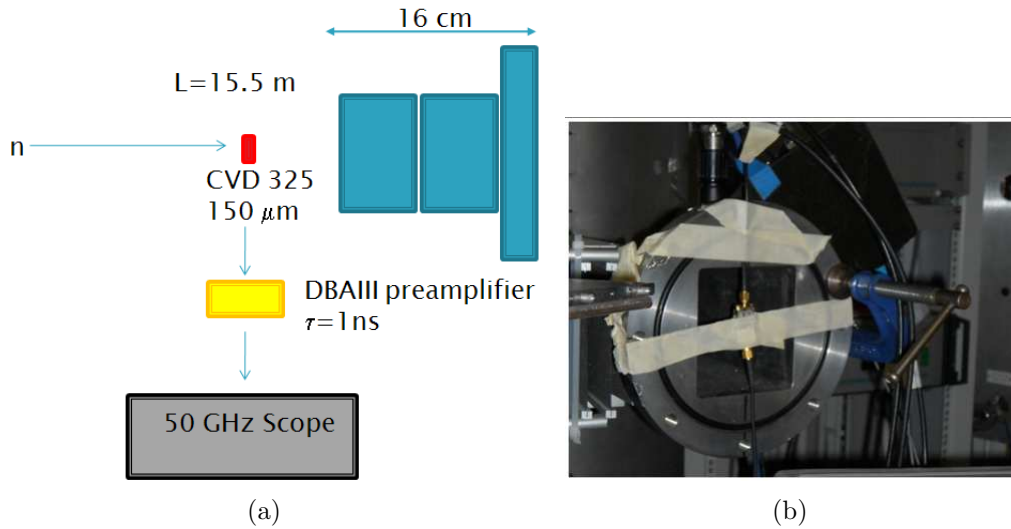


Figure 2.6: Experimental set-up before (a) and after (b) the moderator in the SDD test at the ROTAX beam line.

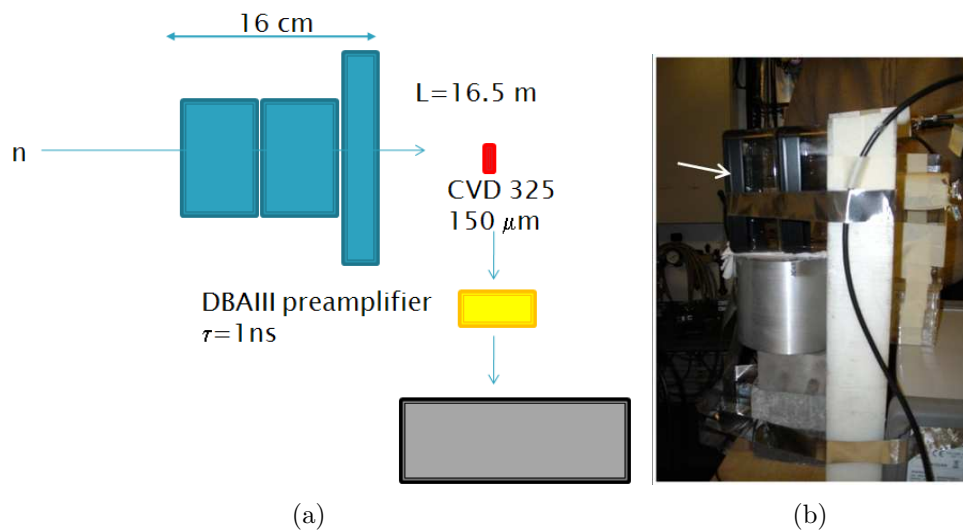


Figure 2.7: Experimental set-up after the moderator in the SDD test at the ROTAX beam line.

Two measurements were performed: the first one (Figure 2.6) by placing the SDD into the ROTAX neutron beam and measuring the t_{ToF} at a distance of 15.5 meters from the moderator; the second one (Figure 2.7) by placing the SDD behind a polyethylene-water extra moderator installed in the beam line, the flight path in this case being 16.5 meters. The extra-moderator was made of a polyethylene slab with a total thickness of 6 cm, and a box with 12 cm of water. The thickness was chosen to significantly attenuate the neutron spectrum below 10 MeV. In both measurements a threshold of 3 MeV was set, and the t_{ToF} spectrum was acquired for 10 hours in the first configuration and for 20 hours in the second one. The integrated proton current during the measurements was 1761 μAh and 3598 μAh , respectively.

The main result of the measurement is that the t_{ToF} spectrum, Figure 2.8,

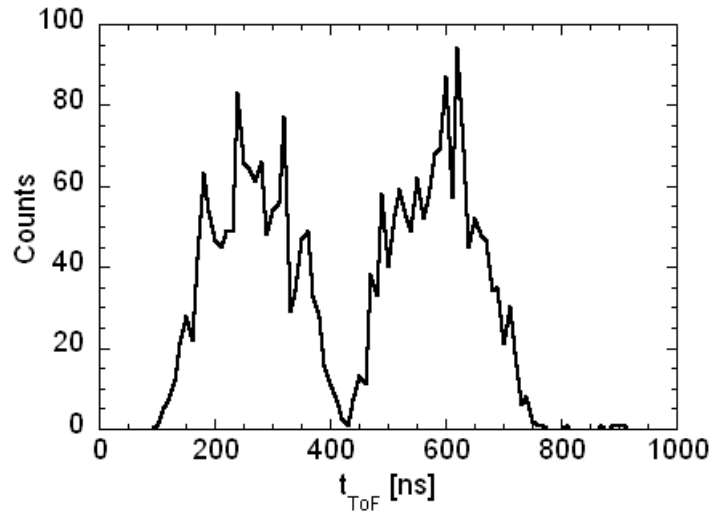


Figure 2.8: Time of flight spectrum obtained before the moderator.

presents a double hump shape, due to the ISIS proton beam time structure, shown in figure 1.5. The two bunches are separated by 322 ns but the bunch width is no longer 70 ns, but about 200 ns, due to the fact that neutrons with different energies have different flight times. The two bunches are well separated, which is due to the detector threshold used (see chapter 3) making the detector practically insensitive to neutrons with $E_n < 6$ MeV (i.e. t_{ToF}

values above ≈ 450 ns). The total number of recorded events is 2690 which corresponds to a count rate of about 0.077 c/s.

From the t_{ToF} measurement performed behind the moderator the double bunch structure is still visible and the spectrum is almost unaffected up to 250 ns (neutron energy ≈ 20 MeV) as clearly visible in Paper III. Such results have been interpreted via MCNPX simulations. MCNPX was used to generate a neutron energy spectrum at the two detection positions. The neutron spectrum before the moderator is the same reported in figure 1.7: the spectrum after the moderator was simulated implementing into the MCNPX code the geometry of the moderator, and measuring the neutron flux with an F2 MCNPX tally. It appears that the less energetic neutrons are the most attenuated by the water-polyethylene moderator. The most energetic part of the spectrum, above ≈ 20 MeV, remains almost the same in both cases. Further details and results are reported in Paper III.

2.3 BIPARAMETRIC MEASUREMENTS WITH SDD AND FDD

During the same experimental campaign measurements were also performed to compare SDD and FDD. A SDD and a FDD both of thickness $24 \mu\text{m}$ ($V_{\text{bias}} = 30$ V) were used with an electronic chain providing a biparametrical information on the recorded events: the t_{ToF} and the energy deposited in the detector by each event (E_d). Goal of experiment was to understand whether correlation between t_{ToF} and E_d is possible, and the separation between the contribution due to the natural uranium events and carbon events in FDD is achievable.

2.3.1 THE ELECTRONIC CHAIN

The electronic chain was developed during laboratory tests performed before the ISIS campaign. Its main characteristics are:

- The diamond detector: SDD-24 was used at ISIS, in laboratory the SDD-100 was also used.
- The preamplifiers were custom preamplifiers realized at the Politecnico di Milano. The first one has a rise time of 40 ns and the shaping time is about 500 ns; the second one has the same rise time but the shaping time is about 5 μ s. The preamplifiers provide both the detector output and the detector bias.
- the Timing Filter Amplifier (TFA) is used to amplify and to shape the signal before sending it to the acquisition module. The TFA parameters are:
 - gain=2,
 - fine gain=2,
 - differentiation constant=0 ns,
 - integration constant=10 ns,
 - non inverting.
- The acquisition module adopted is a CAEN N1728B digitizer module [26]: this is a four-channel, 100 MHz ADC. It can be used in *Energy* mode, providing a list of biparametrical data: for instance time and amplitude of the signals. However, the time is calculated from the start time of the measurements. Thus, in order to obtain a Time of Flight spectrum the data from the N1728B module need further processing as explained later. The sampling period is 10 ns: the time resolution achieved during the tests is 10 ns. The energy calculation is made by a trapezoidal shaping, with a wide range of programmable parameters. The algorithm used for energy calculation is the Jordanov-Knoll one [27].

The first tests were done using the detectors SDD-24 and SDD-100. The detectors and the electronic chain resolutions were measured using an ^{241}Am α source and a pulse train generator in order to simulate the detector signal. The calibration measurements were performed in vacuum for 6 different

values of bias supply, V_{bias} . In Figure 2.9 the energy spectrum obtained is shown for $V_{bias} = 30$ V, 40 V, 50 V, 70 V and 80 V. For V_{bias} two peaks are

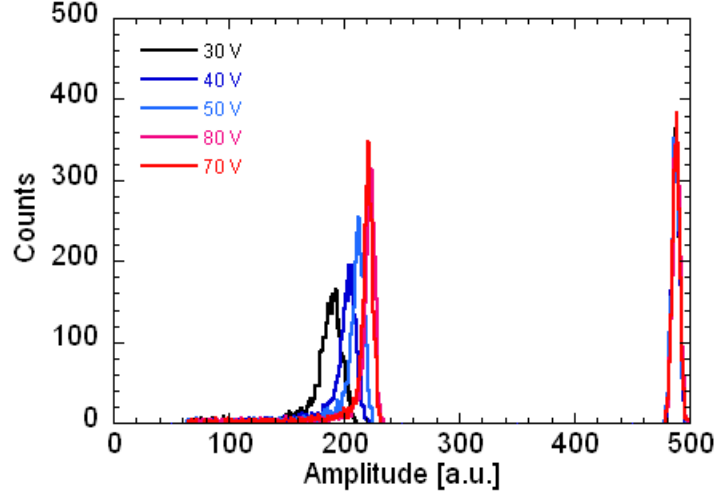


Figure 2.9: Energy spectrum obtained using the SDD-24 coupled to the biparametric electronic chain. The energy spectrum is reported for five different values of V_{bias} . The first peak is the peak from alpha particles of ^{241}Am , the second is the peak from the pulse shape generator.

visible: the first one is the peak from ^{241}Am , the second one, at about 500 a.u. is the pulse generator peak. The latter, as expected, does not vary with V_{bias} . On the other hand, by increasing V_{bias} , the α peak becomes higher and moves to the right: this is because, by increasing the bias supply, the electric field is higher, which makes the collection of electrons and holes more efficient. At 70 V the collection efficiency is maximal, in fact at 80 V the peak is the same as 70 V. Moreover the detector energy resolution increases by increasing the V_{bias} , as shown by the FWHM/peak position ratio (Figure 2.10). The resolution for the α peak increases up to 70 V, where it is equal to 4%, while it is constantly 1.5% for the pulse generator peak.

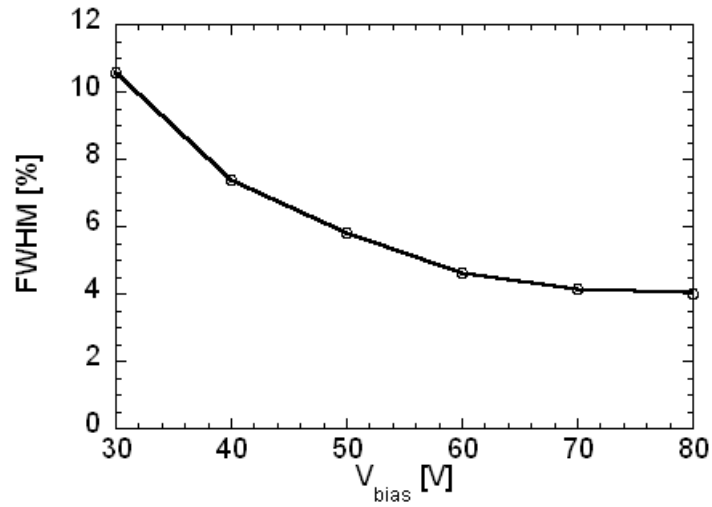


Figure 2.10: Energy resolution achieved for the SDD-24 as a function of the detector bias supply, V_{bias} .

2.3.2 THE EXPERIMENTAL SET-UP AT ISIS

The experimental set-up used in the tests performed at ISIS is reported in Figure 2.11. The signal from the detector was preamplified using the

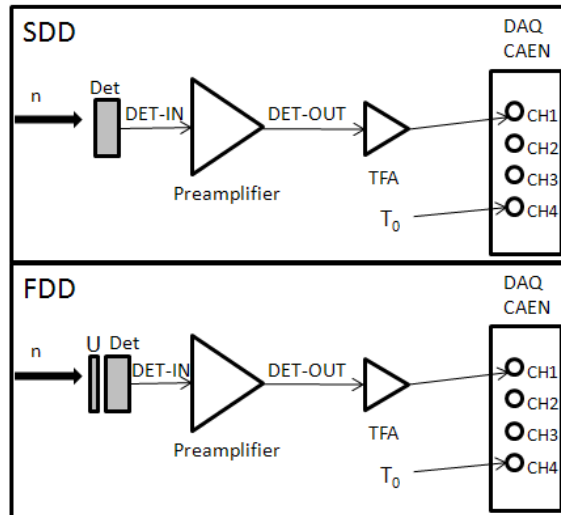


Figure 2.11: Schematics of the electronic chain used in the measurements performed at ROTAX using the FDD and the SDD.

500 ns shaping time; a Timing Filter Amplifier (TFA) was used in order to increase the signals amplitude by a factor 4. The acquisition module was the N1728B. For each event pulse height and time of arrival are stored in a single file. Neutron Time of Flight was calculated off line with reference to the T0 which is also stored by the acquisition module. The acquisition trigger is made both on the T0 and on the diamond signal, meaning that every event occurring at any time is stored, i.e. in these measurements no acquisition window is present. Data were collected for 22 hours using the SDD, corresponding to an integrated proton current of 3942 μAh , and for 20 hours using the FDD, i.e. 3578 μAh .

2.3.3 BIPARAMETRIC MEASUREMENT WITH THE SDD

In Figure 2.12 the scatter plot of the biparametric data of SDD is shown. On

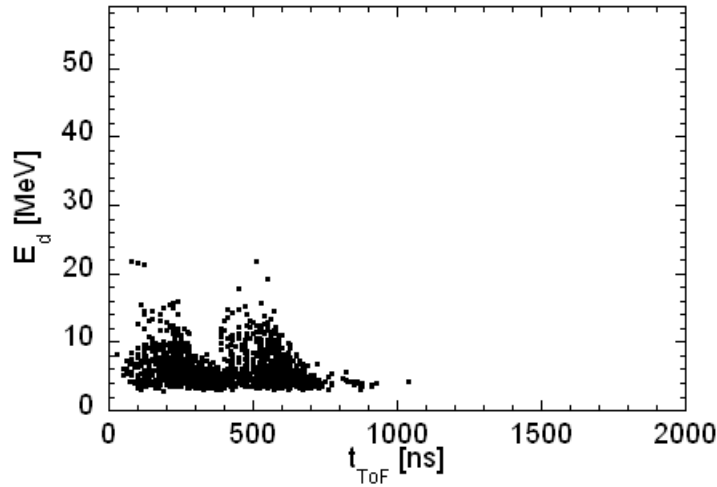
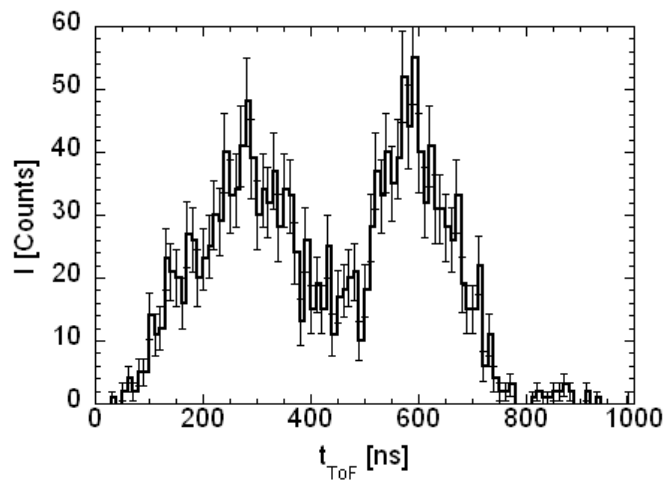


Figure 2.12: Scatter plot of the events recorded by the FDD.

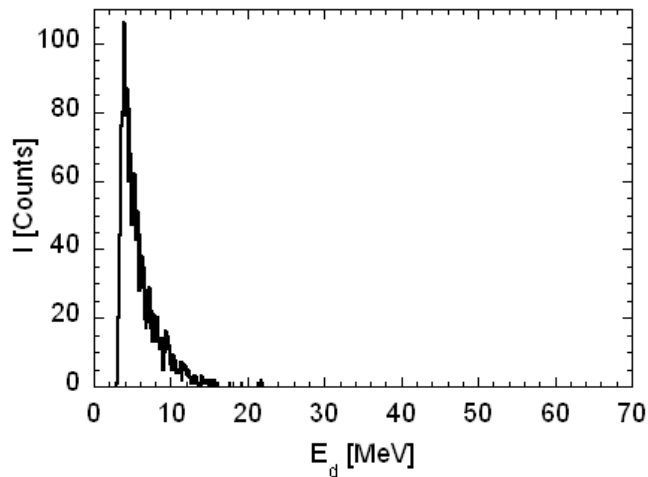
the x axis t_{ToF} is in ns, on the y axis the energy deposited in the detector, E_d , is in MeV. All the events occur in the first 1 μs , and deposit less than 20 MeV in the detector. The total number of recorded events is 1778 which corresponds to a count rate of 0.021 c/s. The events are divided into two regions: the first from 0 to 450 ns, the second from 450 ns up to about 900.

This represent the double pulse structure of the proton temporal profile, already discussed in the previous section. The most energetic events are visible only on the left part of the bunch. This means that the most energetic neutrons deposit more energy in the detector than neutrons events occurring at longer t_{ToF} : a correlation between the energy deposited in the detector and the neutron t_{ToF} is present. Unfortunately the low count rate precludes a more quantitative analysis of the data.

In Figure 2.13 the scatter plot projections on the x-y axes are shown. The



(a)



(b)

Figure 2.13: Time of flight (a) and E_d (b) spectrum of the SDD.

projections confirm that the maximum energy deposited in the detector is about 20 MeV, and the t_{ToF} spectrum shows clearly the double structure of the proton time distribution. However the overall quality of the data is rather poor: we reckon this is mainly due to the count rate and the slow electronic chain. The data quality was much improved in this thesis by adopting a bigger detector and improved electronic chain as described in chapter 3.

2.3.4 BIPARAMETRIC MEASUREMENT WITH THE FDD

Another experiment performed in these measurements was the test of a FDD. As explained before this detector combines the diamond response (via the reactions $^{12}\text{C}(n, \alpha)^9\text{Be}$ and $^{12}\text{C}(n, n')3\alpha$) with the response due to the presence of a natural uranium foil. In Figure 2.14 the scatter plot of all the recorded

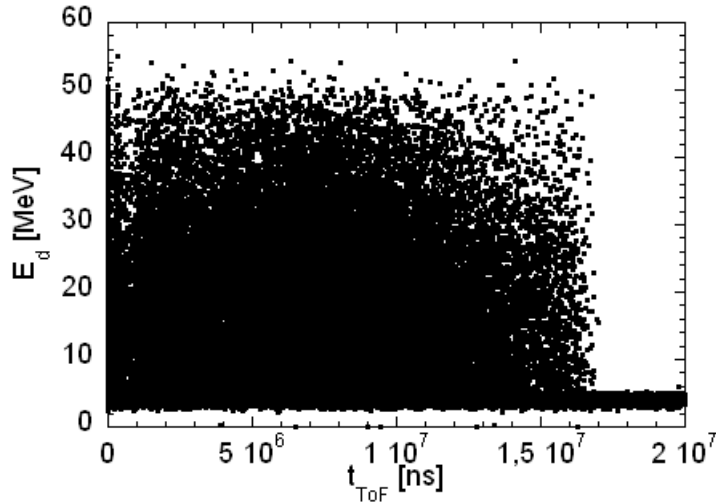


Figure 2.14: Scatter plot of all the events recorded by the FDD.

events is shown. Since ISIS is a pulsed source with a frequency of 50 Hz, the temporal distance between the pulses is 20 ms: this is the maximum time distance between the events recorded by the diamond and the T0. In the scatter plot of Figure 2.14 we see many events that are not present in the scatter plot in Figure 2.12: these events are due to the presence of the uranium foil. On the plot we can see a background of events at every time

with an amplitude between 2.8 MeV (the acquisition threshold) and 4 MeV: these events are due to the alpha particles emitted by the uranium foil and reaching the detector. We also see energetic events up to 50 MeV, with a t_{ToF} up to 17 ms: these events are due to neutron interaction in the uranium foil. Since the uranium foil was made from natural uranium we have that thermal neutrons also can produce a signal on the FDD. In fact thermal neutrons interact with ^{235}U producing fission fragments which reach the detector. The natural abundance of ^{235}U in natural uranium is only 0.7%. Although the natural abundance is very low, thermal neutron flux is higher respect to fast neutrons, and fission cross section of ^{235}U is 100 times higher than ^{238}U . Therefore this detector can in principle be used to measure the neutron spectrum from thermal component up to 800 MeV. We can discriminate the fission events originated by fast neutrons, considering the the fission energy threshold of ^{238}U is about 0.8 MeV. This means that only neutrons with a t_{ToF} shorter than 1.3 μs can produce fission fragments by interacting with ^{238}U . In Figure 2.15 the scatter plot of events in the first 2 microseconds is reported. In this figure we can see the contribution due to both carbon

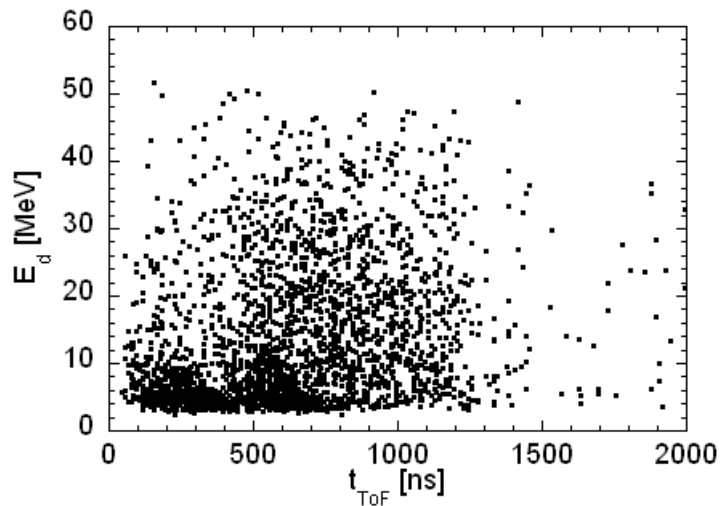
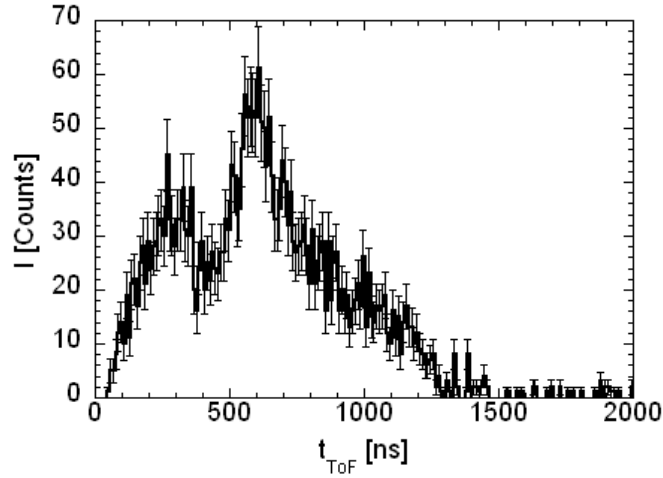


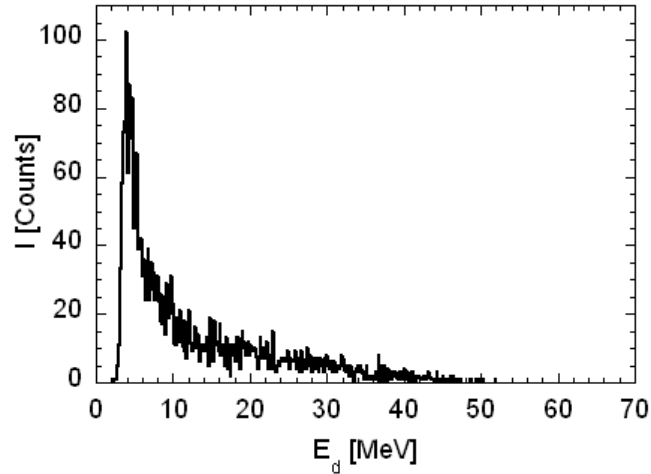
Figure 2.15: Scatter plot of the events recorded in the first two microseconds by the FDD.

and natural uranium. The total number of recorded events in this region is

3302 which corresponds to a count rate of 0.046 c/s. This is about twice the one obtained in the measurement with the SDD-24: the contribution of the uranium increases the count rate by a factor two. Observing the t_{ToF} spectrum and the E_d spectrum (Figure 2.16), we can see that the highest energy deposited is 50 MeV, much higher than in the case of the SDD-24 (20 MeV). This means that fission fragments deposit more energy in the detector



(a)



(b)

Figure 2.16: Time of Flight (a) and E_d (b) spectrum of the FDD.

than events due to carbon reactions. Moreover, observing the t_{ToF} spectrum

we see that using FDD we are able to see events with an energy lower than 6 MeV, i. e. a t_{ToF} higher than 800 ns. This comparison can be performed also comparing graphs 2.15 and 2.12: events above 20 MeV are due only to fission fragments. Thus, the t_{ToF} spectrum for fission fragments events only is shown in Figure 2.17. In this plot we do not see anymore the double pulse structure of proton bunches because the fission energy threshold is 1 MeV, which corresponds to a t_{ToF} of about 1 μs . Considering the fact that the temporal distance between the two proton bunches is 322 ns, it is no longer possible to separate the contribution of the two bunches, therefore we see a single structure 1.2 μs wide. This is compatible with the Time of Flight spectrum measured with Thin Film Breakdown Counter on the VESUVIO beamline [28].

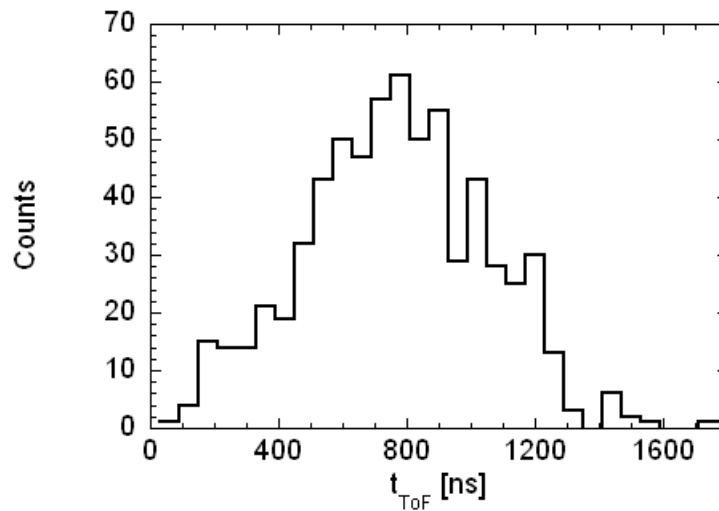


Figure 2.17: Time of Flight spectrum obtained considering only events which deposit more than 20 MeV in the FDD. These events are due to fission fragments originated by neutron-induced fission on ^{238}U .

2.4 CONCLUSIONS FROM DIAMOND DETECTOR PROTOTYPE TESTS

The tests performed with diamond detector prototypes as described in this chapter and in Papers I- III provide the evidence for the subsequent detector development. The recorded t_{ToF} spectrum shape depends on the choice of pulse height threshold and was explained on the basis of the known interactions of neutrons in the diamond. Biparametric (pulse height and t_{ToF}) data provided evidence of correlation between the energy deposited and the t_{ToF} , although the low count rate obtained was not enough for a quantitative analysis. Moreover, the count rate obtained using SDD-24 and SDD-150 is not proportional to the diamond thickness, probably due to the active diamond detector thickness being lower than the thickness of the diamond crystal.

In order to better demonstrate the diamond detector capability as a fast neutron beam monitor, new tests were performed using larger diamond detectors coupled to a fast waveform digitizer. The experiments were performed at ISIS during year 2011 and are the topic of the next chapter.

Last but not least, by adding a natural uranium foil to the diamond detector we are able to increase by a factor two the count rate in the t_{ToF} region of interest. Using the FDD it is possible to measure neutrons from 2 MeV. The FDD tested at ISIS may find application as a flux monitor for 2.5 MeV neutrons in the SPIDER diagnostic system, as we are going to see in chapter 5.

Chapter 3

Results from diamond detector measurements at high rates

A first step towards the use of SDDs at ISIS is to demonstrate reliable operation of the SDD detector in biparametric mode of operation in a high neutron flux. Tests of diamond detectors, previously performed at ISIS, were reported in the previous chapter, in papers I, II, III and in [29][30][31][32]. These tests were performed at rather low neutron detection rates using custom made fine quality diamonds of small active volume. In the tests presented in this chapter and in paper IV, two larger SDDs were coupled to a fast waveform digitizer suitable for off-line biparametric analysis.

3.1 THE NEW DETECTOR SET-UP

Diamond detectors used for measurements were Single Crystal Diamonds produced by Diamond Detectors Ltd. (DDL) [33]. Most of the measurements were performed with two SDD detectors placed in the neutron beam of the VESUVIO [34] beam line at a flight distance of about $L=12.5$ m from the neutron source; for comparison data were also collected at the ROTAX beam line at about $L=14.2$ m flight distance. Two diamond detectors from different production batches and featuring aluminum (Al-SDD) or gold (Au-SDD) as contact materials were placed in the neutron beam for about three days.

The nominal active volume of the two detectors is identical being 4.7×4.7 mm² area and 0.5 mm thickness. The electrical contacts have 4.5 mm diameter. The contact is DDL proprietary and it is made, top and bottom, of Diamond Like Carbon(DLC)/Pt/Au or Al layers, as indicated in Figure 3.1. A DLC is grown in order to obtain a better coherence of the Pt/Au or Pt/Al depositions. This allows minimal polarization effects while maximizing stability and contact resilience [35]. Both detectors were mounted on a movable

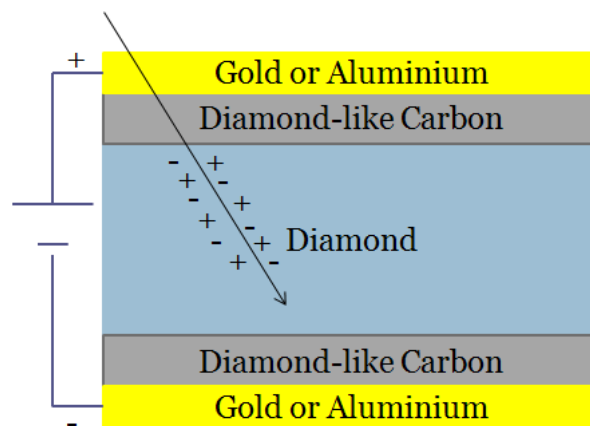


Figure 3.1: Picture of the DDL proprietary contact.

support that was used to move the SDDs remotely in the horizontal direction during some of the measurements (Figure 3.2). Two commercial fast preamplifiers, DBA III and DBA IV [25] were used to preserve the fast response of the SDDs. Both preamplifiers have a shaping time of about 10 ns and a broad bandwidth in the range 3 MHz - 3 GHz. The gain can be remotely controlled but was fixed in these experiments to the maximum available gain; i.e. 38dB and 46dB for the DBAIII and the DBA IV, respectively. An additional custom wideband amplifier (gain=4) was used in order to boost the amplitude of the signal from the DBAIII preamplifier. The signals from the two detectors were fed into the CAEN waveform digitizer model DT5751 [36]. This is a four channel desktop digitizer with a sampling frequency of 1 GHz, input range 0-1 V and 10 bit resolution. The waveforms from both SDDs were stored in coincidence with a reference signal generated by the proton extraction from the synchrotron. For each ISIS pulse a waveform of 2500

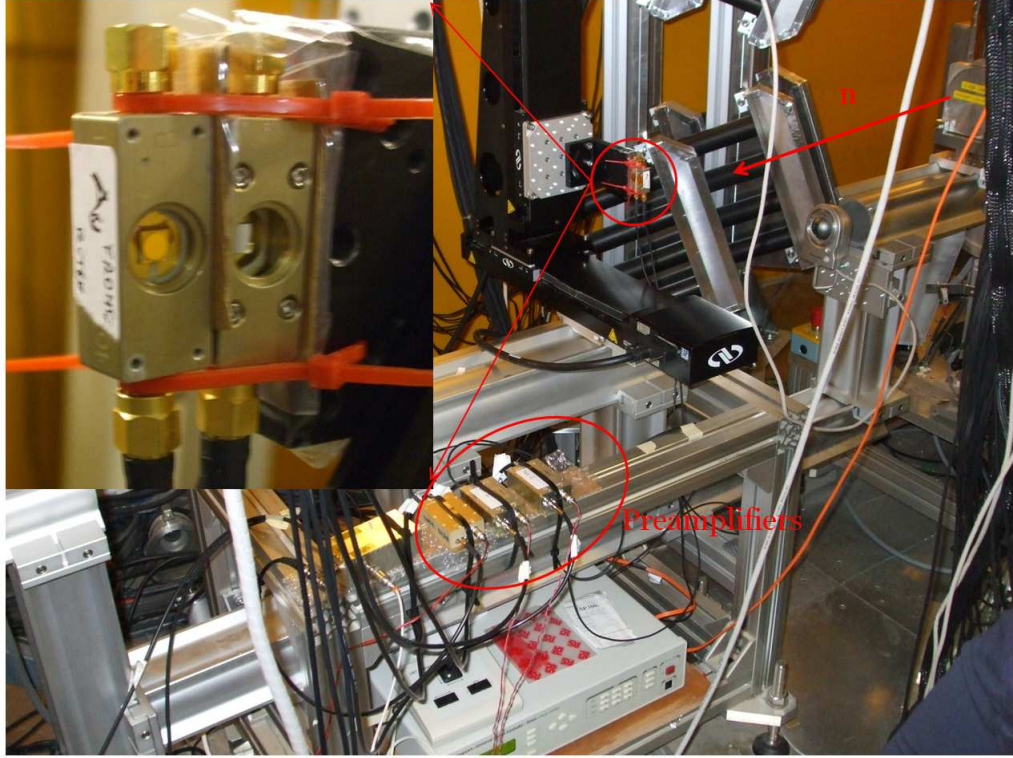


Figure 3.2: A picture of the experimental set-up at the VESUVIO data campaign in October 2011. Neutrons are coming from the right, the detectors are placed directly into the neutron beam. Both detectors were mounted on a movable support used for beam profile measurements. A zoom of the detectors is visible on the left part of the Figure.

ns is stored; all time values are synchronised during the analysis relative to the arrival time of the photons at the detector. The latter is set so that the peak in time of the photon signal occurs at L/c where c is the speed of light; $L/c=42$ ns and 48 ns for VESUVIO and ROTAX, respectively.

3.2 RESULTS

An example of recorded waveforms from the two detectors is shown in Figure 3.3. The different polarity is due to the use of the two different preamplifiers (DBAIII is inverting, DBAIV non-inverting). Typically many narrow pulses (each about 10 ns long) are recorded in every 2500 ns long waveform. Several

pulses can be recognized in Figure 3.3 with pulse height (h_p) values ranging from noise level (rms=10 mV for the DBAIII, and 6 mV for the DBAIV) up to hundreds of mV. A dedicated Python [37] code was used for off-line

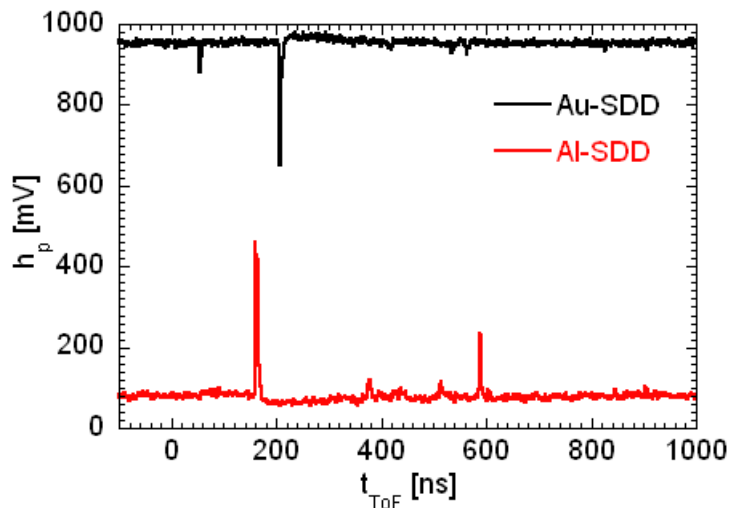


Figure 3.3: Data from the recorded waveform for the Au-SDD (black) and for the Al-SDD (red). The full waveform is 2500 ns long.

analysis to extract information on pulse height h_p , amplitude A (i.e. the area under the pulses in Figure 3.3) and Time of Flight (t_{ToF}) from the measured waveforms. The analysis is based on identification of all data points exceeding a threshold value (usually 30 mV) above the average offset level. These are tagged as events and $N=12$ data points around the pulse height maximum are used for each event to determine the pulse amplitude. The baseline is determined for each event from the 6 data points preceding the pulse and subtracted before computing the pulse amplitude. The time at maximum pulse height is used as t_{ToF} value. It is important to note that the amplification and digitization approach used here was optimized for speed rather than pulse height resolution; hence the pulse height resolution is modest. To reduce the uncertainties the integral pulse height or amplitude A was obtained from the sum of the N data points for each event and used as a measure of the energy deposited in the SDD.

3.2.1 ENERGY CALIBRATION

Energy calibration of the Au-SDD coupled to DBAIV was performed using a ^{241}Am α -source in air after the experiments at ISIS. The calibration results are shown in Figure 3.4. The peak position is 589 mVns and the FWHM

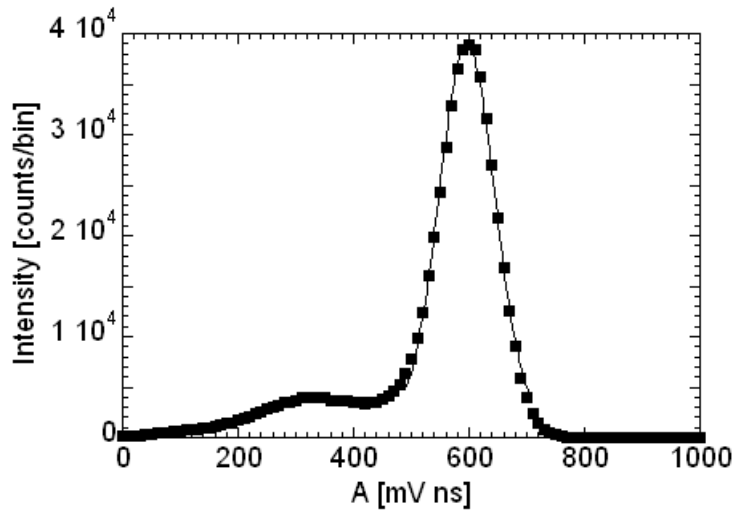


Figure 3.4: Calibration peak for the Au-SDD with ^{241}Am source. The line is a Gaussian fit to the data. The Gaussian parameters are height $I=4 \cdot 10^4$, FWHM=119 mVns, position $A=589$ mVns.

is 119 mVns or 20%. This a large FWHM compared to usual performance of these detectors [19] and is due to the data digitization and analysis used. Assuming an α energy of 5.2 MeV (5.5 MeV less the energy loss in 3 mm of air), we get a calibration coefficient of $8.9 \cdot 10^{-3}$ MeV/(mVns) that was used to convert A values to equivalent deposited energy E_d . The error in the calibration coefficient is mainly systematic and estimated to be $\approx 10\%$. A second energy calibration was performed during the experiments at ISIS for both detectors. Due to the lack of available calibration α -particle sources at the measurement location, the alpha decay of a natural uranium foil was used as a calibration reference (thin uranium foils are in regular use at the VESUVIO beam line). The measured α -particle spectra are shown in Figure 3.5 for both detectors. For the Au-SDD the spectrum appears as a single peak at $A=305$ mVns even though it is due to α -particles of energy 4.23, 4.67 and

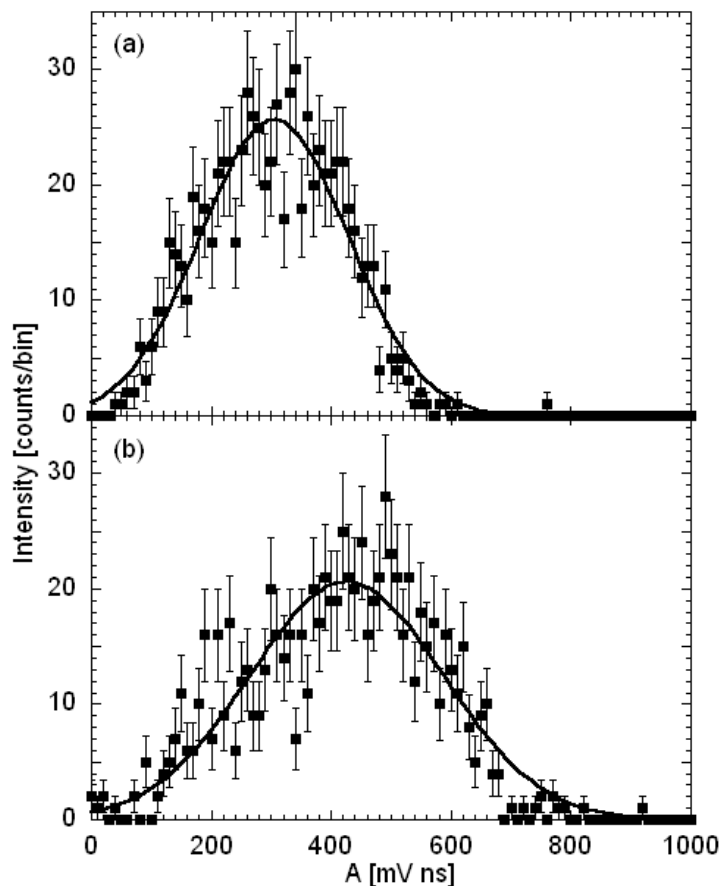


Figure 3.5: Calibration peak for the Au-SDD. The data are the amplitude spectrum from a natural uranium source with statistical error bars. The line is a Gaussian fit to the data. The Gaussian parameters are height $I=25$, width $W=305$ mVns (FWHM), position $A=305$ mVns. (b) Same as (a) but for the Al-SDD. The Gaussian parameters are $I=20$, $W=435$ mVns, $A=420$ mVns

4.85 MeV. The FWHM value happens to be the same as the peak position and is much larger than the distance between the different α -particle peaks. It is also much broader than the statistical broadening. For the Al-SDD the situation is similar, with $A=435$ and $FWHM=420$. The large FWHM values are due to the poor quality of the uranium foil as a calibration source: especially the foil thickness of $30\ \mu\text{m}$ and the poor collimation have the effect of decreasing the average energy and broaden the distribution. The result is that the peak position for the Au-SDD is about 60% lower than expected.

Still the relative peak positions for the two detectors are consistent with the different amplification settings: DBAIV (without preamplifier) provides a gain of about 200 whereas DBAIII + custom amplifier provide a gain of 320. The calibration of the Al-SDD was therefore calculated by considering the ratio between the peak position obtained with ^{nat}U measurements with Au-SDD and Al-SDD. We get a calibration coefficient of $5.6 \cdot 10^{-3} \text{ MeV}/(\text{mVns})$ for the Al-SDD.

The relation between measured pulse height h_p and integral amplitude A

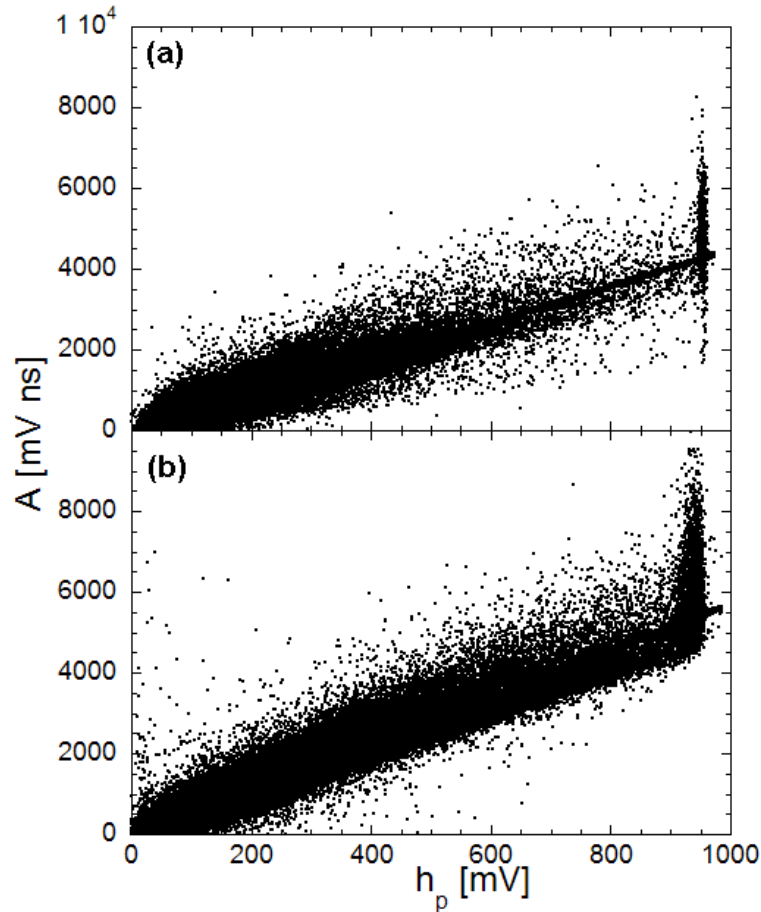


Figure 3.6: Scatter plot of A vs h_p for a subset of the data collected with the Au-SDD placed in the VESUVIO neutron beam. The line is a linear best fit to the data. (b) same as (a) but for the Al-SDD. The total number of data points is $1.6 \cdot 10^6$ in (a) and $3.9 \cdot 10^6$ in (b).

is shown by the scatter plot of Figure 3.6 which includes a subset of all

data collected with the Au-SDD and Al-SDD placed in the VESUVIO neutron beam. The data extend up to the maximum h_p values allowed by the digitizer input (including some offset). A very small fraction of the events ($<0.1\%$) saturates the digitizer input for the Au-SDD and was rejected from the analysis. The fraction of saturated events is larger for the Al-SDD ($\approx 0.5\%$). This suggests that the data quality of Al-SDD at high E_d values (say, $E_d > 30$ MeV) may be less good than for the Au-SDD. In both cases the data show a large scatter around an average linear relation $A = \tau \cdot h_p$ with $\tau = 5.6$ ns and 6.9 ns for the Au-SDD and Al-SDD, respectively. This is consistent with the use of a second amplification stage for Al-SDD slightly broadening the pulse shape. Taking into account the energy calibration of the detectors a pulse height value of $h_p = 1$ V translates to an energy of 50 MeV and 38 MeV for the Au-SDD and Al-SDD, respectively. The maximum deposited energy recorded by the two detectors is somewhat higher because of the calibration error ($\approx 10\%$). The threshold pulse height of $h_p = 30$ mV translates to an energy of 1.49 MeV and 1.16 MeV for the Au-SDD and Al-SDD, respectively. These values set the maximum and minimum deposited energies in our measurements. Note that neither limit is sharp. For instance the threshold $h_p > 30$ mV does not correspond to a sharp cut in the events plane in Figure 3.6. This is because the threshold is relative to an average offset whereas the actual offset subtracted to each event is different. The upper energy limit is more clearly recognizable in Figure 3.6 due to the cluster of events with saturated pulse height.

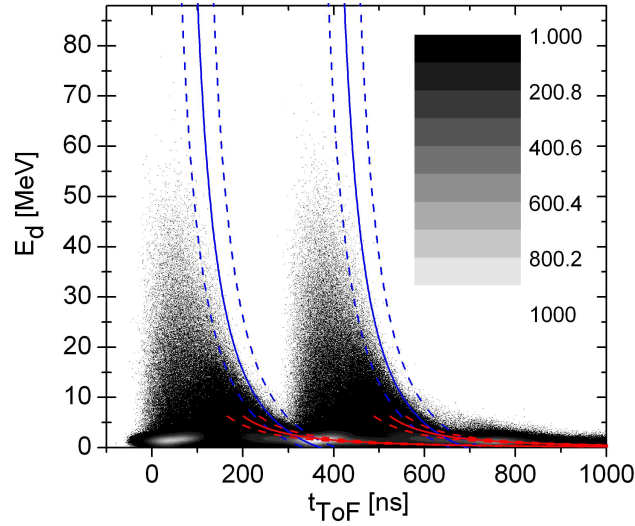
By counting the pulses above a certain h_p threshold it was possible to test the detector stability. The neutron count rate for $h_p > 150$ mV (i.e. $E_d > 5.8$ MeV) was found to be stable at the percent level for a period of 30 hours using the Al-SDD. The average count rate was 3.5 count/s. Since most of the events occur within 600 ns (see below) of the proton interaction with the target, the peak count rate can be estimated as $(50 \times 6 \cdot 10^{-7})^{-1}$ time the average count rate, or ≈ 100 kHz. The total count rate including events of lower deposited energy is much higher and exceeds 1 MHz for events with $h_p > 30$ mV. This suggests that the fast signal amplification and digitization is essential for successful operation of an SDD in the ISIS environment. The

total count rate of the Au-SDD and Al-SDD includes a large contribution from events of low pulse height and depends strongly on the h_p threshold value and on the way the data are processed. For this reason the total count rate varies by a factor 3 between the Au-SDD and Al-SDD even if their response at high E_d is similar (see below).

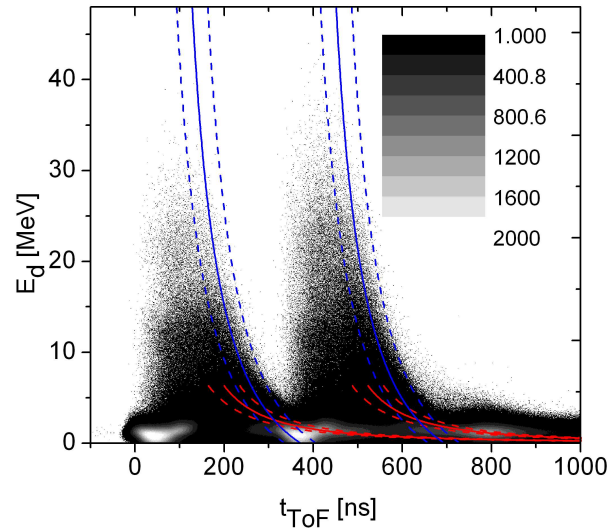
3.2.2 t_{ToF} VS E_d CONTOUR PLOT AND PROJECTIONS

Figure 3.7 shows the biparametric (t_{ToF} - deposited energy, E_d) contour plot recorded with the Al-SDD - DBAIII preamplifier -4X amplifier (a) and the Au-SDD - DBAIV preamplifier (b). The structure of the event distribution in the contour plot reflects the time structure of the two bunches in the proton beam. The events from the two bunches are well separated in time only for deposited energies $E_d > 10$ MeV. For lower E_d values the two bunches overlap. Note that the grey scale is reversed and the maximum event concentration corresponds to a white colour.

Some peak structures with >2000 (Al-SDD) and >900 (Au-SDD) events per bin can be recognized at E_d values below 5 MeV. The peak at about ($t_{\text{ToF}}=42$ ns, $E_d=2$ MeV) is associated with a strong flash of γ -rays coming directly from the moderator and spallation target. This peak was used for synchronization of the t_{ToF} axis since it provides a more stable reference than the proton signal from the accelerator. An identical peak is visible about 320 ns later and is due to the second proton bunch. A broader peak structure is also visible at longer t_{ToF} (≈ 800 ns). The same peaks are visible in the t_{ToF} spectra shown in Figure 3.8. One can see that the width of the two γ -ray peaks are about the same as the width of the proton signal peaks shown for comparison. The peak at ≈ 800 ns is comparatively broader. The differences in the detailed shape of the t_{ToF} spectra are mainly due to low pulse height events contributing differently to the count rate in the two detectors.



(a)



(b)

Figure 3.7: Contour plot of the event density in the (t_{ToF}, E_d) plane for the Au-SDD (a) and the Al-SDD (b). The total number of events in the plot is $2 \cdot 10^7$ (Al-SDD) and $6.7 \cdot 10^6$ (Au-SDD). The bin width is 1 ns in t_{ToF} and 0.089 (Au-SDD), 0.057 (Al-SDD) MeV in E_d . The integrated proton beam current was 4.401 mAh corresponding to a data collection time of 32h. The blue and red lines are the maximum deposited energy for the case of $^{12}\text{C}(n, \alpha)^9\text{Be}$ and elastic $^{12}\text{C}(n, n')^{12}\text{C}$ scattering reactions, respectively. The dashed lines are the same as the full lines but with a shift of ± 35 ns in the t_{ToF} value.

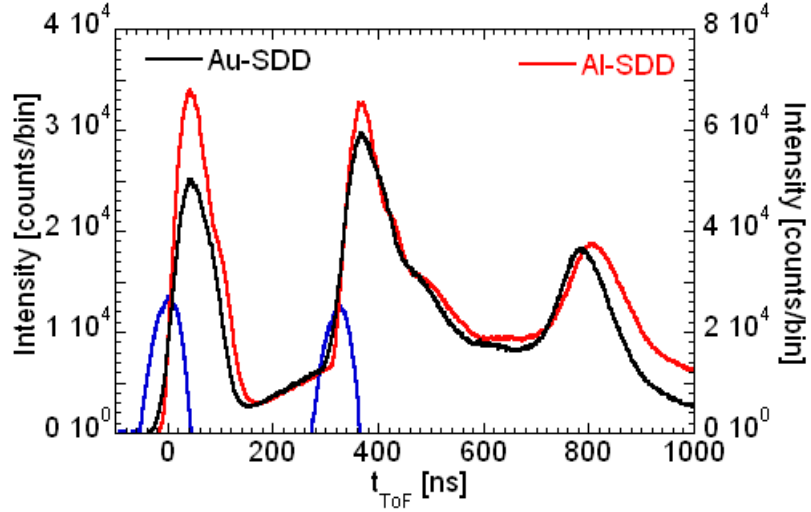


Figure 3.8: Time of flight spectrum for the two detector-amplification combinations used. The black line represents the spectrum for the Au-SDD - DBAIV preamplifier obtained by projecting the data of Figure 3.7 on the horizontal axis. The red line is the same but for Al-SDD - DBAIII preamplifier - 4X amplifier combination. Also shown in blue is the proton pulse signal from the accelerator in arbitrary units.

Figure 3.9 shows the E_d spectrum obtained by projecting the events in Figure 3.7 on the vertical axis. Both spectra feature a peak at low energies ($E_d \approx 2$ MeV) and a long tail. The tail is shorter for the Al-SDD as expected due the larger signal amplification for Al-SDD resulting in the limit in deposited energy of $E_d=40$ MeV. In the range $3 \text{ MeV} < E_d < 25 \text{ MeV}$ the two spectra are very similar. This appears to be the most promising range for use of the SDD as a neutron beam monitor and is further analysed below.

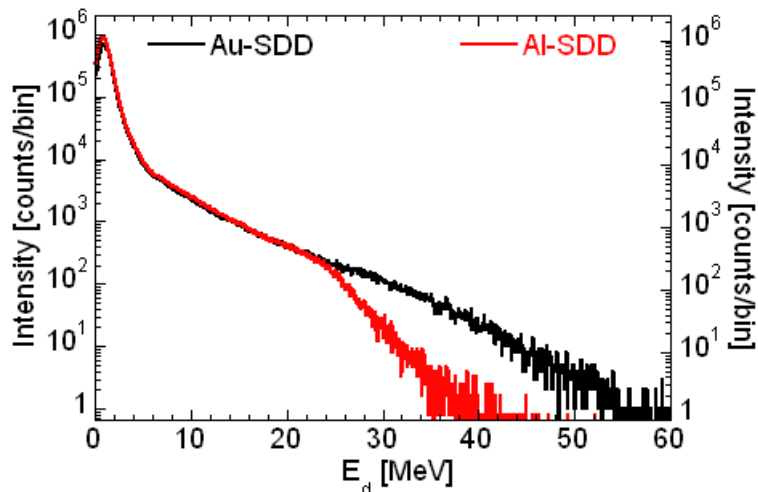


Figure 3.9: Spectrum of the deposited energy for the two detector-amplification combinations used. The black line represents the E_d spectrum for the Au-SDD - DBAIV preamplifier obtained by projecting the data of Figure 3.7 on the vertical axis. The red line is the same but for Al-SDD - DBAIII preamplifier - 4X amplifier combination. The E_d bin width is the same as in Figure 3.7. The vertical scales are adjusted to provide a good match between the two traces in the range $5 \text{ MeV} < E_d < 20 \text{ MeV}$.

3.2.3 COMPARISON WITH ROTAX

Data were also collected with the Au-SDD on the ROTAX [38] beam line where the flight distance is longer. The results are shown in Figures 3.10-3.12 and compared with results obtained on VESUVIO. The difference in the t_{ToF} spectra on ROTAX and VESUVIO is not surprising and is mainly due to the different flight path in the two beamlines. The longer flight path is manifested by a better separation between the events from the two proton bunches (320 ns apart in both cases). For instance in the region at $t_{\text{ToF}} \approx 400$ ns and low E_d the peaks due to photons and neutrons are resolved in ROTAX but not in VESUVIO.

The comparison between the E_d spectra in Figure 3.12 suggests that the neutron energy spectrum may be different in the two beamlines. In order to rule out instrumental effects the spectra on VESUVIO were collected with the same amplification chain coupled to either Au-SDD (black) or Al-

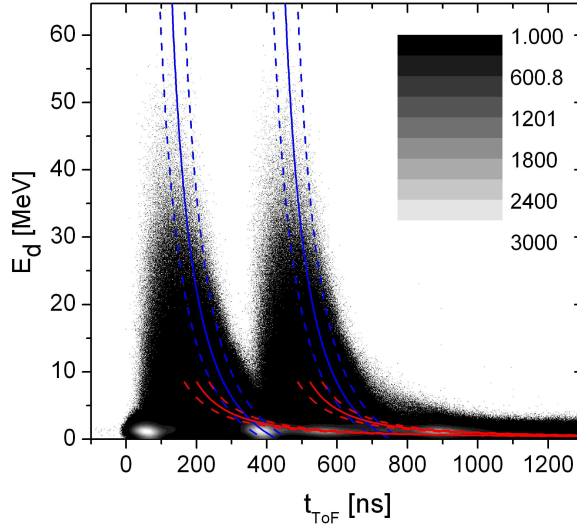


Figure 3.10: Contour plot of the event density in the (t_{TOF}, E_d) plane for the Au-SDD on the ROTAX beamline. The total number of events in the plot is $3 \cdot 10^7$. The bin width is 1 ns in t_{TOF} and 0.065 MeV in E_d . The integrated proton beam current was 11.7 mAh corresponding to a data collection time of 65h. The blue and red lines have the same meaning as in Figure 3.7 and were calculated assuming a flight distance $L=14.2$ m.

SDD (red). The measurement performed with the Au-SDD coupled to the DBAIII + Amp lasted 2 hours for a total number of events of $1.4 \cdot 10^6$ and an integrated current of 360 μAh . The spectrum measured with the Al-SDD is the same as in Figure 3.9. Apart from the different statistics the two VESUVIO spectra are identical for $E_d > 2$ MeV whereas the ROTAX spectrum has a somewhat different shape. The ROTAX spectrum can be scaled to match the VESUVIO spectra for $5 \text{ MeV} < E_d < 25 \text{ MeV}$ but the match is not accurate. This mismatch was not further investigated in this thesis but should be interpreted on the basis of detailed simulations of the target/moderator/collimation geometry for the two beamlines. Here we just point out that the VESUVIO and ROTAX beamlines view different moderators: the VESUVIO moderator is 300 K liquid water whereas the ROTAX moderator is 95 K methan moderator.

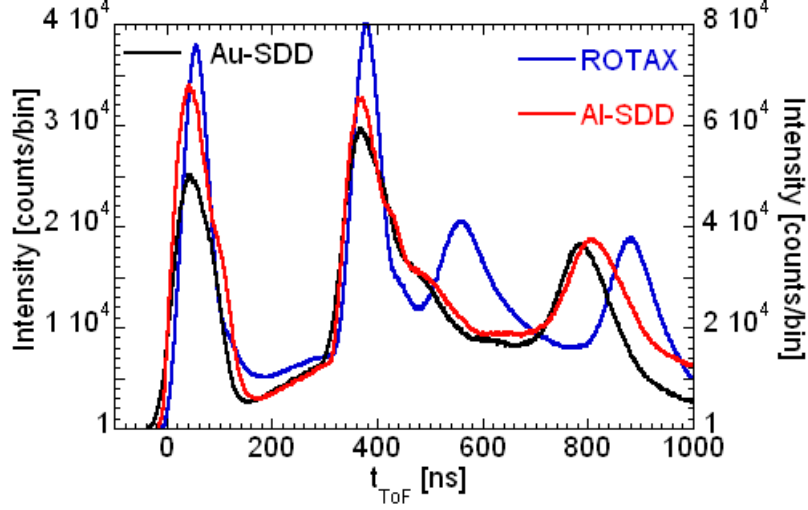


Figure 3.11: Time of flight spectrum for the Au-SDD - DBAIII preamplifier - 4X amplifier combination on the ROTAX beam line (blue). For comparison the spectra of Figure 3.8 are also shown.

3.2.4 BIPARAMETRIC ANALYSIS

The blue and red lines in Figure 3.7 provide a guide for understanding the observed event distribution in (t_{ToF}, E_d) space. The blue line is the maximum energy deposited by $^{12}\text{C}(n, \alpha)^9\text{Be}$ reactions of neutrons having the energy corresponding to the t_{ToF} value; i.e.

$$E_n[\text{eV}] = \left(\frac{72.2985 \cdot L_0[\text{m}]}{t_{\text{ToF}}[\mu\text{s}]} \right)^2 \quad \text{and} \quad E_d = E_n + Q \quad (3.1)$$

where E_n , E_d and the neutron mass are in energy units, c is the speed of light, $L=12.5$ m is the VESUVIO neutron flight distance and $Q=-5.7$ MeV is the reaction negative Q -value. Other break up reactions such as $^{12}\text{C}(n, n')3\alpha$ have a higher threshold and provide events that should fall below the blue curve. This is indeed what is observed for short flight times provided one takes into account the ± 35 ns time spread of the proton pulse illustrated by the dashed blue lines. For flight times longer than ≈ 300 ns, where E_n is low and $^{12}\text{C}(n, n')3\alpha$ is below threshold, there is a significant amount of events (best seen in the second bunch of events i.e. at $t_{\text{ToF}} > 700$ ns). This is where a

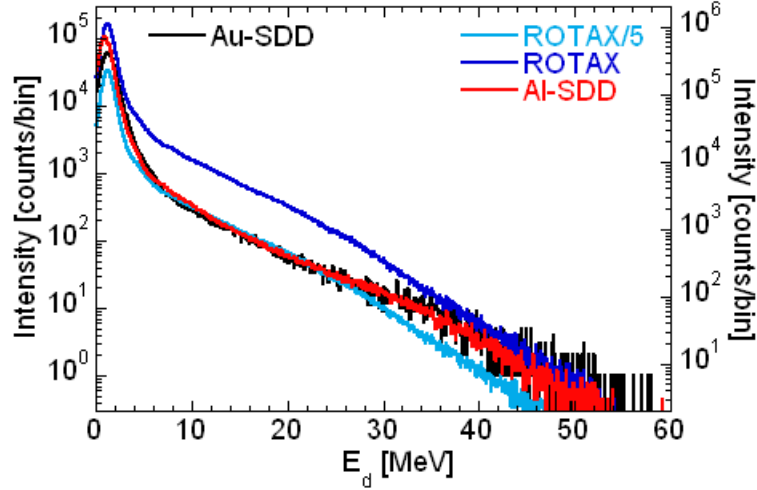


Figure 3.12: Spectrum of the deposited energy for the Au-SDD - DBAIII preamplifier - 4X amplifier combination on the ROTAX beamline (blue). The same spectrum divided by 5 is shown for comparison with spectra obtained on VESUVIO with the same amplification chain coupled to either Au-SDD (black) or Al-SDD (red). The vertical scales are adjusted to show a good match between the two data sets collected on VESUVIO.

broader peak structure is observed in Figure 3.7. A possible explanation for these events is that they are due to neutron elastic scattering off carbon. The recoiling carbon nuclei have a maximum energy (head on collisions) amounting to 28% of the incoming neutron energy. The corresponding E_d - t_{ToF} curve is shown in red in Figure 3.7. The t_{ToF} range where elastic scattering seems to be the main interaction process is $t_{\text{ToF}}=380\text{-}580$ ns. The corresponding neutron energy interval is $2.4 < E_n < 5.7$ MeV.

Further insight in the data can be gained by slicing the 2D data plot along lines of constant t_{ToF} or constant E_d . In Figure 3.13, the E_d spectrum for different neutron t_{ToF} is plotted. The t_{ToF} bin width was chosen equal to 5 ns in order to achieve sufficient statistics. The t_{ToF} values correspond to an (average) neutron energy equal to $E_n=21.1$ MeV ($t_{\text{ToF}}=200$ ns), $E_n=13.3$ MeV ($t_{\text{ToF}}=250$ ns), $E_n=9.2$ MeV ($t_{\text{ToF}}=300$ ns). There is a clear correlation between average E_n and maximum E_d . A more quantitative analysis of the spectra would require knowledge of the SDD response to monoenergetic neu-

trons folded with the relatively broad time distribution of the protons. t_{ToF}

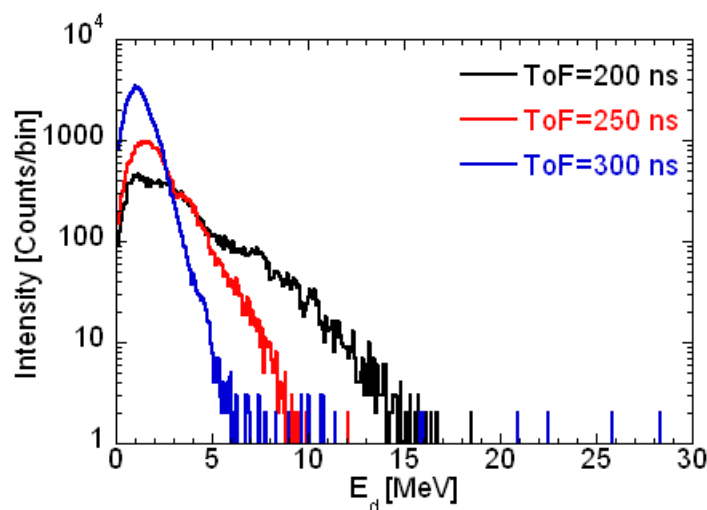


Figure 3.13: E_d spectrum for the Au-SDD for the t_{ToF} values reported in the legend. The t_{ToF} bin width is 5 ns. The E_d bin width is 0.089 MeV.

spectra obtained for larger E_d thresholds are shown in Figure 3.14. Again a clear correlation between t_{ToF} and E_d is observed: the maximum t_{ToF} is shorter for the higher energy. A neutron that deposits 10 MeV in the SDD should have $E_n > 15.7$ MeV; that is $t_{\text{ToF}} < 230 \pm 35$ ns. A neutron that deposits 20 MeV should have $E_n > 25.7$ MeV, i.e. $t_{\text{ToF}} < 182 \pm 35$ ns. The spectra in Figure 3.14 are in qualitative agreement with the above t_{ToF} limits. Again, for a quantitative analysis knowledge of the SDD response to monoenergetic neutrons is needed. Future work will include the improvement of the data reduction for optimal energy resolution before the SDD response function is determined at a suitable neutron source.

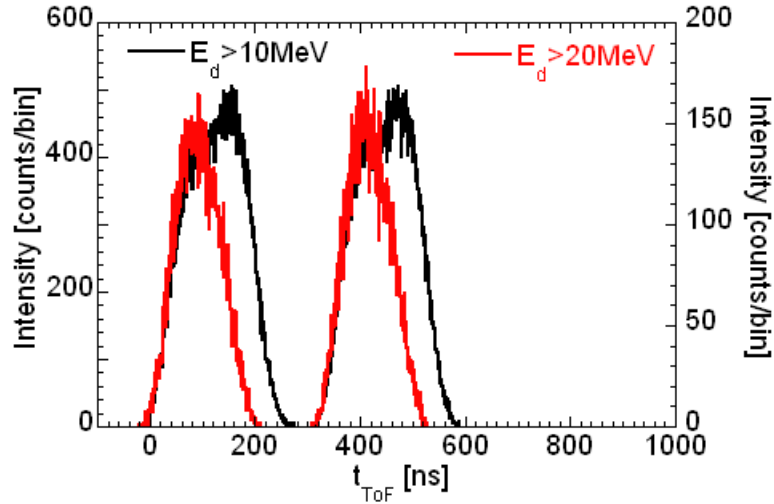


Figure 3.14: t_{ToF} spectrum for the Au-SDD for the E_d intervals reported in the legend. The t_{ToF} bin width is 1 ns.

3.2.5 BEAM PROFILE MEASUREMENTS

The last measurement performed at the VESUVIO with the Al-SDD coupled to the DBAIII was a horizontal scan of the detector position in order to determine the spatial profile of the neutron flux. Figure 3.15 represents the horizontal beam profile for different regions in the (t_{ToF}, E_d) space. The number of events were normalized to the integrated current. Three regions are considered:

- $E_d < 5$ MeV and $t_{\text{ToF}} < 75$ ns. Here the events are mainly due to photon interactions. The profile width (FWHM) is $W=48$ mm
- $E_d > 5$ MeV, $200 < t_{\text{ToF}} < 250$ ns. The events in this range are mainly due to inelastic n-C reactions with intermediate E_n values. The profile width (FWHM) is $W=36$ mm
- $E_d > 15$ MeV. This region includes events due to high energy neutrons. The profile width (FWHM) is $W=41$ mm

The differences in profile width are well outside the uncertainties in the measurement. It would be interesting to compare the results with model simulations of the neutron and γ -ray collimation along the VESUVIO beam line.

This simulation work will be addressed in the future. Once the SDD re-

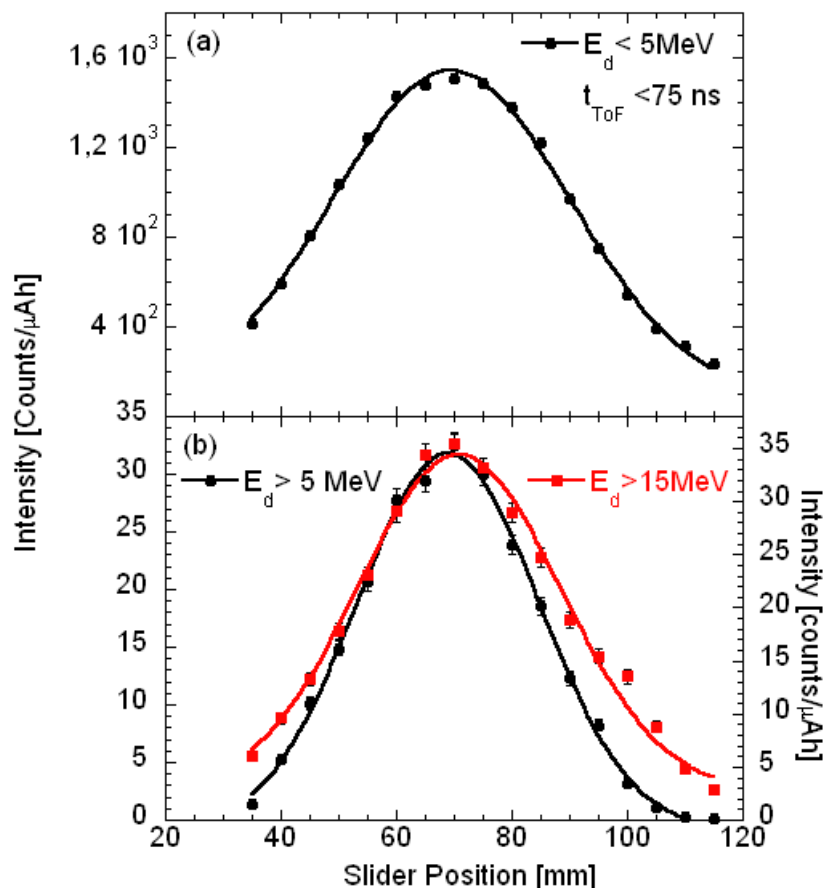


Figure 3.15: Horizontal beam profile obtained by selecting events with (a) $E_d < 5$ MeV and $t_{\text{ToF}} < 75$ ns, (b) $E_d > 5$ MeV, $200 < t_{\text{ToF}} < 250$ ns (black), and $E_d > 15$ MeV (red). Each point corresponds to a 15 minute long run. The integrated current was typically 45 μAh in each point. The lines are a Gaussian fit to the data.

response to monoenergetic neutrons becomes available it should be possible to unfold the biparametric spectrum and determine the beam profile as function of neutron energy. This will be especially interesting on the ChipIr beam line where different modes of operation will be available providing a range of beam profiles. The measurement of the beam profile at different neutron energies will be a powerful benchmark for the neutron transport simulations on which the ChipIr beam line design is based.

3.3 CONCLUSIONS

The performance of a single crystal diamond ($4.7 \times 4.7 \times 0.5 \text{ mm}^3$ active volume) detector was tested in the ISIS pulsed neutron beam using a fast biparametric data acquisition. Three characteristic regions in the biparametric spectra were observed: i) low pulse height events with very short time of flight induced by γ -rays; ii) low pulse height events at longer flight times (i.e. neutron energies $E_n > 3.5\text{-}6 \text{ MeV}$), possibly due to neutron elastic scattering off ^{12}C ; iii) events with large pulse height and flight times corresponding to $E_n > 6 \text{ MeV}$ mainly due to inelastic reactions such as $^{12}\text{C}(n, \alpha)^9\text{Be}$ and $^{12}\text{C}(n, n')^3\alpha$. The SDD is a promising detector in view of applications to the ChipIr neutron beam line for fast neutron irradiation of electronic components at ISIS. Applications to be further investigated with the help of response function measurements and neutron transport simulations include beam profile measurements, beam intensity monitoring and measurements of the neutron energy spectrum in a broad range of fast neutron energies.

Chapter 4

Simulations of neutron production and transport in SPIDER

The neutron detection system proposed as a beam diagnostic for SPIDER will measure the map of the neutron emission from the SPIDER beam dump. In this chapter the neutron emission process is investigated with the help of simulations.

4.1 SIMULATIONS OF DEUTERIUM BEAM INTERACTION

In SPIDER a beam of 100 keV deuterium ions will collide against the beam dump inclined by 30° relative to the beam axis. The total beam current of 40 A is thus spread out over a surface of $\approx 1 \text{ m}^2$ for a reference average current density of 40 A/m^2 and deuterium flux of $2.5 \cdot 10^{20} \text{ D/m}^2 \cdot \text{s}$. The beam dump has a depth much larger (tens of mm) than the deuterium deposition layer. Earlier studies [39] indicate an expected neutron production for 100 keV deuterons on saturated copper alloy of $\approx 3 \cdot 10^7 \text{ n/mAs}$ (see Figure 4.1). This gives a total neutron production per SPIDER pulse (lasting 3600 s) of up to $\approx 4 \cdot 10^{15}$ neutrons.

In order to confirm these values a Local Mixing Model (LMM)[40]) was used to predict the evolution of deuterium ions implanted on the SPIDER beam

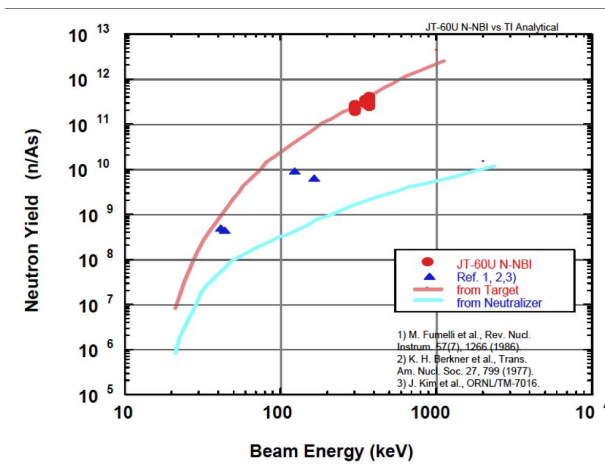


Figure 4.1: Predicted (lines) and measured (symbols) neutron yield from copper beam dump at deuterium beam facilities [39].

dump. The computer program TRansport of Ion in Matter (TRIM)[16] was used to determine the range distributions and energy loss of the implanted deuterium inside the target material and the target damage due to the deuterium ions bombardment.

4.1.1 DEUTERIUM IMPLANTATION PROFILE

Deuterium beam interaction was simulated using the TRIM program. In this MonteCarlo code, the interactions of energetic ions hitting the target material are described by i) collisions with electrons where energy is lost but the direction of motion is not changed (inelastic energy loss) and ii) elastic collisions with nuclei where both energy and direction of motion are changed. The trajectories of 10^6 deuterium ions with an initial energy $E_0=100$ keV and incidence angle equal to 60° relative to the normal to the CuZrZr-alloy target surface have been simulated. The projection of the trajectories in a plane normal to the surface of bombardment is shown in Figure 4.2. When energetic particles impinge on a solid surface, a fraction of them is backscattered retaining part of their initial energy. Besides, when the incident particle or a target recoiling atom reaches the target surface there is the possibility that a solid atom could be ejected from it (physical sputtering). About 95% of the

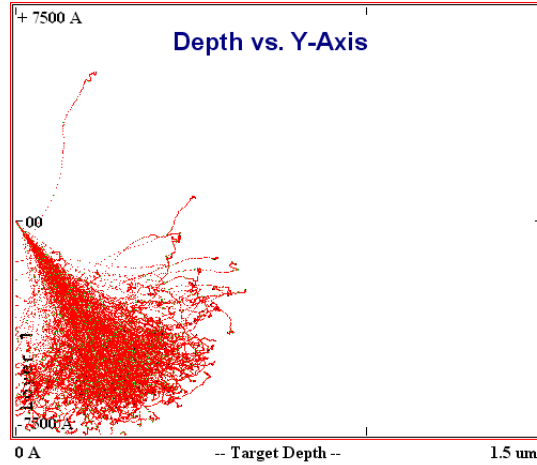


Figure 4.2: Planar projection of ion trajectories generated by a TRIM simulation for 100 keV deuterium and 60 degrees incidence in CuCrZr-alloy.

deuterons penetrate (by up to $1\ \mu\text{m}$) in the beam dump and can contribute to the neutron emission. The deuterium deposition profile, i.e. deuterium ion distribution across the target, is shown in Figure 4.3 as function of the target depth (z). The plot ordinate $P(z)$ represents the probability than an incident ion comes to rest at depth z in the element length dz . According to the TRIM results of Figure 4.3 all deuterium ions are deposited within a depth of $0.8\ \mu\text{m}$ from the target surface; the ion projected range in the target solid is nearly $0.3\ \mu\text{m}$.

4.1.2 ION ENERGY LOSS

The energy loss of ions by collision with the target electrons is called *electron energy loss* or *ionization loss*. It constitutes the main channel of energy loss for the incident ions. Other sources of energy loss are due to the collisions with the solid nuclei: if the target atom retains enough energy it will leave the lattice site and will continue to loose energy as the incident ions. If the imparted energy is less than the displacement energy, the target atoms return to the original site by loosing their energy by lattice vibrations (energy loss by phonons). According to TRIM results, 97% of the initial ion energy is

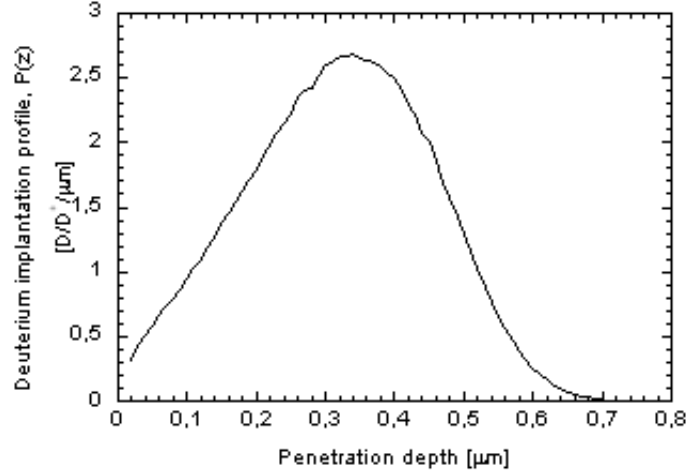


Figure 4.3: Penetration depth distribution of implanted deuterium in the beam dump.

lost by ionization, $\approx 0.1\%$ by elastic collisions from ions or displaced target atoms, the rest by phonon energy loss. Figure 4.4 shows the ionization energy loss of the incident ions and of the recoiled atoms versus the target depth. Most of the ion energy is deposited in the target very close to its surface. The integral of the energy loss of the ions with respect to the target depth gives the total energy deposited by one incident ion. The average ion energy as function of target depth was determined and it is shown in Figure 4.5 as fraction of the incident energy E_0 . This quantity is used in the next section to determine the neutron emissivity from fusion reactions between deposited deuterium and incident deuterium.

4.1.3 ION DAMAGE AND DEUTERIUM CONCENTRATION IN THE BEAM DUMP

During the slowing down of the incident ion each nuclear collision will transfer energy to the target atoms. At sufficiently high energy transfer, the *primary* knock-on atom may create a collision cascade and further material defects. A relatively large energy is required to move a target atom far enough from its original site in order to create a vacancy and an interstitial that do not

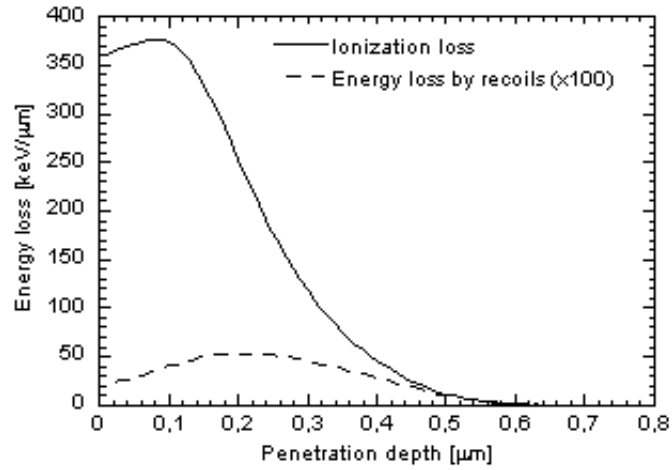


Figure 4.4: Electronic (ionization) energy loss of deuterium ions vs penetration depth. Also shown is the energy loss due to recoiling target atoms (x100).

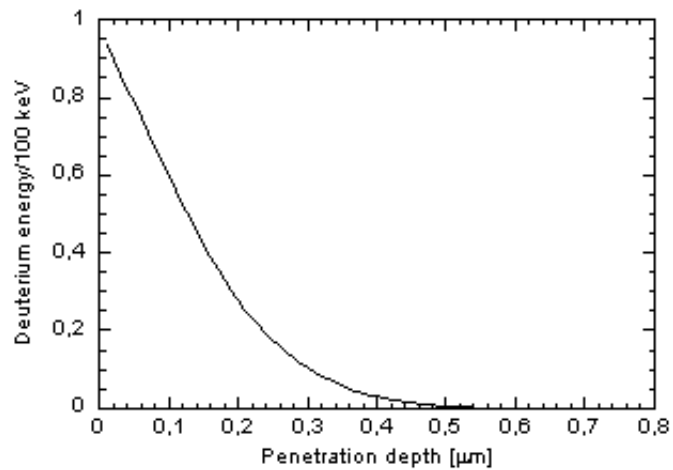


Figure 4.5: Average deuterium energy as fraction of the incident energy ($E_0=100$ keV) as function of penetration depth.

recombine (Frenkel pair). The TRIM code calculates the number of target atoms displacements per incident ion (either made by the ion itself or by all the recoiling target atoms). The results from TRIM are multiplied by the ion fluence to determine the damage profile in displacements per atom (dpa). Figure 4.6 shows the damage profile versus target depth at different implan-

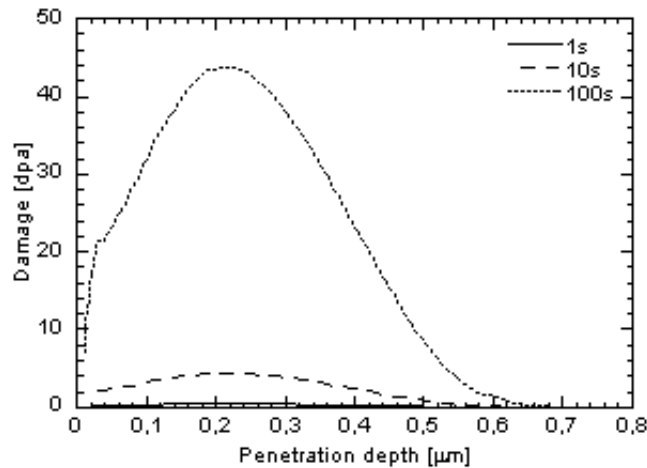


Figure 4.6: Ion damage (displacements per atom) at different times after switch on of the deuterium beam.

tation times for a reference deuterium incident flux of $2.5 \cdot 10^{20} \text{D}^+ / \text{m}^2 \text{s}$. After a deuterium bombardment of $t=100 \text{ s}$ the damage becomes larger than 10 dpa (vacancies) within $0.5 \mu\text{m}$ from the surface. As shown in Figure 4.6, the damage rate near the surface of the target becomes very high and it is probably accompanied by a highly damaged state of the material, with the formation of bubbles, microchannel networks and cracks all over the deuterium implantation zone [41].

Due to the high damage rate in the target, the implanted deuterium ions are suddenly trapped in the material defects. In this situation the diffusivity or the detrapping of the implanted deuterium are small and high concentrations of the implanted deuterium can build up. Clearly the material cannot accommodate an arbitrarily high concentration of implants. There is experimental evidence of release of the implanted gas over a certain value of fluence.

It implies a saturation level on the hydrogen concentration within the material. The LMM is a simple model for *local saturation*, in which the bulk concentration, $c(z)$ of implanted deuterium at depth z from the surface is limited to a maximum (or saturation) value, c_s [42]. In case of implantation of a single hydrogen isotope the LMM model simplifies to:

$$\frac{dc(z)}{dt} = \phi \cdot P(z) \quad (4.1)$$

when $c(z) < c_s$, and:

$$\frac{dc(z)}{dt} = 0 \quad (4.2)$$

when $c(z) = c_s$. Here $P(z)$ is the implantation profile (4.3) and $\phi = 2.5 \cdot 10^{20} \text{ D}^+/\text{m}^2\text{s}$ is the assumed flux of incident deuterium. It is easy to integrate the above equations given the deuterium profile as function of depth z and the implantation time t :

$$c(z, t) = \min[\phi \cdot P(z) \cdot t, c_s] \quad (4.3)$$

The deuterium concentration profiles are given in atomic fraction (*at.fr.*), i.e. number of deposited deuterium atoms per solid atom. From experiments on hydrogen implantation in copper, a typical value is $c_s \approx 20\%$ at.fr. [40]. With this choice of saturation value the implantation profile in Figure 4.3 gives the deuterium profiles shown in Figure 4.7. The concentration profile has a peak at $\approx 0.3 \mu\text{m}$, equal to the deuterium range in the copper alloy, shown in Figure 4.3. Deuterium saturation is first reached after ≈ 30 s of bombardment. After 100 s the deuterium is saturated from 0.07 up to 0.5 μm , and if we consider an irradiation time greater than 200 s the deuterium concentration is fully saturated up to a penetration depth of 0.7 μm .

The LMM does not include temperature effects for the evaluation of the deuterium profile in highly bombarded targets. It has been found that the saturation level, c_s , may depend on temperature for some materials like carbon [43]. The possibility of hydrogen thermal release from a saturated solid layer has been included in a *extended* LMM version [42][41]; however the extension means that several additional parameters enter the model, which

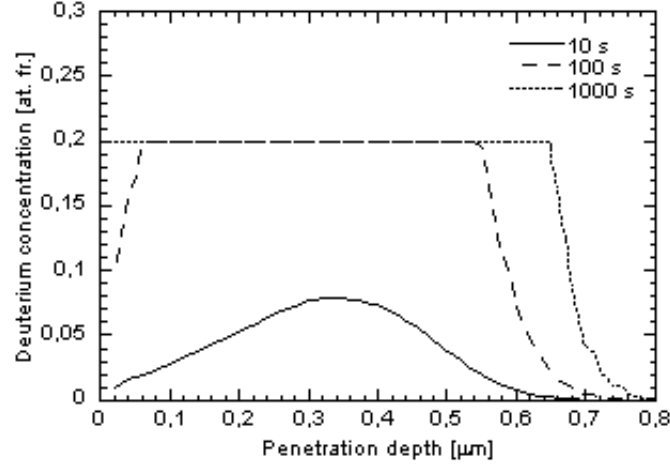


Figure 4.7: Deuterium concentration profile at different times after switch on of the deuterium beam.

can only be determined by experimental measurements. Another effect that has to be considered is the tritium production in the beam dump due to DD reactions. These effects are believed to be small and have not been taken into account here.

4.2 NEUTRON PRODUCTION IN SPIDER BEAM DUMP

The neutron emissivity at a given point (x, y, z) in the beam dump can be written as:

$$y = \phi(x, y, z) \cdot \sigma \cdot n_d \quad (4.4)$$

where $\phi(x, y, z)$ is the deuteron flux entering the dump, $\sigma(E_d)$ is the cross section for the DD reaction and $n_d(x, y, z)$ is the density of deuterium nuclei in the dump. The latter can be obtained by multiplying the atomic density (n_{Cu}) in the dump copper alloy by the deuterium concentration profile $c(x, y, z, t)$:

$$n_d = n_{Cu} \cdot c \quad (4.5)$$

The map of deuterium flux $\phi(x, y)$ was calculated and shown in chapter 1 (Figure 1.13) for stable beam conditions. The peak flux is $\phi = 2.5 \cdot 10^{20}$

$D^+/\text{m}^2\text{s}$, and is lower by about one half between adjacent beamlets. A lower flux implies a longer time for the concentration profile to reach the saturation value, as indicated in formula 4.3. Thus, non-uniformity in deuterium flux affects the neutron yield: both directly (y is proportional to ϕ) and indirectly because of the c dependence on the deuterium flux.

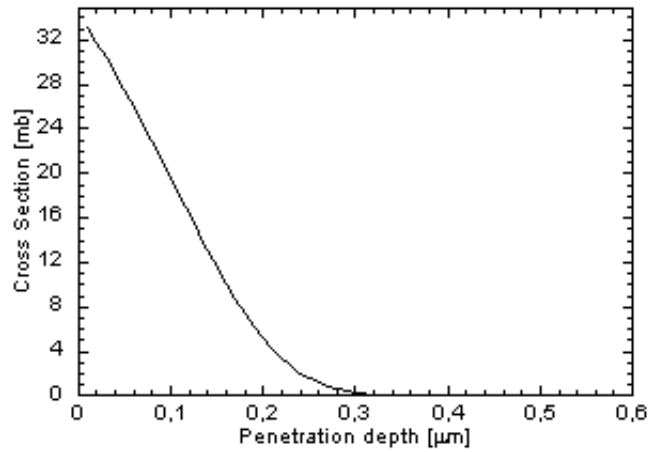
We are not interested in resolving the details of the neutron emissivity within a beamlet footprint. This means that the diagnostic performance can be assessed on the basis of a simplified model for the global neutron emission inside the dump. The model is based on the average deuteron behavior inside the dump. Each deuteron is assumed to slow down in the dump according to the energy distribution shown in Figure 4.5. Thus our model is based on two simplifying assumptions: i) the deuteron flux is independent of z and ii) the flux level is fixed and it is $\phi = 2.5 \cdot 10^{20} D^+/\text{m}^2\text{s}$. This gives the concentration profiles of Figure 4.7 where the chosen flux value affects the time scale but not the profile shapes.

4.2.1 NEUTRON EMISSIVITY

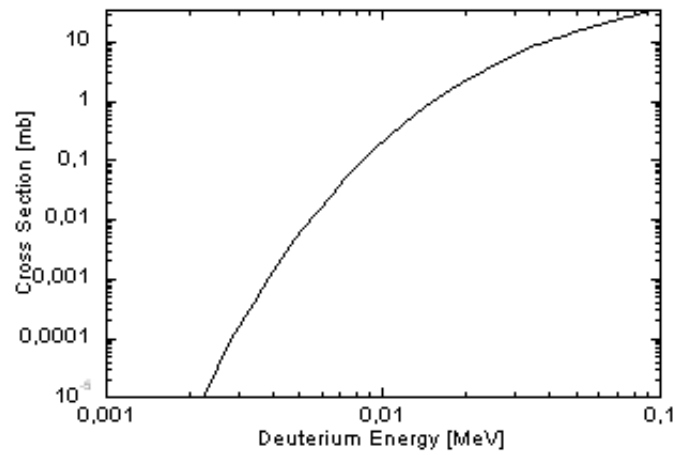
The DD cross section can be expressed as a function of the penetration depth z via the relationship between the cross section and the deuterium energy reported in [44]. The cross section as a function of the deuterium energy and the penetration depth is reported in Figure 4.8(a) and (b), respectively.

Using formula 4.4 the neutron emissivity has been calculated as a function of the penetration depth for different irradiation time. In Figure 4.9 the neutron emissivity as a function of the penetration depth is reported for different irradiation times (see Figure 4.9). According to the model the neutron emissivity has a position-dependent saturation level. For low irradiation times ($< 30\text{s}$) the saturation is not reached and there is no saturation point in the neutron emission profile. For longer irradiation times the neutron emission saturation occurs when the deuterium concentration profile reaches the value of 20% of n_{Cu} . For an irradiation time of 100 s the concentration reaches the saturation value at $0.1 \mu\text{m}$, therefore the neutron emissivity is highest at $0.1 \mu\text{m}$. Considering an irradiation time greater than 200 s, the deuterium

concentration is saturated up to $0.7 \mu\text{m}$ and the neutron emissivity is fully saturated over most of the profile. This means that after this irradiation time the neutron emissivity is only dependent on the deuterium beam intensity.



(a)



(b)

Figure 4.8: Cross Section for the $\text{D}(d,n)^3\text{He}$ reaction as function of deuterium energy (a) and of the penetration depth (b).

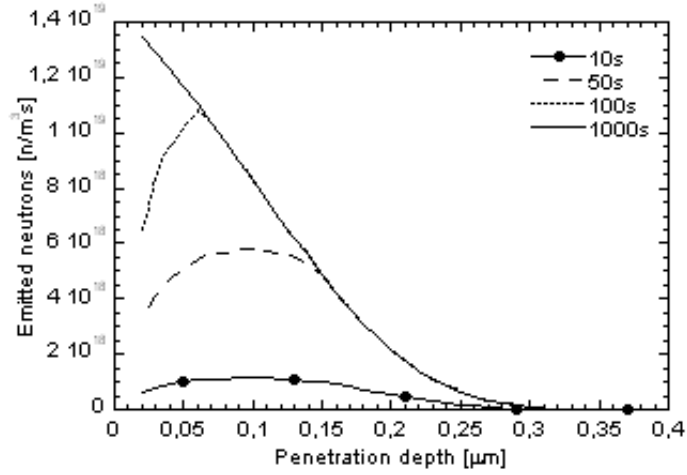


Figure 4.9: Neutron emission profile as a function of penetration depth (z) after the irradiation times reported in the legend.

4.2.2 SOURCE BRIGHTNESS

Equation 4.4 can be integrated along the penetration depth to give the neutron brightness of the source:

$$b = \phi \int \sigma \cdot n_D \cdot dz \quad (4.6)$$

The brightness (in units of n/m^2s) as a function of the irradiation time is reported in Figure 4.10. It features a linear growth lasting for about 50 s followed by an asymptotic approach to a saturation value of $1.4 \cdot 10^{12} n/m^2s$. At times longer than 200 s the brightness is fully saturated.

The values in Figure 4.10 are representative of the peak brightness point within a beamlet footprint, as already said in the previous subsection. The brightness will rise more slowly at the footprint boundary, reaching a lower saturation value in proportion to the local deuteron flux. The main outcome of the result of our model calculation is that

- About 3 minutes will be needed before the neutron emission reaches a steady state value in SPIDER. This time may be shorter depending on the initial deuteron concentration. The transient phase before satura-

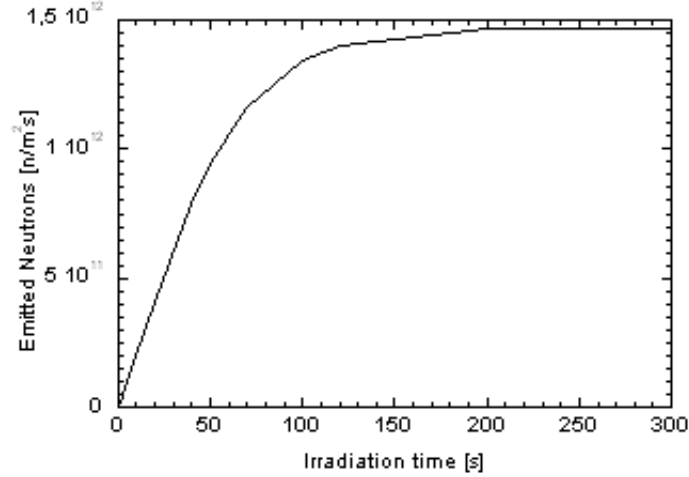


Figure 4.10: Neutron emission rate as a function of the irradiation time.

tion depends on the initial deuteron concentration in the dump and on the beam intensity.

- The saturation value of the neutron brightness depends mainly on the beam intensity. At full power the average neutron brightness will be $\approx 10^{12}$ n/m² · s if the saturation concentration value is 20%.

A neutron measurement system with a time resolution of 1 s or better and a spatial resolution able to separate the neutron emission from individual beamlets will be able to provide diagnostic information on the beamlet intensity. Relative intensity changes between beamlets will be reflected in their neutron brightness: the neutron brightness map is also a map of the beam intensity. The transient phase at the switch-on of the beams is expected to provide information on the deuteron implantation in the copper alloy (e.g. deuteron migration in the quiet phase between SPIDER pulses can be investigated).

4.3 NEUTRON TRANSPORT IN THE SPIDER BEAM DUMP

From what was shown in the previous section it is clear that neutron emission occurs on the beam dump surface up to a penetration depth of $0.8 \mu\text{m}$. Neutrons emitted must cross the dump in order to be detected on the back side, where our detector will be placed. A fraction of the neutrons is scattered in the process: in this section the results obtained from MCNPX simulations of scattering will be described. The effect of the beam dump on neutron transport was investigated using the MCNPX code. Many aspects of the neutron transport across the beam dump materials were investigated:

- The effect of the beam dump materials on neutron propagation. Simulations were performed with and without the beam dump in order to investigate the effect of scattering and adsorption in the copper-alloy and in the cooling-water.
- The effect of the mechanical support holding the beam dump in place.
- More generally, the contribution of the SPIDER vessel.

Neutrons bouncing back from the walls of the bunker, in which the experiment is contained, are mostly thermalised and have no effect on detectors of fast neutrons.

4.3.1 SIMULATIONS

The CAD model of the SPIDER beam dump was shown in Figure 1.10. The beam dump geometry can be approximated as a 2D slab with two layers of copper alloy separated by a layer of water (Figure 4.11). This model is adequate for assessing the importance of scattered neutrons and for designing the neutron diagnostic system.

Three panels parallel to the xz plane are inserted along the y -positive axis. Two of these panels are made from copper alloy (CuCrZn) and the one in

between is made from water. The panels are infinite in the x and z direction and have a thickness of 5.8 mm, 6.2 mm and 5.0 mm. The thickness was chosen in order to preserve the same volume ratio between copper alloy and water. A monoenergetic neutron source ($E_n = 2.5$ MeV) is placed in the axes origin (green point). The neutron detector was placed at a distance of 30 mm from the source. The detector is a flux monitor (MCNPX - mesh tally, type 1) of area of 200×350 mm² matching one of the SPIDER beamlet groups. The monitor was divided in a mesh of 2800 pixels of 25 mm² area. The frame which supports the beam dump panels was modelled into an iron column. This column is shown in grey in Figure 4.11. Instead of creating

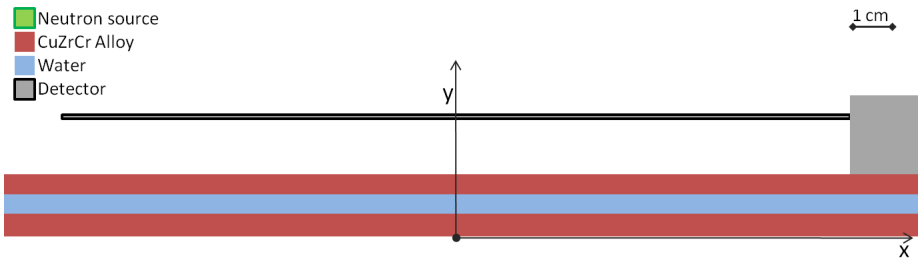


Figure 4.11: Cross section of the 2D beam dump model used for the simulations. In this example neutrons from a point neutron source (green) cross layers of copper alloy (red) and water (light blue) before reaching the detection surface (black) located at 30 mm from the source. also visible on the right is the cross section of a steel column (grey) used to estimate the importance of scattered neutrons from the beam dump support.

a comprehensive model of the beam dump geometry we separately analysed the key effects. This approach was preferred since it provides a better comprehension of the different processes. Therefore, three different sources have been implemented into the MCNPX code:

- An isotropic point source to calculate the spatial resolution;
- A point source with the DD reaction cross section anisotropy to evaluate its contribution to the spatial resolution;

- A planar source with an area equal to the detector dimensions in order to investigate the contribution due to the environment materials.
- A planar source with a single beamlet area in order to study the intensity of an individual beamlet compared to total (5×16 beamlets) beam intensity.

4.3.2 ANISOTROPY AND SPATIAL RESOLUTION

The DD differential cross section is anisotropic as shown in Figure 4.12: more neutrons are emitted along the deuterium beam direction than in the perpendicular direction.

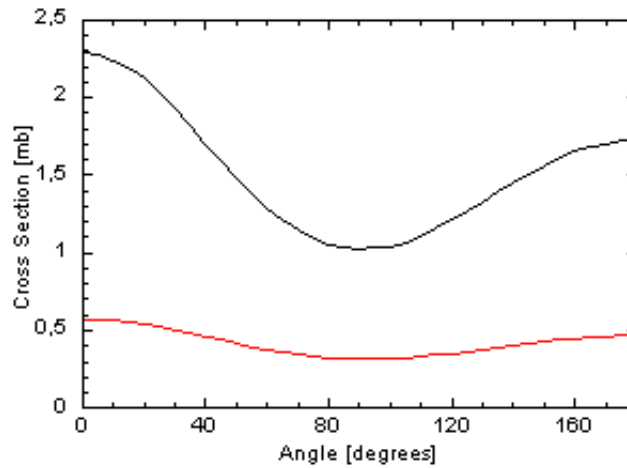


Figure 4.12: Differential Cross Section for the DD beam-target reaction with beam energies $E_d=50$ keV (red), and $E_d=100$ keV (black). [45]

In the range 0° - 90° the cross section can be approximated as:

$$\frac{d\sigma}{d\Omega} = a \cdot (1 + b \cdot \cos^2\theta) \quad (4.7)$$

where a and b are fit parameters and θ is the angle between the neutron and deuteron velocities. The anisotropy coefficient values are $b=0.82$ and $b=1.29$ at $E_D=50$ keV and 100 keV, respectively. Assuming $b \approx 1$ as a representative value for the whole energy range of interest, we find that the main effect

of the anisotropy is to shift the neutron intensity at the detection surface. To illustrate the effect we consider two cases where the intensity distribution

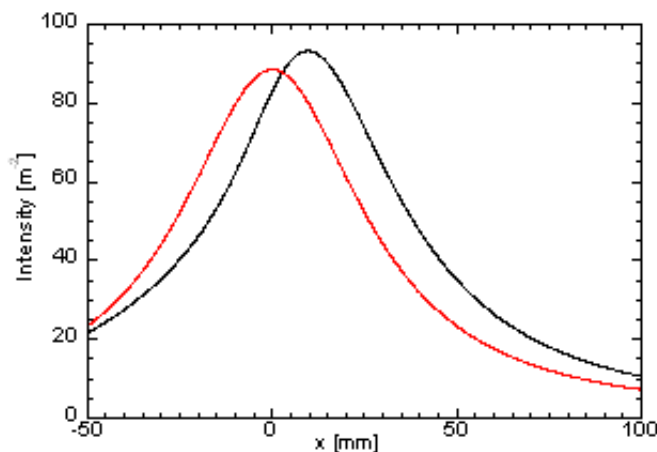


Figure 4.13: Neutron intensity at the detection surface as a function of position along the x axis. A point source of unit intensity is placed at 30 mm from the detection surface. The red line is the flux from an isotropic source. The black line is the flux from a unit source with an anisotropy coefficient $1+\cos^2\theta$ where θ is the angle relative to the deuteron beam direction.

from a point source of unit intensity is recorded on a detection surface placed at 30 mm from the source. In the case of an isotropic source the intensity varies along the x-axis reflecting the well-known $1/r^2$ dependence. This is shown by the red trace in Figure 4.13. In the second case the neutron emission has an anisotropy coefficient $1+\cos^2\theta$ where θ is the angle relative to the deuteron beam direction; the deuteron beam is assumed to run in the XY plane at an angle of 30° relative to the detection surface. The resulting intensity curve is shown as a black trace in Figure 4.13. The main effect is a 10 mm shift of the intensity peak whereas the peak intensity is changed by about 10% and the shape (width) change of the curve is at the 5% level. This simple model calculation provides an estimate of the effects that are neglected when assuming an isotropic neutron emission as is done in the MCNPX simulations below.

If we consider again the red line in Figure 4.13 we see that the intensity distribution has a FWHM (Full Width Half Maximum) of about 60 mm.

The width depends on the source-detector distance and can be considered as an effective spatial resolution or “point spread function” at the detector surface.

4.3.3 NEUTRON SCATTERING IN THE BEAM DUMP

The effect of neutron scattering in the beam dump is to modify the intensity distribution on the detector surface due to a point source as shown in Figure 4.14 (black line). Compared to the case without beam dump (red line), the intensity peak is slightly increased and the wings are decreased. Note that scattered neutrons are downgraded in energy (see below) and our simulation follows all neutrons until their energy drops below 0.2 MeV. The peak increase is due to a scattered neutron additional component that overcompensates the attenuation of the unscattered neutrons. In the wings attenuation is dominant due to the oblique path through the dump.

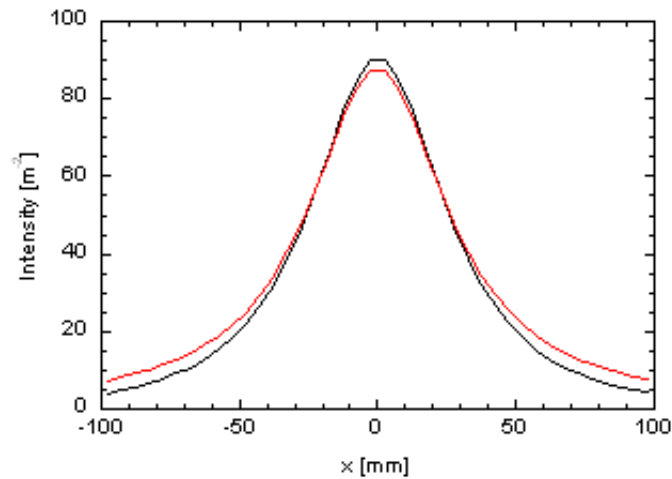


Figure 4.14: Neutron intensity at the detection surface as a function of position along the x axis. A unit point source is placed at 30 mm from the detection surface. The red curve is the same as in Figure 4.13. The black curve shows the effect of the beam dump placed between source and detector.

4.3.4 NEUTRON SCATTERING IN THE SPIDER MATERIALS

The effect of neutron scattering on the SPIDER materials surrounding the beam dump was investigated with the help of two simulations. The source used in these simulations is a planar source representing the beam dump area intercepted by one of the 16 SPIDER beamlet groups made of 5×16 beamlets, as modelled in paragraph 1.2.2. Each elliptical beamlet footprint is replaced here with a 22×40 mm² rectangle giving for the beamlet group a uniform plane source of area 200×352 mm². This is the same area as the detector surface used in the MCNPX model. The neutron intensity on the

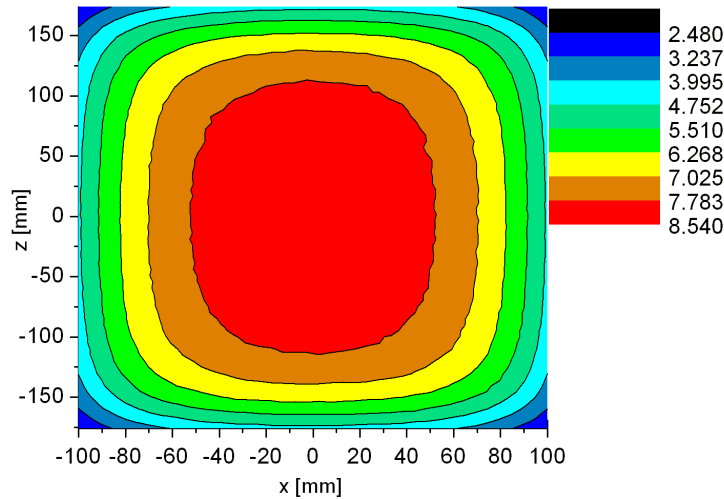


Figure 4.15: Contour plot of the neutron intensity on the detector surface due to a unit uniform plane source of area 200×352 mm². The intensity is in m⁻².

detector surface has the symmetric 2D distribution shown by the contour plot in figure 4.15. As said previously two simulations have been performed:

- First of all, the steel tank was modelled by adding a 50 mm thick iron cylinder of 4 m diameter and 7 m long. The effect was found to be totally negligible. This result would also apply to the bunker walls and any equipment inside the tank that is outside the beam dump area:

they are too far away to give a sizeable contribution to the neutron accounting at the detection surface in the energy range $E_n > 0.2$ MeV. This would not be the case if the detector were not in close contact with the neutron source.

- The beam support structure is sufficiently close to scatter neutrons towards the detector surface. The items closest to the detectors are the steel columns and the water pipelets letting water in and out of the hypervapotrons. Other items in the beam dump support are further away from the detectors and contribute less to the background. Within the scope of the conceptual study the effect of neutron scattering from the dump support was investigated by adding an iron column to the MCNPX model, as shown by the grey block in Figure 4.11. The column is 1 m long and its cross section in the XY plane is a 20×20 mm² square.

The comparison between neutron intensities with (black lines) and without (red lines) the iron column are reported in Figure 4.16 and Figure 4.17. As expected the neutrons scattered from the iron column increase the neu-

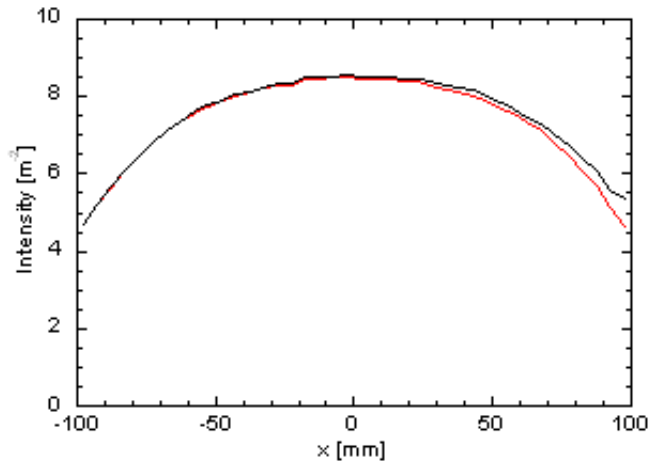
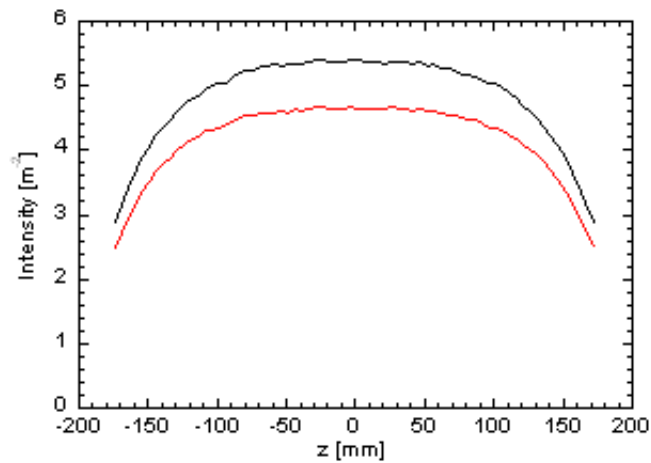


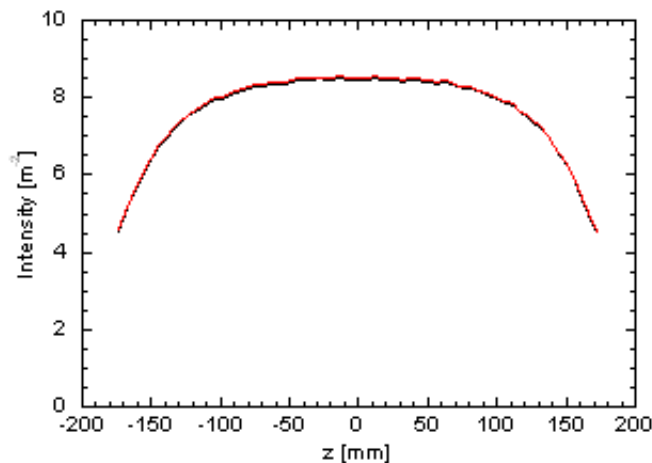
Figure 4.16: Neutron intensity profile along the x direction for $z=0$. The red line is taken from the data of Figure 4.15. The black line shows the effect of neutron scattering from the iron column added to the MCNPX model.

tron intensity in the proximity of the column. This can be seen in Figure 4.16

where the intensity profile along the horizontal direction shows an increase due to the column on the right hand side that vanishes moving away from the column. Scattering from the column contributes an additional $\approx 15\%$ of intensity near the column. This is shown in Figure 4.17(a) where the relative intensity increase is seen to be more or less uniform along the vertical direction at the boundary of the detector surface ($x=100$ mm). On the other hand the intensity does not change for $x=0$ (Figure 4.17(b)). We can sum-



(a)



(b)

Figure 4.17: Same as Figure 4.16 but for the z direction and $x=100$ mm (a), and $x=0$ mm (b).

marise the results of these simulations by stating that a $\approx 15\%$ increase in the neutron intensity should be expected within a distance of ≈ 50 mm from the beam dump support structures.

4.3.5 NEUTRON SPECTRUM

The neutron intensities calculated so far include all neutrons with energy above 0.2 MeV. Since the response of neutron detectors is energy dependent the role of neutron scattering will depend also on the energy spectrum of the scattered neutrons. Neutron energy spectra recorded at three different locations on the detector equatorial plane ($z=0$ mm) are shown in Figure 4.18 for the model case with iron support column. The red line is the reference

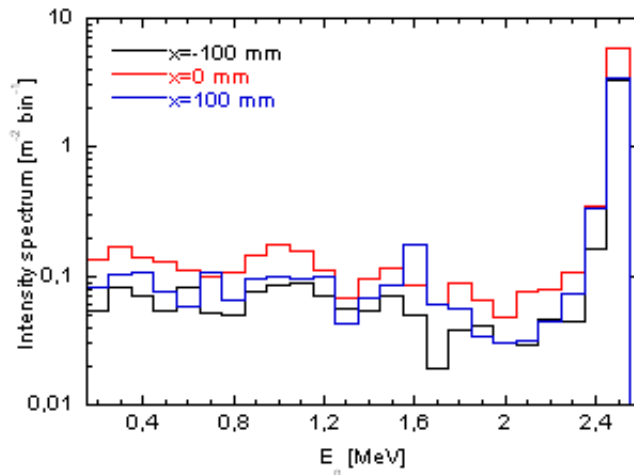


Figure 4.18: Neutron energy spectrum at three positions on the detector surface with $z=0$ and $x=-100$ mm (black), 0 mm (red) and 100 mm (blue).

spectrum at the detector centre. At this point the scattering from the iron column is negligible and all scattered neutrons come from the beam dump. Most of the scattered neutrons show up in the spectrum as a low energy tail whereas unscattered neutrons have the full 2.45 MeV energy and fall in one bin on the right hand side. The scattered neutron spectrum has a fine structure with broad peaks due to the presence of scattering resonances in the n-Cu scattering Cross Section. Indeed the same structure (with statisti-

cal fluctuations) is visible also in the spectrum at $x=-100$ mm (black) albeit with lower intensity. At $x=-100$ mm the neutron intensity is about half the value at $x=0$ mm for reasons of detection geometry. At $x=100$ mm (blue) the spectrum is the same as at $x=-100$ mm except for the additional scattering contribution from the iron column: there is no change in the rightmost bin at full energy, whereas the scattered neutron spectrum now reflects the scattering resonances of iron on top of the copper ones.

The fractional intensity of the scattered neutrons is about 30% at the positions $x=-100$ mm and $x=0$ mm; i.e. 30% of the total neutrons are scattered from the beam dump before reaching the detection surface. At $x=100$ mm the scattered fraction is higher (37%). These numbers would seem in contradiction with the previous observation (Figure 4.14) that the peak intensity from a point source was hardly affected by the presence of the beam dump. The reason why both results are correct can be explained as follows. When the source is close to the detector (case of Figure 4.14) most of the scattered neutrons have a much longer path before reaching the detection point and the relative contribution of scattered neutrons to the total is low. When the source is instead far from the detector the relative contribution of scattered neutrons is larger. The 30% value is an indication that a large fraction of the neutron intensity is due to contributions from distant parts of the source; this is further addressed in the next paragraph.

Experimentally the contribution of scattered neutrons is decreased by detecting neutrons above an energy threshold. For the purpose of illustration we report in Table 4.1 the relative fraction of scattered neutrons of Figure 4.18 that have an energy exceeding a threshold $E_{th}=2$ MeV. Note that the

x [mm]	Scattered fraction, $E_{th} = 0.2$ MeV	Scattered fraction $E_{th} = 2$ MeV
-100	30.3 %	8.0 %
0	31.6 %	9.3 %
100	37.3 %	12.4 %

Table 4.1: Relative contribution of scattered neutrons to the total intensity at different detection positions and for detection thresholds.

total intensity above threshold is different for the two columns in the table. The scattering contribution above 2 MeV is at the 10% level. This can be further reduced as explained in the next chapter by using a detector that can discriminate neutrons depending on their angle.

4.3.6 CONTRIBUTION OF A SINGLE BEAMLET

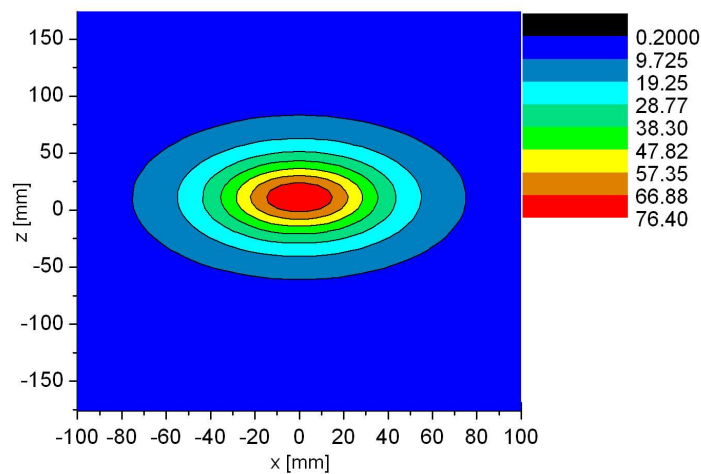
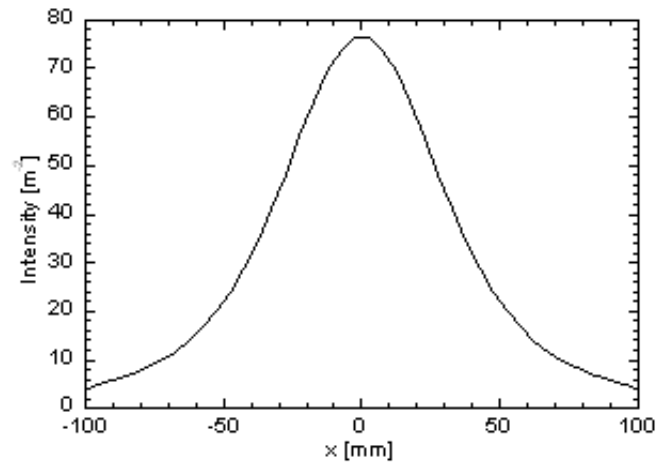


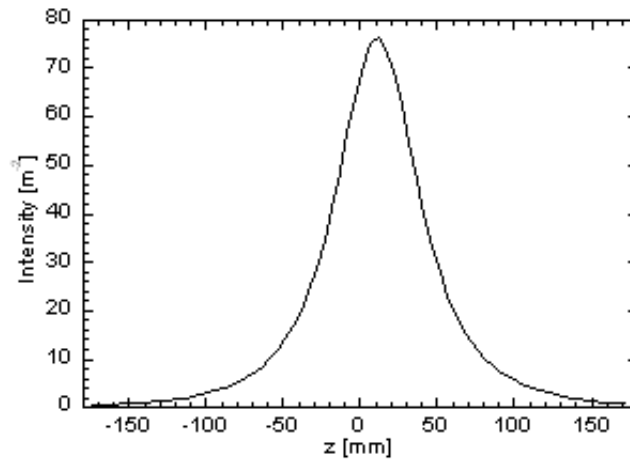
Figure 4.19: Contour plot of the neutron intensity on the detector surface due to a unit uniform plane source of area $40 \times 22 \text{ mm}^2$ centred at the coordinate origin. The intensity is in m^{-2} .

We have seen in this chapter that a point source gives an intensity distribution that is peaked at a well-defined position on the detector surface. We have also seen earlier (chapter 1) that the SPIDER neutron source is an array of individual sources at beamlet footprints. Each source has an elliptical cross section and a Gaussian profile but here we make the simplifying assumption that it is a $40 \times 22 \text{ mm}^2$ rectangle of uniform emissivity. The intensity distribution on the detector surface from a $40 \times 22 \text{ mm}^2$ rectangular unit source is shown in Figure 4.19. Intensity profiles along the x and z directions are shown in Figure 4.20. The profiles are not very different from those shown in Figure 4.14 for a pointwise source except for a greater FWHM ($\approx 5\%$ increase), and for a lower peak intensity ($\approx 10\%$).

The contour obtained in Figure 4.15 is the superposition of a matrix of 5x16 distributions from individual rectangular/elliptical beamlets (Figure 4.19). If we compare the normalized intensities (considering the area of the respective sources) of the profiles shown in Figures 4.20(a) and 4.16 (red line) we obtain the graph reported in Figure 4.21. The graph tells us that $\approx 10\%$ of the intensity is due to the beamlet facing the detection point. The remaining 90% is due to the integrated intensity from the other 79 beamlets. This result is the starting point for further considerations on the spatial resolution of the



(a)



(b)

Figure 4.20: Neutron intensity profile along the x direction for $z=0$ (a) and along the z direction for $x=0$ (b). Data from Figure 4.19.

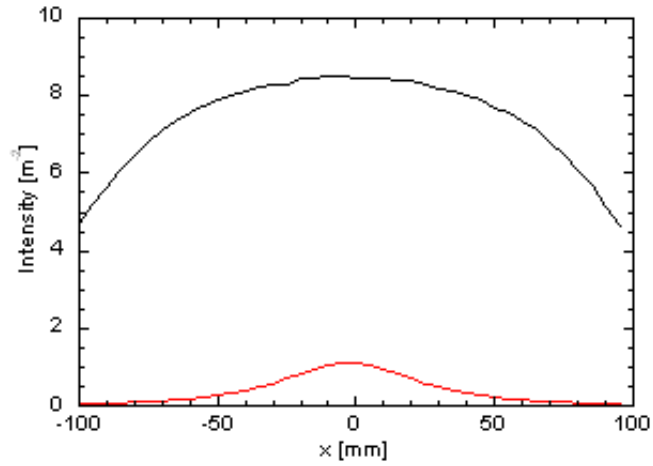


Figure 4.21: Neutron intensity on the detector surface due to a unit uniform plane source of area $40 \times 22 \text{ mm}^2$ centred at the coordinate origin. The intensity is in m^{-2} .

neutron measurements. In the next chapter a detector able to discriminate neutrons respect to their incidence angle will be described. This will lead to a significant improvement of the spatial resolution of the measurement.

Chapter 5

The CNESM detection system

One of the diagnostic system which are going to be installed on SPIDER is the Close-contact Neutron Emission Surface Mapping (CNESM). It is based on the use of nGEM detectors that can measure the neutron emission map from the SPIDER beam dump with a spatial resolution approaching the size of an individual beamlet. nGEM can be complemented by other detectors including the FDD. The detector development for CNESM is presented in this chapter.

5.1 FISSION DIAMOND DETECTORS FOR SPIDER

Diamond, as mentioned before, is a suitable detector material for neutron detection in highly radioactive environments. Its radiation hardness, low voltage and room temperature operation make it a practical material for use in a neutron environment. Unfortunately its inelastic neutron cross section vanishes below 6 MeV which has so far limited its application in fusion research to the detection of 14 MeV neutrons from the DT reaction. However, the test performed at ISIS neutron source of a Fission Diamond Detector (FDD) and described in chapter 2 and Paper III demonstrate that the use of a diamond detector coupled to a uranium foil makes possible the detection of neutrons also from the DD reaction: the t_{ToF} spectrum obtained for measurements performed was shown in Figure 2.17.

In order to understand the spectrum in more detail a model calculation can be made. The Reaction Rate Density (RRD) can be expressed [46] as the product between the fission cross section, $\sigma(E)$, and the neutron flux, $\phi(E)$. Multiplying the RRD for the Jacobian of the transformation between neutron energy and t_{ToF} we can calculate the RRD as a function of the ToF for a single proton bunch. This is reported in Figure 5.1. The red line represent

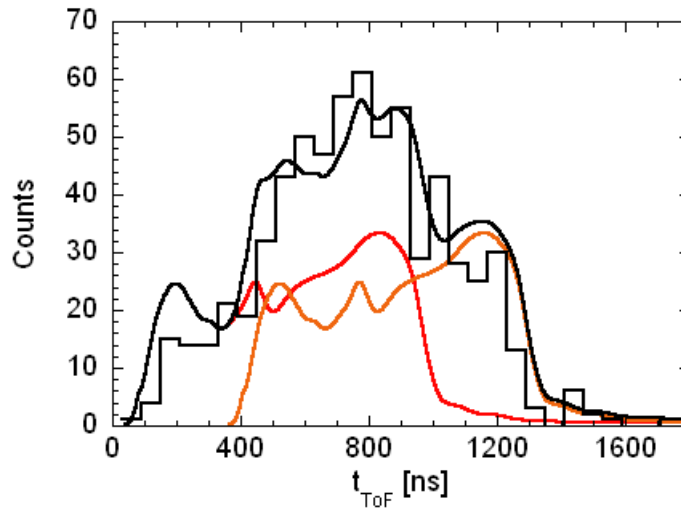


Figure 5.1: ToF Spectrum obtained considering only fission events from ^{238}U , compared to simulation results.

the RRD for the first bunch, the orange line for the second bunch. Both lines have been convoluted with a 70 ns wide gaussian, in order to simulate the bunch width. The black line represent the sum between the two lines. The agreement between data and simulation is rather good and confirms the identification of the selected events with ^{238}U fission events. The results of the test confirm that the FDD is detecting neutrons using the same fission process typical of other common neutron detectors, such as Fission Chambers. What is unique of the FDD is its small size which makes it suitable for neutron flux measurements behind the SPIDER beam dump with a spatial resolution of < 10 mm. The detector can be operated in vacuum and fixed directly to the back of the beam dump. Rates of the order of > 100 Hz are expected which is sufficient to provide data with 10 s time resolution. Thus

we envisage that implementation of a few of these detectors would not be impractical. On the other hand the use of a large number of FDDs would be cumbersome and expensive. Therefore FDDs will not be used as the standard detector for mapping the neutron emission from the SPIDER beam dump. The FDD could instead be used as an independent monitor of the neutron flux at a few locations behind the dump. The precise location for FDDs use should be defined as part of the engineering design taking into account the access constraints of the alternative detectors presented in the next section. E.g. FDDs may fit in restricted spaces where no other detector would.

5.2 NEUTRON DETECTION WITH NGEM: THE DIAGNOSTIC SYSTEM

The key component of the CNESM diagnostic system is the nGEM detector. This is a Gas Electron Multiplier (GEM) detector equipped with a cathode that also serves as neutron-proton converter foil. In this section the key parameters of the nGEM detector will be discussed: from the GEM operating principle to the electronic chain to neutron detection using the nGEM.

5.2.1 GAS ELECTRON MULTIPLIER DETECTORS

The GEM, proposed in the 1997 by F. Sauli [47], was born as an *upgrade* of the MWPC (Multi Wire Proportional Chamber, [48]) for its ability to cope with high intensity fluxes. Overcoming the flux limitation of the MWPC is particularly needed in the new high luminosity colliders and nowadays the GEM technology is well established, and it has essential tasks in several high energy physics experiments including LHCb.

In the GEM detector the conversion, multiplication and the induction regions are physically distinct, resulting in a greater freedom in the readout geometry. Moreover, the possibility to divide the multiplication in more steps drastically reduces the problems of discharge and ageing processes.

The GEM is a 50 μm thick insulating kapton foil, clad on each side with a

thin copper layer ($5\mu\text{m}$) and chemically perforated with a high density matrix of holes. The holes have a bi-conical structure with an external diameter of $70\mu\text{m}$ and internal of $50\mu\text{m}$ and a pitch of $140\mu\text{m}$ [49] (Figure 5.2). In a GEM detector the hole acts as a multiplication channel for the electrons released by ionizing radiation in the gas mixture. Applying a suitable voltage difference ($300\div 500\text{ V}$) between the two copper faces, a high electric field ($<100\text{ kV/cm}$) is generated inside the holes. In this region, an electron can acquire enough energy to develop an avalanche. The reachable gain with a single GEM can be greater than 10^3 . The choice of the geometrical parameters of a GEM foil, as the hole diameter, the pitch and the hole shape, and the manufacturing technique are a compromise between production yield and safe operation of the detector [50].

5.2.2 SINGLE AND TRIPLE GEM

The simplest gas detector based on GEM technology is obtained by inserting a single GEM foil between two flat parallel electrodes [51]. The upper electrode plays the role of cathode while the lower one is the readout anode. The cross section schematics of a single-GEM detector is shown in Figure 5.3(a), together with the labelling of the different detector parameters. The drift field, E_D , is generated between the upper side of the GEM foil and the cathode, while the induction field, E_I , between the lower side of the GEM

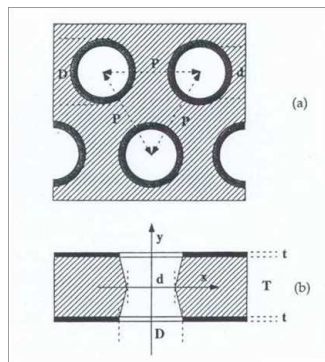
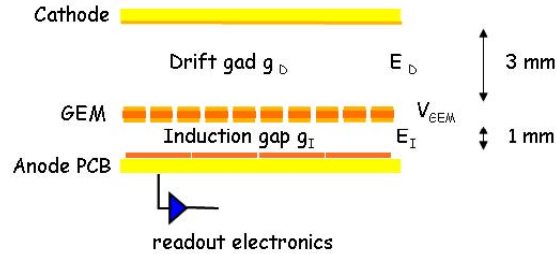
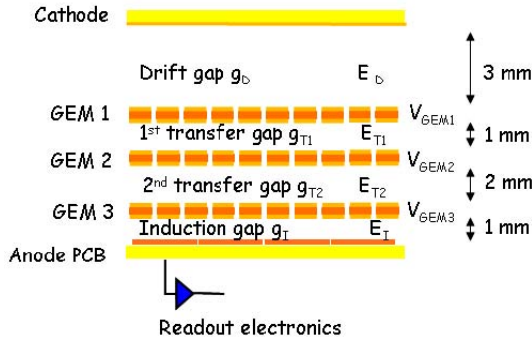


Figure 5.2: Cross section of the geometry of GEM foil and the bi-conical shape of the holes.

foil and the anode (PCB). The relative regions are called drift and induction



(a) E_D and E_I are the drift and the induction fields, while g_D , g_I are the drift and induction gaps; V_{GEM} is the voltage difference applied to the two copper layers of the GEM foil.



(b) E_D , E_{T1} , E_{T2} and E_I are the drift, the first and the second transfer and the induction fields respectively; g_D , g_{T1} , g_{T2} and g_I are the drift, the two transfer and the induction gaps respectively.

Figure 5.3: Cross section of a single (a) and triple (b) GEM detector.

gaps. Electrons produced by ionization in the drift gap are driven by means of the low E_D towards the GEM holes, where multiplication occurs. Some of the electrons from the multiplication are collected on the lower side of the GEM foil. The fraction of the multiplication electrons that are transferred in the induction gap, gives rise to an induced current signal on the anode. Typically, such a fraction is 50% and it depends on the electric field inside the hole and below the GEM. The multiplication ions are mainly collected on the upper side of the GEM foil instead of drifting towards the cathode, leaving the GEM hole free from charges in a relatively short time (few μs), thus ensuring this kind of detector a high rate capability.

As mentioned above, the induced signal is purely due to the motion of the electrons in the induction gap. Taking into account the high electron mobility, the induced signal is fast and not affected by the ion tail typical of wire chambers. Higher gas gain, up to $10^4 - 10^5$, can be achieved assembling more than one GEM foil in cascade at close distance to each other. A triple-GEM detector consists of three GEM foils piled-up and sandwiched between the two electrodes, and the gain is divided in three amplification stages each with a lower electric field. A cross section of a triple-GEM detector, together with the labeling defining the geometrical and electrical parameters, is shown in Figure 5.3(b). The voltage difference applied to the various GEM foils are called (from top to bottom) V_{GEM1} , V_{GEM2} , V_{GEM3} , and their sum V_{tot} . The gap between the cathode and the first GEM foil acts as conversion and drift gap. The gap between the last GEM foil and the anode is the induction gap where (after multiplication, in this case due to the three GEM foils) the charge induces the signal on the anode PCB. The other two gaps, between two consecutive GEM foils, are called transfer gaps. They act as an induction gap for the above GEM, while as a drift gap for the GEM below.

For a triple-GEM detector the intrinsic gain is an exponential function of V_{GEM} . It is found that the effective gain depends on the voltage applied to the three GEMs only through their sum. Thus it is possible to unbalance these voltage differences in order to reduce the discharge effect in the last GEM.

The time performance of a GEM-based detector depends on the signal fluctuations during the pulse rise. These are correlated with the statistics of the clusters produced in the drift gap. It was estimated that the Ar/CO₂ (70/30) gas mixture, commonly used by other experiments, give a time resolution of about 10 ns r.m.s [52] for a typical applied voltage of $V_{GEM}=4$ kV. This will be the gas mixture that will be used on SPIDER.

5.2.3 HIGH VOLTAGE AND READOUT SIGNAL

The GEM detector at LHCb has a specialized front-end electronics suitable for operation under tight space constraints and radiation hardness. A

custom high voltage system is also available that ensures flexibility and safe-operation.

The high voltage is generated by the HV-GEM power supply [53] and is brought to the detector through a multi-pin (8 pins) cable. A compact panel, containing RC filters used to filter HV noise, links the pins of the HV cable to the 7 HV pads that are present on the drift cathode PCB and brings the voltages to the detector electrodes whose terminals are connected to it.



Figure 5.4: Readout board with 8 CARIOCA chips.

For what concerns the front end electronics, ten CARIOCA (Figure 5.4) chips will be used to read out the pad signals. This type of chip has already been used for the LHCb GEM detectors at CERN [54]. CARIOCA is an Amplifier-Shaper-Baseline-Restorer-Discriminator Front-end Chip fabricated with IBM 0.25 μm CMOS technology. More details on CARIOCA chips can be found in [55].

5.2.4 THE NEUTRON DETECTION PRINCIPLE WITH GEMs

As already mentioned the nGEM detector is a GEM detector with a cathode that also serves as neutron-proton (n-p) converter foil, where neutrons coming from the beam dump are converted into protons by elastic recoil. A 50 μm CH_2 will be used as converting material, an Aluminium foil will be used as cathode. A proton which leaves the polyethylene foil with enough energy can cross the aluminium layer and ionize the gas. The energy of the proton, E_p ,

is higher if its recoiling angle, θ_{n-p} , is smaller:

$$E_p = E_n \cdot \cos^2 \theta_{n-p} \quad (5.1)$$

As said in section 4.3, it is clear that if the neutron emission map must be representative of the deuterium beam uniformity, the signal read on a nGEM pad must be due to neutrons emitted from the corresponding $40 \times 22 \text{ mm}^2$ beamlet footprint on the dump front surface. This is only possible if we can select neutrons impinging the cathode surface with an incident angle smaller than $40\text{-}50^\circ$. Figure 5.5 illustrates how this is achieved by suitable choice

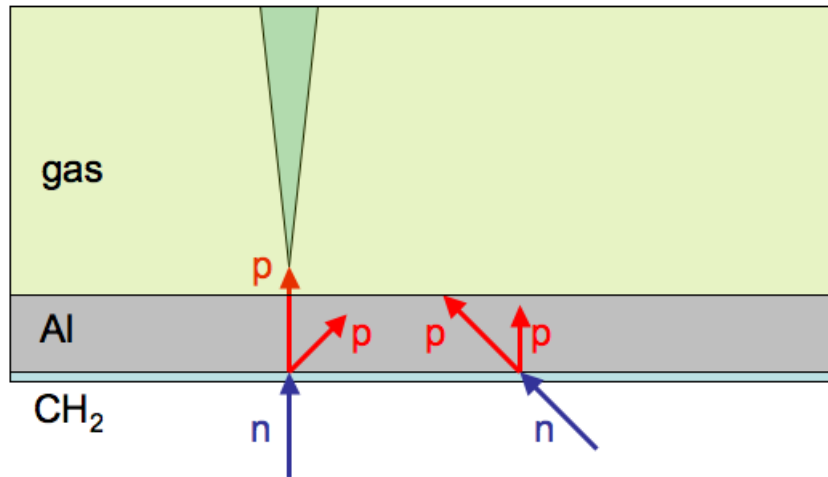


Figure 5.5: A thick Al cathode (grey) is used to suppress detection of neutrons with oblique incidence. Only one of the four protons in the figure can cross the Al layer and produce a discharge in the GEM gas.

of the Al foil thickness by considering two neutrons of energy $E_n=2.5 \text{ MeV}$ hitting the active GEM surface with incidence angles of $\theta = 0^\circ$ and $\theta = 45^\circ$. For a quasi-normally incident neutron ($\theta_n = 0^\circ$), the recoiling protons, have energies ranging from 2.5 MeV ($\theta_{n-p} = 0^\circ$) and 1.77 MeV ($\theta_{n-p} = 45^\circ$). Only the first proton has energy enough to cross the $50 \text{ }\mu\text{m}$ -Al layer and reach the gas (the range of a 2.5 MeV in Al is $60 \text{ }\mu\text{m}$). The net result is that protons emitted at 45° do not reach the GEM gas because they lose all their energy

in the Al layer. Consider now the neutron impinging the nGEM cathode with $\theta_n = 45^\circ$. The most energetic recoiled protons have 2.5 MeV but they have to cross 70 μm of alluminum: they have a longer path respect to those emitted with $\theta_{n-p} = 45^\circ$. On the other hand these protons have not enough energy (1.77 MeV) to cross the 50 μm Al foil.

This simple analysis shows that the detection of neutrons hitting the nGEM with a large incidence angle can be suppressed using an opportune Al-foil thickness. The reference case described here is just for illustrating of the concept, in the next section the results of simulations performed with different Al thickness and incoming neutron angle will be discussed.

5.3 SIMULATION OF THE nGEM CATHODE

The simulations were performed with the MCNPX code. A monoenergetic ($E_n=2.7$ MeV) point neutron source was placed at a distance $d=30$ mm from the nGEM cathode. The cathode is modelled as a slab composed of a 25 μm thick polyethylene foil (CH_2), a $t=43$ μm thick Al foil and a 3 mm GEM gas mixture of Argon (70%) and CO_2 (30%). A scheme of the geometry of the cathode implemented in MCNPX is reported in Figure 5.6, the z direction is the direction of neutron motion. Neutrons in the n-p converter produce



Figure 5.6: A thick Al cathode (grey) is used to suppress detection of neutrons with oblique incidence. Only one of the four protons in the figure can cross the Al layer and produce a discharge in the GEM gas.

protons. The energy deposited by protons in the gas was studied using the MCNPX-F8 tally. This tally produces as output a histogram of the energy deposited by the proton in the GEM gas.

5.3.1 ENERGY DEPOSITED IN THE nGEM GAS

In Figure 5.7 the energy deposited, E_d , in the nGEM gas is reported for different Al thicknesses and considering a neutron incident angle equal to 0° . In Figure 5.8 and 5.9 E_d is reported for different neutron incident angles θ_n , for an aluminum thickness of $43 \mu\text{m}$ and $51 \mu\text{m}$ respectively. The distribution of

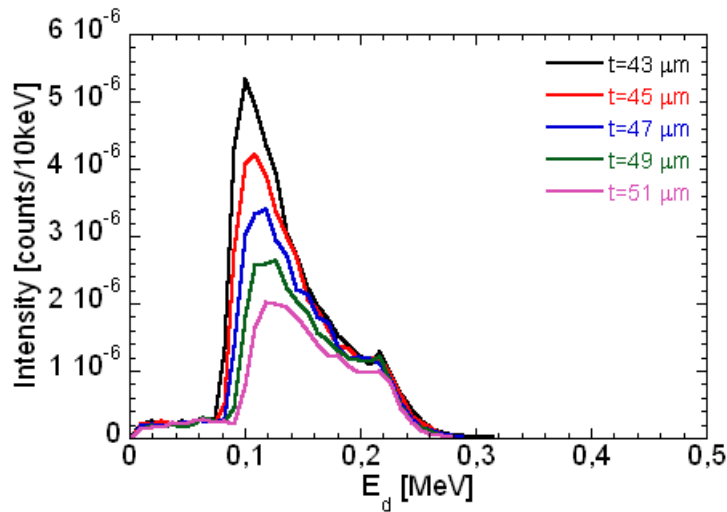


Figure 5.7: Simulated distribution of proton energy deposition inside the nGEM gas for different Al thicknesses. The neutron incident angle is set at $\theta_n = 0^\circ$.

deposited energy rises sharply above $E_d=70-90 \text{ keV}$ and drops above $E_d=240 \text{ keV}$. The detailed shape of the distribution within this energy range can be understood by noting that:

- the energy loss dE/dz is a decreasing function of the proton energy,
- the range of the most energetic protons is longer than the GEM gas thickness.

The result is that higher energy protons deposit less energy in the gas, whereas the maximum deposited energy is achieved by lower energy protons that have a range matching the GEM gas thickness. We can therefore interpret the spectral shape as due to two main components:

- On the low energy side is a strong peak due to energetic protons.
- The second component due to lower energy protons peaks on the high energy side of the distribution.

If we observe Figure 5.7 we note that the second spectral component does not vary significantly with the Al-thickness, whereas the first component is much more dependent on the Al thickness. In fact, increasing the Al foil thickness the energy of protons reaching the gas is overall decreased.

In Figures 5.8 and 5.9, the first component is seen to be dominant for lower neutron incidence angles. As θ_n is increased, the second component does not vary significantly. For an Al thickness of 51 μm the overall signal drops to almost 0 for $\theta_n > 45^\circ$ which is the directional response we wanted to achieve.

nGEM integral detector response

The nGEM detector readout electronics includes a lower energy discriminator that can be set anywhere in the range of deposited energies. We consider

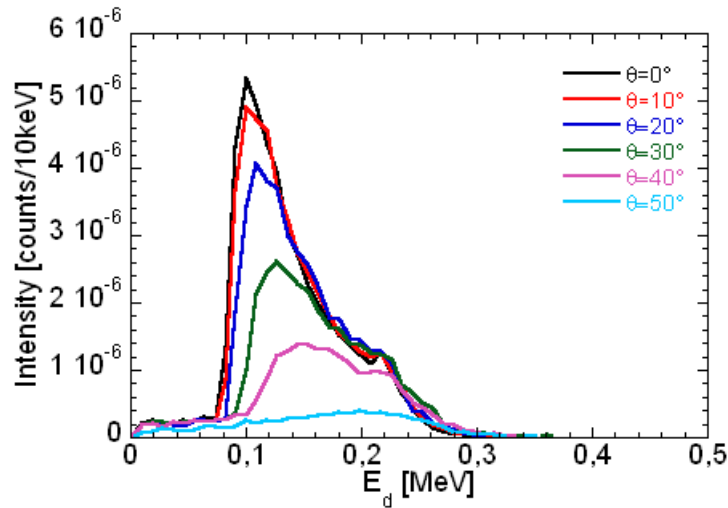


Figure 5.8: Simulated distribution of proton energy deposition inside the nGEM gas for different neutron incident angles θ_n . The thickness of the Al foil was $t=43 \mu\text{m}$.

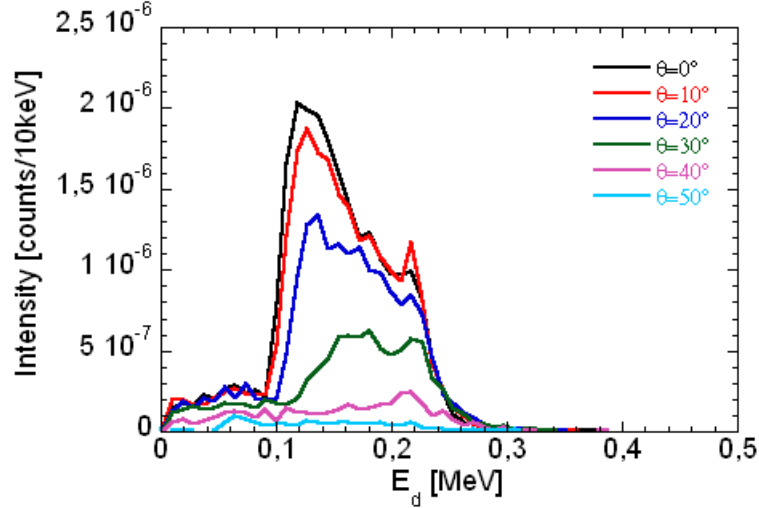


Figure 5.9: Simulated distribution of proton energy deposition inside the nGEM gas for different neutron incident angles θ_n . The thickness of the Al foil was $t=51 \mu\text{m}$.

two threshold values: the first one at $E_{dth}=70 \text{ keV}$, just below the peak due to the most energetic protons, and a second one at $E_{dth}=200 \text{ keV}$, more sensitive to events due to the less energetic protons. Now we consider the total number of events above threshold. This is shown in figure 5.10 with an energy threshold $E_{dth}=72 \text{ keV}$ (a) and $E_{dth}=200 \text{ keV}$ (b). These plots show the directionality of the nGEM response to neutrons: the integrated number of events is a decreasing function both of the angle and of the thickness. If we consider the plot with an energy threshold of 200 keV (Figure 5.10(b)) we see that with an Al foil of $43 \mu\text{m}$ the efficiency at 30° is higher than the efficiency at 0° . This can be understood by observing figures 5.8 and 5.9: for small Al thicknesses and small incident angles, the contribution due to more energetic protons (those depositing less energy in the gas) is higher than the contribution due to less energetic protons (depositing more energy). Therefore, by increasing the angle, we are increasing the path of protons in Al and then decreasing their energy. This is the reason why at $43\text{-}45\text{-}47 \mu\text{m}$ the detector efficiency above 200 keV is higher at 30° than at 0° .

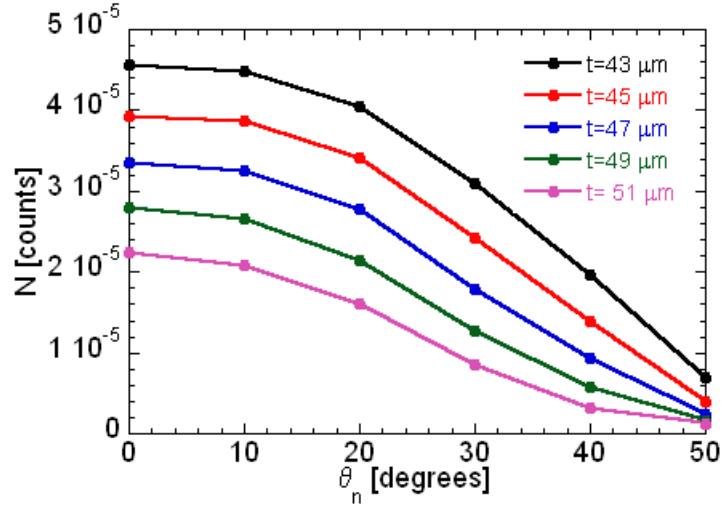
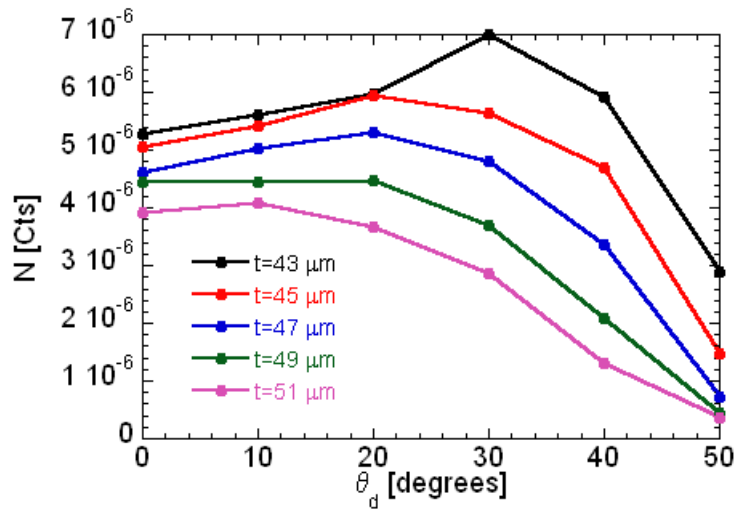
(a) $E_{dth}=72$ keV(b) $E_{dth}=200$ keV

Figure 5.10: Integrated number of events with proton energy deposition above threshold inside the nGEM gas for different neutron incident angles θ_n and different Al thicknesses t .

A good figure of merit is the ratio $\rho = N(\theta_n = 0^\circ)/N(\theta_n = 40^\circ)$ between the number of events above threshold at $\theta_n = 40^\circ$ and $\theta_n = 0^\circ$. For $E_{dth}=70$ keV this ratio (Figure 5.11 dash-line) becomes smaller as the Al thickness is increased. This means that a thicker Al layer is better for achieving a

low sensitivity of the nGEM to neutrons with large incidence angles. For $E_{dth}=200$ keV good rejection of large incidence angles is achieved only at the highest Al thickness value considered. A safe choice is therefore to use an Al thickness of about $50 \mu\text{m}$, providing good results independently of the choice of E_{dth} (which could be dictated by other instrumental reasons, e.g. background rejection). A larger thickness would provide somewhat better directionality but would come at the price of a lower efficiency. An Al thickness of about $50 \mu\text{m}$ is therefore a good compromise between directionality and efficiency of the detector.

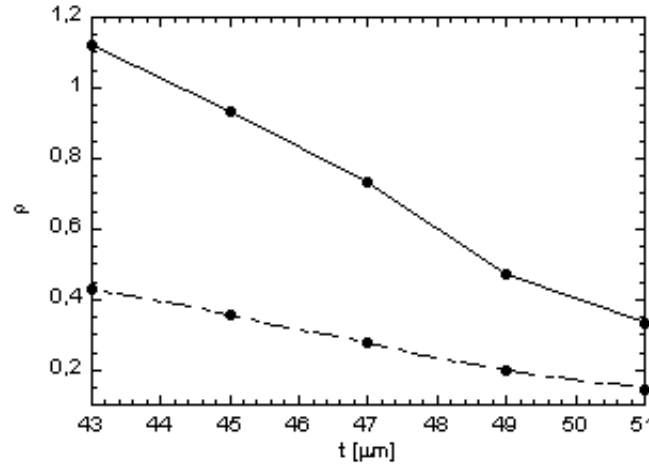


Figure 5.11: Ratio $\rho = N(\theta_n = 0^\circ)/N(\theta_n = 40^\circ)$ between the number of events above threshold at $\theta_n = 40^\circ$ and $\theta_n = 0^\circ$, plotted as a function of Al thickness t . The threshold is $E_{dth}=72$ keV (dash line) and $E_{dth}=200$ keV (full line).

5.3.2 nGEM DETECTOR SPATIAL RESOLUTION

The angular response shown in Figure 5.10(a) can be used to determine the effective spatial resolution of the nGEM. This is shown in Figure 5.12 where the simulated nGEM response to neutrons emitted along the x-position at a distance $d=30$ mm from the nGEM is plotted for the two cases with and without the Al foil. Without the Al foil the response follows the $1/(d^2+x^2)$ law and drops slowly as the neutron point source is moved away from the

$x=0$ position, as shown with the red line in figure 4.13. The case with a $49\ \mu\text{m}$ thick Al foil features a sharper decay and drops to zero for $x\approx 50$ mm. The curves of Figure 5.12 can be integrated to give the integral detector re-

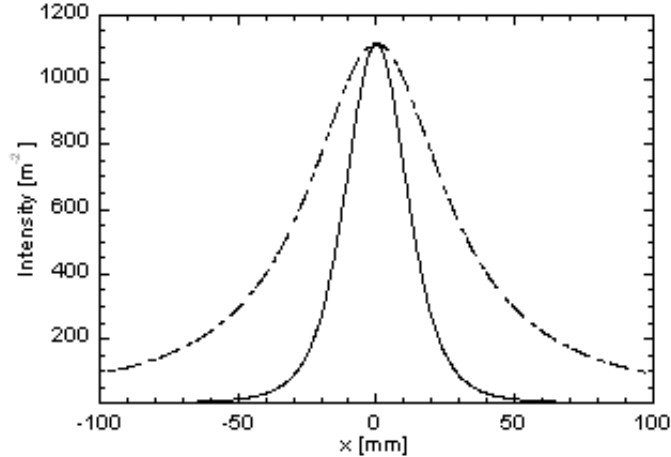


Figure 5.12: Simulated nGEM response to neutrons emitted along the x -position at a distance $d=30$ mm from the nGEM. The nGEM response is much sharper when the cathode is equipped with a $49\ \mu\text{m}$ Al foil (continuous line) than without the Al foil (dashed line).

sponse shown in Figure 5.13 for the cases with (continuous line) and without (dashed) a $49\ \mu\text{m}$ Al foil. The neutron emission is assumed to be uniform and isotropic on a surface placed at $d=30$ mm from the nGEM. The quantity plotted is the relative number of recorded events due to neutrons emitted from within a circle of radius x . Both curves are normalised so they equal unity at $x=100$ mm. Without the Al foil the number of recorded events due to neutrons emitted within $x=30$ mm would be as low as $\approx 30\%$; i.e. over two thirds of the neutrons detected at the $x=0$ position would in fact come from $|x|$ values > 30 mm. With the Al foil the situation is reversed and $\approx 80\%$ of the events recorded at $x=0$ are due to neutrons emitted within $|x| < 30$ mm. We conclude that the simulations show a significant improvement in spatial resolution due to the use of a $\approx 50\ \mu\text{m}$ Al foil on the nGEM cathode. This approach was used in the first nGEM prototype tested at the FNG neutron source, which is the subject of the next section.

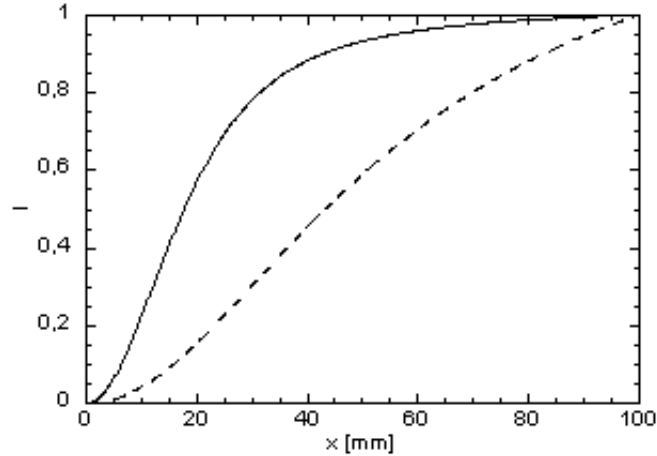


Figure 5.13: Integral detector response for the cases with (continuous line) and without (dashed) a $49 \mu\text{m}$ Al foil. The neutron emission is assumed to be uniform on a surface placed at $d=30$ mm from the nGEM. The quantity plotted is the relative number of recorded events due to neutrons emitted from within a circle of radius x .

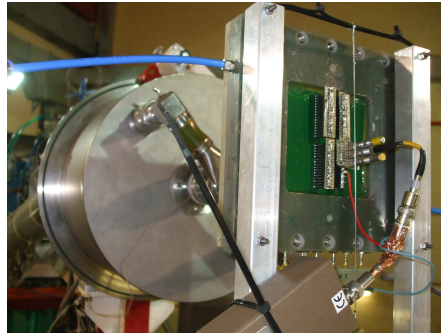
5.4 EXPERIMENTS WITH THE FIRST NGEM PROTOTYPE

5.4.1 EXPERIMENTAL SET UP

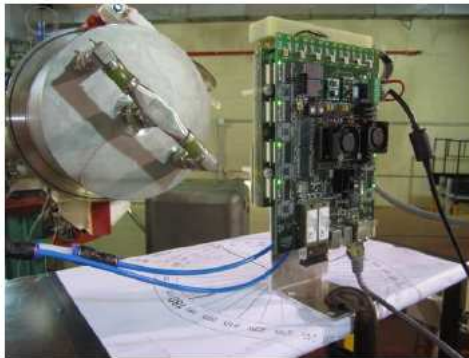
Two small area ($10 \times 10 \text{ cm}^2$) nGEM prototypes have been realized and tested using 2.5 MeV neutrons at the FNG (Frascati Neutron Generator) [56] located in Frascati (see Figure 5.14(a) and (b)). These are triple GEM detectors equipped with the CH_2 ($60 \mu\text{m}$) + Al ($40 \mu\text{m}$) converter cathode. The gaps geometry of these detectors is the same as the one used in Triple GEM LHCb detectors [57]¹. Both detectors were operated using a gas mixture of Ar/ CO_2 / CF_4 (45%/15%/40%). The high voltage configuration was generated using the HV-GEM NIM module and the bias was applied to each electrode by means of passive resistive-capacitive filters properly designed for a Triple GEM detector. The first prototype (hereby called *analog* prototype)

¹(Drift/Transfer 1/Transfer 2/Induction= $3 \text{ mm}/1 \text{ mm}/2 \text{ mm}/1 \text{ mm}$)

has 128 readout pads but just one of these pads is read out using a standard pre-amplifier (Ortec 142 IH), amplifier (Ortec 474), MCA (Ortec Maestro32) chain and MCA outputs pulse height spectra. The second one (hereby called *digital* prototype) has all the 128 pads read out by 16 CARIOCA chips and is able to measure the counting rate of the detector. All the CARIOCAs are then connected to a custom made FPGA Mother Board that analyzes the signals coming from the chips. The digital prototype is a complete small version of the full size area nGEM for SPIDER.



(a)



(b)

Figure 5.14: Analog (a) and digital (b) nGEM prototypes, installed at the FNG 2.5 MeV neutron source.

5.4.2 FIRST PROTOTYPE RESULTS

nGEM linearity with neutron flux

The first test performed was realized using the *digital* nGEM prototype. The results are shown in Figure 5.15. This represent the nGEM counts as a function of the incoming neutron flux, measured by a NE213 beam monitor. As expected the nGEM count rate scales linearly with the neutron flux.

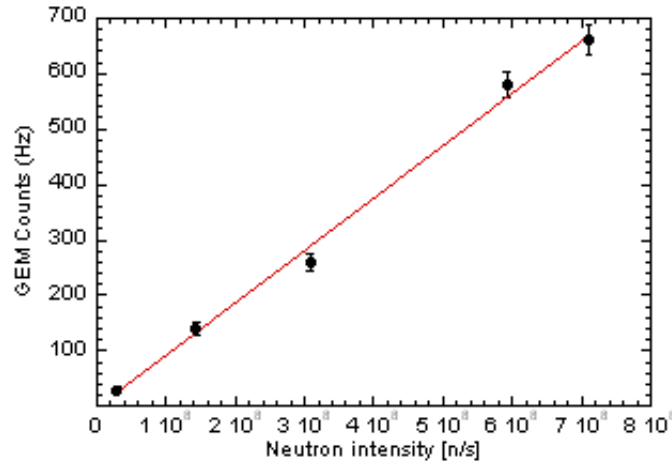


Figure 5.15: nGEM response as a function of the neutron flux. $\Sigma\Delta V_{GEM}=1020$ V; E_d (Drift Field)= E_{T1} (Transfer 1 Field)= $E_{T2}=3$ kV/cm, E_{Ind} (Induction Field)=5 kV/cm; Gas Mixture Ar/CO₂/CF₄ (45%/15%/40%).

This is a crucial result in order to use the nGEM detector as a neutron beam monitor in SPIDER.

5.4.3 DETECTOR DIRECTIONAL RESPONSE

In order to measure the detector directionality the pulse height spectrum is needed, therefore the *analog* detector was used in these measurements. The measurements were performed using these parameters: $\Sigma\Delta V_{GEM}=970$ V; E_d (Drift Field)= E_{T1} (Transfer 1 Field)= $E_{T2}=3$ kV/cm, E_{Ind} (Induction Field)=5 kV/cm; Gas Mixture Ar/CO₂/CF₄ (45%/15%/40%). This parameters result into an effective gain of about 96.

The neutron flux was measured by the NE213 scintillator being equal to about $10^8 \text{n/m}^2 \cdot \text{s}$. The nGEM detector was aligned to the deuterated target and the pulse height spectrum (PHS) was measured by rotating the detector by $\theta_{\text{GEM}} = 10, 20, 30, 45, 60, 90^\circ$ relative to the incoming beam direction. Each pulse height spectrum was normalized to the total flux measured by the beam monitor. The results are shown in Figure 5.16. The rising edge

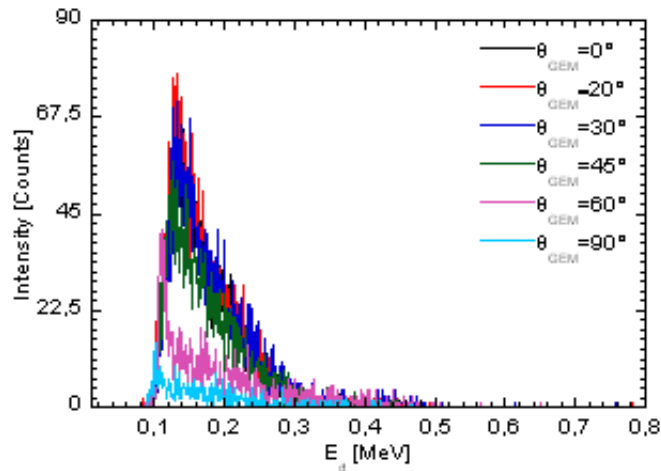


Figure 5.16: Pulse height spectrum measured at the FNG neutron source for different θ_{GEM} values.

on the left of the PHS is affected by the low level discriminator threshold, applied in order to filter the electronic noise. The pulse height spectrum is essentially the same up to $\theta_{\text{GEM}} = 30^\circ$. On the other hand for $\theta_{\text{GEM}} = 45^\circ$ the counting rate decreases, and the signal drops to almost 0 for $\theta_{\text{GEM}} = 90^\circ$. For $\theta_{\text{GEM}} = 90^\circ$ the signal is not exactly zero, but since the nGEM chamber is perpendicular to the incoming neutron beam, we can assume the $\theta_{\text{GEM}} = 90^\circ$ to be mostly background.

In Figure 5.17 the integral above the energy threshold, $E_d = 127 \text{ keV}$, is reported as a function of θ_{GEM} . Here the background measured at 90° was subtracted from all data. As already observed in the previous plot, the detector count rate is almost constant up to 30° , and drops rapidly at larger angles, confirming the directionality of the detector response.

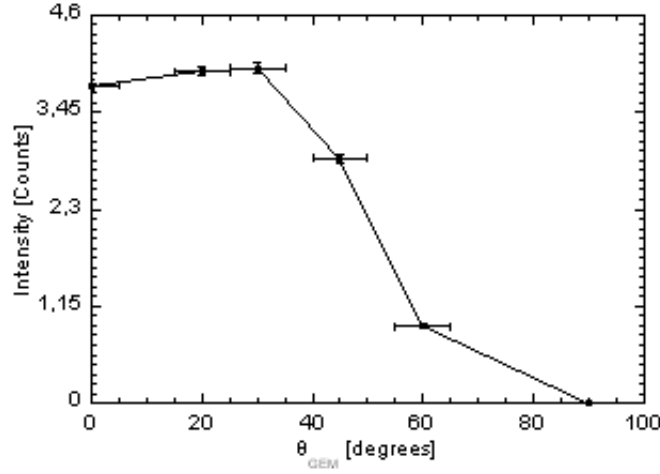


Figure 5.17: Integrated pulse height spectrum above the threshold $E_{dth} = 137\text{keV}$ as function of the θ_{GEM} .

5.5 COMPARISON BETWEEN SIMULATION AND EXPERIMENTAL RESULTS

In this final section the comparison between the experimental results and MCNPX simulations is presented. First of all the experimental and simulated pulse height spectra at 0° are compared in Figure 5.18. The simulations were performed reproducing the experimental conditions but with an Al foil thickness equal to 33 (red line), 38 (blue line) and 43 μm (green line). The simulated spectra have been scaled so as to provide a good match to the data for $E_d > 130$ keV. This is because the measured spectrum is affected by the low energy threshold and data below $E_d = 130$ keV are an artifact. Above the threshold all simulations are in reasonable agreement with the measurement. The area of the PHS above 127 keV is plotted in Figure 5.19 as function of neutron incidence angle. In this figure the area of the PH spectrum was normalized to the area obtained at 0° in order to better show the detector response variation with the neutron incidence angle. The angular response varies significantly with Al thickness: the detector sensitivity to high incident angles (high θ_{GEM}) decreases with increasing Al-thickness. The simulated

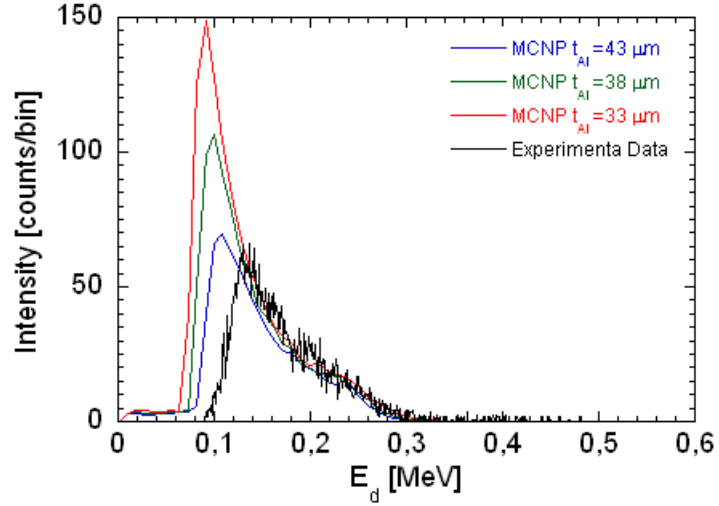


Figure 5.18: Experimental pulse height spectrum (black line) compared to the simulated one. An Al-foil thickness equal to $33 \mu\text{m}$ (red line), $38 \mu\text{m}$ (green line) and $43 \mu\text{m}$ (blue line) was used in simulations. The neutron incidence angle in this case was 0° .

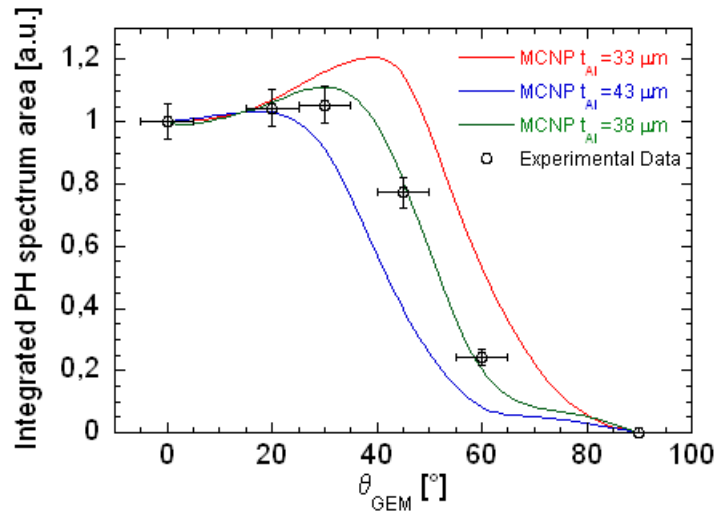


Figure 5.19: Integrated PH spectrum above 127 keV. Experimental data are reported in black, the red line represent the simulated angular response with Al-foil thickness of $33 \mu\text{m}$, the green line $38 \mu\text{m}$ and the blue line considering $43 \mu\text{m}$ of aluminium.

curve providing the best match to the experimental data is the one obtained with an Al thickness of 38 μm . This is consistent with the measured Al-foil thickness of 38 $\mu\text{m} \pm 2 \mu\text{m}$.

The results of the simulations and the good agreement with experimental results confirm the suitability of nGEM detector for measuring the neutron emission map on SPIDER with a spatial resolution approaching the size of an individual beamlet. From the neutron emission map the deuterium beam power profile can be inferred provided the deuterium concentration in the SPIDER beam dump is saturated.

Chapter 6

Conclusions and outlook

The research presented in this thesis was devoted to the development of fast neutron instrumentation for beam diagnostic.

The first part concerns the study of a fast neutron monitor for the ChipIr beamline at ISIS. ChipIr will be dedicated to neutron chip irradiation experiments for measuring the Single Event Effects incidence rate in electronic devices. The detectors proposed here are based on single-crystal diamonds. Two approaches have been attempted: the Single-crystal Diamond Detector (SDD) and the Fission Diamond Detector (FDD).

First SDD tests were performed at ISIS using a thin (150 μm) diamond and Time of Flight (t_{ToF}) data acquisition. The tests demonstrated the SDD potential for development of a small size beam monitor suitable for neutron flux measurements with high spatial resolution. The measured t_{ToF} spectrum was consistent with the double pulse time pattern of the proton beam, thus showing the good time resolution of our detection system. In order to achieve not only the t_{ToF} information but also the pulse height spectrum, i.e. the energy deposited in the diamond, a new data acquisition chain was developed based on a commercial waveform digitizer. Further measurements showed a correlation between the energy deposited in the detector and the neutron t_{ToF} , suggesting that SDDs may be good candidates for fast neutron spectroscopy at spallation sources. A FDD was also tested using the same biparametric data acquisition. The FDD was made of a $^{\text{nat}}\text{U}$ foil as fissile

target coupled to a 24 μm thin SDD. An FDD combines the fast neutron response of carbon to the neutron-induced fission in natural uranium. Biparametric data collection was found to be essential for a correct separation of events from ^{235}U , ^{238}U and from carbon break-up reactions.

The last stage in the SDD development within this thesis project was the use of a more efficient SDD capable of high rate measurements. The high rate SDD is based on a thicker (500 μm) commercial diamond coupled to a fast preamplifier and 1 GHz digitizer. The system was optimized for speed but had nevertheless enough energy resolution to separate events due to different interaction processes in the diamond. Three characteristic regions in the biparametric spectra were observed: i) low pulse height events with very short time of flight induced by γ -rays; ii) low pulse height events at longer flight times (i.e. neutron energies $E_n > 3.5\text{-}6$ MeV), possibly due to neutron elastic scattering off ^{12}C ; iii) events with large pulse height and flight times corresponding to $E_n > 6$ MeV mainly due to inelastic reactions such as $^{12}\text{C}(n, \alpha)^9\text{Be}$ and $^{12}\text{C}(n, n')^3\alpha$. Inelastic processes are the ones for which the use of SDD seems most promising. E.g. a rugged fast neutron counter can be realized by using the present system with a pulse height threshold rejecting events with deposited energy below, say, 10 MeV. For comparison the range of deposited energies explored in this thesis reached about 100 MeV.

No attempt was made in this thesis to use the biparametric data for quantitative spectroscopy. A prerequisite would be an assessment of the SDD response to monoenergetic neutrons and, preferably, an improvement in its energy resolution without sacrificing rate capability. Plans are underway to perform measurements at the n_{TOF} pulsed neutron source at CERN. n_{TOF} is short pulsed meaning that neutrons of high energies can be separated by their time of flight; this is partly prevented at ISIS by the width of the proton pulses (about 70 ns FWHM). By folding the monoenergetic response measurements at n_{TOF} with the proton pulse time structure of ISIS we shall attempt to perform a quantitative analysis of biparametric spectra at ISIS. The lower energy limit in the biparametric analysis is expected to lie close to the threshold of inelastic n-C reactions, e.g. 5-6 MeV. This is adequate for most applications of the ChipIr beamline. Use of diamond detectors for

neutrons of lower energy may be possible using thinner SDD diamonds with lower event rates and a more conventional electronics chain providing better energy resolution. Alternatively the FDD approach may be a good way forward. The FDD tests at ISIS have demonstrated the sensitivity of such a detector to neutrons above 2 MeV. This could be of interest in relation to tests of electronics devices such as DRAMs where the neutron energy threshold for SEE can be as low as 1 MeV.

The FDD can also be used as beam monitors for neutrons emitted by deuterium-deuterium fusion reactions. Their application is being considered in the CNESM diagnostic system for the SPIDER facility, also developed in this thesis.

The ITER neutral beam test facility under construction in Padova will host two experimental devices: SPIDER, a 100 keV negative hydrogen-deuterium beam, and MITICA, a full scale, 1 MeV deuterium beam. A number of diagnostics will be deployed in the two facilities to qualify the beams. The aim of this thesis was to provide the main elements for the design of a neutron diagnostic for SPIDER, as a first step towards the application of this diagnostic technique to MITICA.

The proposed detection system is called CNESM which stands for Close-contact Neutron Emission Surface Mapping. CNESM will be placed right behind the SPIDER beam dump, as close as possible to the neutron emitting surface. It shall provide the map of the neutron emission on the surface of the beam dump. The latter is a rectangular panel made of water cooled pipes used to stop the incoming beam. Although FDDs would be attractive detectors in this context due to their high radiation hardness and small size, a more effective solution is to equip the CNESM diagnostic system with nGEM neutron detectors. These are Gas Electron Multiplier detectors equipped with a cathode that also serves as neutron-proton converter. The nGEM is expected to provide the neutron emission map with a spatial resolution approaching the size of the footprint of the SPIDER beamlets. This is achieved by using GEMs equipped with a cathode designed for detecting neutrons with an energy higher than 2.2 MeV and with an incidence angle smaller than 40° . This could be done by using an Al-CH₂ cathode. The

CNESM diagnostic system was designed on the basis of simulations of the different steps leading to neutron emission, from deuterium implantation in the beam dump to neutron detection within the nGEM. The simulations reported in this thesis show that the best resolution is achieved by using an Al cathode thickness of about 50 μm . Simulations results were confirmed by experiments performed using nGEM prototypes at a 2.5 MeV neutron source. The experimental results are a good benchmark of the detector directional response obtained in the simulations. The final CNESM detector system will comprise one or two nGEM detectors of active area $20 \times 35 \text{ cm}^2$. It is expected to be built in 2013 and take data in the following year. For the interpretation of the CNESM measurements a more comprehensive detector model simulation will be required. This will provide the basis for corrections for scattered neutrons and other background radiation. It will also be used in support of the unfolding analysis that we envisage will be needed in order to infer the map of the deuterium beam power profile from the measured neutron emission map.

CNESM on SPIDER is a first step towards the application of this diagnostic technique to the MITICA beam test facility, where it will be used to resolve the horizontal profile of the beam intensity. In principle the same detector geometry (and even the same detector system) could be used in MITICA. However the interpretation of the data will be even more challenging due to the higher beam energy of MITICA (1 MeV) compared to SPIDER (100 keV). At 1 MeV the DD fusion cross section is strongly anisotropic and neutrons with energies up to 4 MeV are emitted. The MITICA beam dump will be made of thin copper alloy pipes with an alternating geometry and a tilt angle of as little as 6° relative to the beam direction. Also the large temperature excursion in the copper may affect the deuterium concentration. The analysis and simulations performed in this thesis provide the main elements from which a more comprehensive diagnostic model can be built in support of the final MITICA detector design and later interpretation of the CNESM measurements.

LIST OF FIGURES

1.1	Comparison between the neutron, proton, muon and pion flux at sea level. The neutron flux is the most intense.	4
1.2	Neutron flux above 1 MeV in different neutron facilities compared with the atmospheric one [7].	4
1.3	High energy neutron interaction in an electronic chip. An ionizing charge particle is produced by elastic or inelastic reaction on silicon atoms. The collected charge by the transistor may produce a soft error.	5
1.4	Photo of the ISIS spallation neutron source area, Didcot, UK.	7
1.5	The proton bunch profile, the bunch are 60 ns wide and 322 ns apart. Neutron will be produced with the same temporal structure.	8
1.6	Schematic view of the ISIS facility, including the synchrotron, the extractor and the beam lines.	8
1.7	VESUVIO neutron spectrum simulated with MCNPX [7].	9
1.8	CAD model of the CHIPIR beam line [10].	10
1.9	SPIDER experimental area: the source and the stopping system are shown. The main stopping system, called beam dump, is shown in yellow.	12
1.10	CAD model of the SPIDER beam dump: hypervapotrons are arranged in two panels as shown in (a). Each panel is supported on the back by a steel frame with columns (b).	13

1.11	Cross section of a hypervapotron in the SPIDER beam dump, quotes are in mm.	13
1.12	The SPIDER beam dump area: the beam impinges on the beam dump surface with an incident angle of 30°	14
1.13	Contour plot of the power density profile of a 5X16 beamlet matrix hitting the beam dump. The power density levels are in MW/m^2	15
1.14	Top view of the SPIDER beam dump area: the detector boxes are shown in green.	16
2.1	Cross sections of the most important neutron induced reactions with carbon [24].	21
2.2	Scheme of the configuration of a diamond detector realized at the University of Roma Tor Vergata. From bottom to top: High Pressure High Temperature substrate, B-doped CVD diamond, intrinsic CVD diamond, Al contact.	22
2.3	Photo of diamond detector produced at the University of Roma Tor Vergata.	22
2.4	Photo of the experimental set-up (neutrons are coming from the right).	25
2.5	Signal pulse recorded by the SDD irradiated with α particles from a ^{241}Am source. The SDD was connected to a DBA III preamplifier and a fast digital scope.	25
2.6	Experimental set-up before (a) and after (b) the moderator in the SDD test at the ROTAX beam line.	26
2.7	Experimental set-up after the moderator in the SDD test at the ROTAX beam line.	26
2.8	Time of flight spectrum obtained before the moderator.	27
2.9	Energy spectrum obtained using the SDD-24 coupled to the bi-parametric electronic chain. The energy spectrum is reported for five different values of V_{bias} . The first peak is the peak from alpha particles of ^{241}Am , the second is the peak from the pulse shape generator.	30

2.10	Energy resolution achieved for the SDD-24 as a function of the detector bias supply, V_{bias}	31
2.11	Schematics of the electronic chain used in the measurements performed at ROTAX using the FDD and the SDD.	31
2.12	Scatter plot of the events recorded by the FDD.	32
2.13	Time of flight (a) and E_d (b) spectrum of the SDD.	33
2.14	Scatter plot of all the events recorded by the FDD.	34
2.15	Scatter plot of the events recorded in the first two microseconds by the FDD.	35
2.16	Time of Flight (a) and E_d (b) spectrum of the FDD.	36
2.17	Time of Flight spectrum obtained considering only events which deposit more than 20 MeV in the FDD. These events are due to fission fragments originated by neutron-induced fission on ^{238}U . . .	37
3.1	Picture of the DDL proprietary contact.	40
3.2	A picture of the experimental set-up at the VESUVIO data campaign in October 2011. Neutrons are coming from the right, the detectors are placed directly into the neutron beam. Both detectors were mounted on a movable support used for beam profile measurements. A zoom of the detectors is visible on the left part of the Figure.	41
3.3	Data from the recorded waveform for the Au-SDD (black) and for the Al-SDD (red). The full waveform is 2500 ns long.	42
3.4	Calibration peak for the Au-SDD with ^{241}Am source. The line is a Gaussian fit to the data. The Gaussian parameters are height $I=4 \cdot 10^4$, FWHM= 119 mVns, position $A=589$ mVns.	43
3.5	Calibration peak for the Au-SDD. The data are the amplitude spectrum from a natural uranium source with statistical error bars. The line is a Gaussian fit to the data. The Gaussian parameters are height $I= 25$, width $W= 305$ mVns (FWHM), position $A= 305$ mVns. (b) Same as (a) but for the Al-SDD. The Gaussian parameters are $I = 20$, $W = 435$ mVns, $A = 420$ mVns	44

- 3.6 Scatter plot of A vs h_p for a subset of the data collected with the Au-SDD placed in the VESUVIO neutron beam. The line is a linear best fit to the data. (b) same as (a) but for the Al-SDD. The total number of data points is $1.6 \cdot 10^6$ in (a) and $3.9 \cdot 10^6$ in (b). 45
- 3.7 Contour plot of the event density in the (t_{ToF}, E_d) plane for the Au-SDD (a) and the Al-SDD (b). The total number of events in the plot is $2 \cdot 10^7$ (Al-SDD) and $6.7 \cdot 10^6$ (Au-SDD). The bin width is 1 ns in t_{ToF} and 0.089 (Au-SDD), 0.057(Al-SDD) MeV in E_d . The integrated proton beam current was 4.401 mAh corresponding to a data collection time of 32h. The blue and red lines are the maximum deposited energy for the case of $^{12}\text{C}(n, \alpha)^9\text{Be}$ and elastic $^{12}\text{C}(n, n')^{12}\text{C}$ scattering reactions, respectively. The dashed lines are the same as the full lines but with a shift of ± 35 ns in the t_{ToF} value. 48
- 3.8 Time of flight spectrum for the two detector-amplification combinations used. The black line represents the spectrum for the Au-SDD - DBAIV preamplifier obtained by projecting the data of Figure 3.7 on the horizontal axis. The red line is the same but for Al-SDD - DBAIII preamplifier - 4X amplifier combination. Also shown in blue is the proton pulse signal from the accelerator in arbitrary units. 49
- 3.9 Spectrum of the deposited energy for the two detector-amplification combinations used. The black line represents the E_d spectrum for the Au-SDD - DBAIV preamplifier obtained by projecting the data of Figure 3.7 on the vertical axis. The red line is the same but for Al-SDD - DBAIII preamplifier - 4X amplifier combination. The E_d bin width is the same as in Figure 3.7. The vertical scales are adjusted to provide a good match between the two traces in the range $5 \text{ MeV} < E_d < 20 \text{ MeV}$ 50

- 3.10 Contour plot of the event density in the (t_{ToF}, E_d) plane for the Au-SDD on the ROTAX beamline. The total number of events in the plot is $3 \cdot 10^7$. The bin width is 1 ns in t_{ToF} and 0.065 MeV in E_d . The integrated proton beam current was 11.7 mAh corresponding to a data collection time of 65h. The blue and red lines have the same meaning as in Figure 3.7 and were calculated assuming a flight distance $L=14.2$ m. 51
- 3.11 Time of flight spectrum for the Au-SDD - DBAIII preamplifier - 4X amplifier combination on the ROTAX beam line (blue). For comparison the spectra of Figure 3.8 are also shown. 52
- 3.12 Spectrum of the deposited energy for the Au-SDD - DBAIII preamplifier - 4X amplifier combination on the ROTAX beamline (blue). The same spectrum divided by 5 is shown for comparison with spectra obtained on VESUVIO with the same amplification chain coupled to either Au-SDD (black) or Al-SDD (red). The vertical scales are adjusted to show a good match between the two data sets collected on VESUVIO. 53
- 3.13 E_d spectrum for the Au-SDD for the t_{ToF} values reported in the legend. The t_{ToF} bin width is 5 ns. The E_d bin width is 0.089 MeV. 54
- 3.14 t_{ToF} spectrum for the Au-SDD for the E_d intervals reported in the legend. The t_{ToF} bin width is 1 ns. 55
- 3.15 Horizontal beam profile obtained by selecting events with (a) $E_d < 5$ MeV and $t_{ToF} < 75$ ns, (b) $E_d > 5$ MeV, $200 < t_{ToF} < 250$ ns (black), and $E_d > 15$ MeV (red). Each point corresponds to a 15 minute long run. The integrated current was typically 45 μ Ah in each point. The lines are a Gaussian fit to the data. 56
- 4.1 Predicted (lines) and measured (symbols) neutron yield from copper beam dump at deuterium beam facilities [39]. 60
- 4.2 Planar projection of ion trajectories generated by a TRIM simulation for 100 keV deuterium and 60 degrees incidence in CuCrZr-alloy. 61
- 4.3 Penetration depth distribution of implanted deuterium in the beam dump. 62

4.4	Electronic (ionization) energy loss of deuterium ions vs penetration depth. Also shown is the energy loss due to recoiling target atoms (x100).	63
4.5	Average deuterium energy as fraction of the incident energy ($E_0=100$ keV) as function of penetration depth.	63
4.6	Ion damage (displacements per atom) at different times after switch on of the deuterium beam.	64
4.7	Deuterium concentration profile at different times after switch on of the deuterium beam.	66
4.8	Cross Section for the $D(d,n)^3He$ reaction as function of deuterium energy (a) and of the penetration depth (b).	68
4.9	Neutron emission profile as a function of penetration depth (z) after the irradiation times reported in the legend.	69
4.10	Neutron emission rate as a function of the irradiation time.	70
4.11	Cross section of the 2D beam dump model used for the simulations. In this example neutrons from a point neutron source (green) cross layers of copper alloy (red) and water (light blue) before reaching the detection surface (black) located at 30 mm from the source. also visible on the right is the cross section of a steel column (grey) used to estimate the importance of scattered neutrons from the beam dump support.	72
4.12	Differential Cross Section for the DD beam-target reaction with beam energies $E_d=50$ keV (red), and $E_d=100$ keV (black). [45] . . .	73
4.13	Neutron intensity at the detection surface as a function of position along the x axis. A point source of unit intensity is placed at 30 mm from the detection surface. The red line is the flux from an isotropic source. The black line is the flux from a unit source with an anisotropy coefficient $1+\cos^2\theta$ where θ is the angle relative to the deuteron beam direction.	74

4.14	Neutron intensity at the detection surface as a function of position along the x axis. A unit point source is placed at 30 mm from the detection surface. The red curve is the same as in Figure 4.13. The black curve shows the effect of the beam dump placed between source and detector.	75
4.15	Contour plot of the neutron intensity on the detector surface due to a unit uniform plane source of area 200x352 mm ² . The intensity is in m ⁻²	76
4.16	Neutron intensity profile along the x direction for z=0. The red line is taken from the data of Figure 4.15. The black line shows the effect of neutron scattering from the iron column added to the MCNPX model.	77
4.17	Same as Figure 4.16 but for the z direction and x=100 mm (a), and x=0 mm (b).	78
4.18	Neutron energy spectrum at three positions on the detector surface with z=0 and x=-100 mm (black), 0 mm (red) and 100 mm (blue).	79
4.19	Contour plot of the neutron intensity on the detector surface due to a unit uniform plane source of area 40x22 mm ² centred at the coordinate origin. The intensity is in m ⁻²	81
4.20	Neutron intensity profile along the x direction for z=0 (a) and along the z direction for x=0 (b). Data from Figure 4.19.	82
4.21	Neutron intensity on the detector surface due to a unit uniform plane source of area 40x22 mm ² centred at the coordinate origin. The intensity is in m ⁻²	83
5.1	ToF Spectrum obtained considering only fission events from ²³⁸ U, compared to simulation results.	86
5.2	Cross section of the geometry of GEM foil and the bi-conical shape of the holes.	88
5.3	Cross section of a single (a) and triple (b) GEM detector.	89
5.4	Readout board with 8 CARIOCA chips.	91

5.5	A thick Al cathode (grey) is used to suppress detection of neutrons with oblique incidence. Only one of the four protons in the figure can cross the Al layer and produce a discharge in the GEM gas. . .	92
5.6	A thick Al cathode (grey) is used to suppress detection of neutrons with oblique incidence. Only one of the four protons in the figure can cross the Al layer and produce a discharge in the GEM gas. . .	93
5.7	Simulated distribution of proton energy deposition inside the nGEM gas for different Al thicknesses. The neutron incident angle is set at $\theta_n = 0^\circ$	94
5.8	Simulated distribution of proton energy deposition inside the nGEM gas for different neutron incident angles θ_n . The thickness of the Al foil was $t=43 \mu\text{m}$	95
5.9	Simulated distribution of proton energy deposition inside the nGEM gas for different neutron incident angles θ_n . The thickness of the Al foil was $t=51 \mu\text{m}$	96
5.10	Integrated number of events with proton energy deposition above threshold inside the nGEM gas for different neutron incident angles θ_n and different Al thicknesses t	97
5.11	Ratio $\rho = N(\theta_n = 0^\circ)/N(\theta_n = 40^\circ)$ between the number of events above threshold at $\theta_n = 40^\circ$ and $\theta_n = 0^\circ$, plotted as a function of Al thickness t . The threshold is $E_{dth}=72 \text{ keV}$ (dash line) and $E_{dth}=200 \text{ keV}$ (full line).	98
5.12	Simulated nGEM response to neutrons emitted along the x-position at a distance $d=30 \text{ mm}$ from the nGEM. The nGEM response is much sharper when the cathode is equipped with a $49 \mu\text{m}$ Al foil (continuous line) than without the Al foil (dashed line).	99
5.13	Integral detector response for the cases with (continuous line) and without (dashed) a $49 \mu\text{m}$ Al foil. The neutron emission is assumed to be uniform on a surface placed at $d=30 \text{ mm}$ from the nGEM. The quantity plotted is the relative number of recorded events due to neutrons emitted from within a circle of radius x	100
5.14	Analog (a) and digital (b) nGEM prototypes, installed at the FNG 2.5 MeV neutron source.	101

- 5.15 nGEM response as a function of the neutron flux. $\Sigma\Delta V_{GEM}=1020$ V; E_d (Drift Field)= E_{T1} (Transfer 1 Field)= $E_{T2}=3$ kV/cm, E_{Ind} (Induction Field)=5 kV/cm; Gas Mixture Ar/CO₂/CF₄ (45%/15%/40%). 102
- 5.16 Pulse height spectrum measured at the FNG neutron source for different θ_{GEM} values. 103
- 5.17 Integrated pulse height spectrum above the threshold $E_{dth} = 137$ keV as function of the θ_{GEM} 104
- 5.18 Experimental pulse height spectrum (black line) compared to the simulated one. An Al-foil thickness equal to 33 μ m (red line), 38 μ m (green line) and 43 μ m (blue line) was used in simulations. The neutron incidence angle in this case was 0°. 105
- 5.19 Integrated PH spectrum above 127 keV. Experimental data are reported in black, the red line represent the simulated angular response with Al-foil thickness of 33 μ m, the green line 38 μ m and the blue line considering 43 μ m of aluminium. 105

LIST OF TABLES

1.1	Reaction products and thresholds for the $n + {}^{28}\text{Si}$ reaction. . . .	5
2.1	Diamond characteristics compared to those of Si and Ge [20]. . . .	20
4.1	Relative contribution of scattered neutrons to the total intensity at different detection positions and for detection thresholds. . . .	80

BIBLIOGRAPHY

- [1] T. J. O’Gorman, J. M. Ross, A. H. Taber, J. F. Ziegler, H. P. Muhlfeld, C. J. Montrose, H. W. Curtis, and J. L. Walsh, “Field testing for cosmic ray soft errors in semiconductor memories,” *IBM J. Res. Dev.*, vol. 40, p. 3, 1996.
- [2] P. E. Dodd and L. W. Massengill, “Basic Mechanisms and modelling of single event upsets in digital microelectronics,” *IEEE Trans. on Nucl. Sci.*, vol. 50, pp. 583 – 602, 2003.
- [3] J. Ziegler and W. Lanford, “The Effect of Sea-Level Cosmic Rays on Electronic Devices,” *J. Appl. Phys.*, vol. 52, pp. 4305 – 4312, 1981.
- [4] R. Baumann, “Soft errors in commercial integrated circuits,” *International Journal of High Speed Electronics and Systems (IJHSES)*, vol. 14, pp. 299 – 309, 2004.
- [5] R. Baumann, “Soft errors in advanced computer systems,” *Design Test of Computers, IEEE*, vol. 22, pp. 258 – 266, 2005.
- [6] T. C. May and M. H. Woods, “A new physical mechanism for soft error in dynamic memories,” *Proc. 16th Int. Reliability Physics Symp. (IRPS)*, pp. 33 – 40, 1978.
- [7] C. Andreani, A. Pietropaolo, A. Salsano, G. Gorini, M. Tardocchi, A. Paccagnella, S. Gerardin, C. D. Frost, S. Ansell, and S. P. Platt, “Fa-

- cility for fast neutron irradiation tests of electronics at the ISIS spallation neutron source,” *Applied Physics Letters*, vol. 92, no. 11, p. 114101, 2008.
- [8] <http://lansce.lanl.gov/>.
- [9] <http://www.triumf.ca/>.
- [10] <http://www.isis.stfc.ac.uk/instruments/Chipir/>.
- [11] <http://www.isis.stfc.ac.uk/>.
- [12] R. Bedogni, A. Esposito, C. Andreani, R. Senesi, M. P. D. Pascale, P. Picozza, A. Pietropaolo, G. Gorini, C. D. Frost, and S. Ansell, “Characterization of the neutron field at the ISIS-VESUVIO facility by means of a bonner sphere spectrometer,” *Nucl. Instrum. and Meth. A*, vol. 612, pp. 143–148, 2009.
- [13] <http://www.isis.stfc.ac.uk/about-isis/target-station-2/>.
- [14] <http://www.iter.org/>.
- [15] <http://www.igi.cnr.it/>.
- [16] J. Ziegler. <http://www.srim.org/>.
- [17] <http://mcnpx.lanl.gov/>.
- [18] E. Bartz, J. Doroshenko, V. Halyo, B. Harrop, D. Hits, A. Macpherson, D. Marlow, L. Perera, S. Schnetzer, and R. Stone, “A CMS Luminosity Monitor Using Single-Crystal CVD Diamond Pixel Detectors,” *Journ. Instrum.*, vol. 4, p. P04015, 2009.
- [19] J. Kaneko, T. Tanaka, T. Imai, Y. Tanimura, M. Katagiri, T. Nishitani, H. Takeuchi, T. Sawamura, and T. Iida, “Radiation detector made of a diamond single crystal grown by a chemical vapor deposition method,” *Nucl. Instr. and Meth. A*, vol. 505, p. 187190, 2003.

- [20] J. Isberg, J. Hammersberg, E. Johansson, T. Wikstrm, D. J. Twitchen, A. J. Whitehead, S. E. Coe, and G. A. Scarsbrook, “High Carrier Mobility in Single-Crystal Plasma-Deposited Diamond,” *Science*, vol. 297, no. 5587, pp. 1670–1672, 2002.
- [21] M. Marinelli, E. Milani, A. Paoletti, A. Tucciarone, G. V. Rinati, M. Angelone, and M. Pillon, “High quality diamond grown by chemical-vapor deposition: improved collection efficiency in α -particle detection,” *Appl. Phys. Lett.*, vol. 75, p. 3216, 1999.
- [22] M. Marinelli, E. Milani, A. Paoletti, A. Tucciarone, G. V. Rinati, M. Angelone, and M. P. M., “Systematic study of the normal and pumped state of high efficiency chemical vapor deposited ty diamond particle detectors,” *Appl. Phys. Lett.*, vol. 89, p. 1490, 2001.
- [23] S. Almagora, M. Marinelli, E. Milani, G. Prestopino, A. Tucciarone, C. Verona, G. Verona-Rinati, M. Angelone, M. Pillon, I. Dolbnya, K. Sawhney, and N. Tartoni, “Chemical vapor deposition diamond based multilayered radiation detector: Physical analysis of detection properties,” *J. Appl. Phys.*, vol. 107, no. 014511, 2010.
- [24] <http://www-nds.iaea.org/exfor/exfor.html>.
- [25] P. Moritz, *Broadband Preamplifiers for Fast Particle Detectors*. GSI - Gesellschaft fr Schwerionenforschung mbH, Planckstr. 1, D-64291 Darmstadt, Germany.
- [26] CAEN S.p.a., Via Vetraria, 11 55049 - Viareggio (LU) - Italy, *Mod. N1728A/N1728B 4 Ch. Flash ADC*. User’s Manual (MUT).
- [27] V. Jordanov and G. Knoll, “Digital techniques for real-time pulse shaping in radiation measurements,” *Nucl. Instrum. Methods A*, vol. 345, p. 337, 1994.
- [28] A. N. Smirnov, A. V. Prokofiev, E. E. Rodionova, C. D. Frost, S. Ansell, E. M. Schooneveld, G. Gorini, and A. Pietropaolo, “Characterisation of the high-energy neutron field at the ISIS-VESUVIO facility by means

- of thin-film breakdown counters,” *Technical Report RAL-TR-2010-024*, 2010.
- [29] M. Pillon, M. Angelone, A. Krasab, A. Plompen, P. Schillebeeckx, and M. Sergi, “Experimental Response Functions of a Single-Crystal Diamond Detector for 5-20.5 MeV Neutrons,” *Nucl. Instrum. Meth. A*, pp. 185–191, 2011.
- [30] M. Pillon, M. Angelone, and A. Krasilnikov, “14 MeV neutron spectra measurements with 4% energy resolution using a type IIa diamond detector,” *Nucl. Instr. Meth. B*, vol. 101, pp. 473–483, 1995.
- [31] L. Giacomelli, C. Andreani, A. Fazzi, C. Frost, G. Gorini, E. P. Cippo, A. Pietropaolo, M. Rebai, H. Schuhmacher, M. Tardocchi, C. Verona, G. V. Rinati, and A. Zimbal, “Diamond detectors for fast neutron irradiation experiments,” *Nuclear Physics B (Proceedings Supplements)*, vol. 215, pp. 242–246, 2011.
- [32] A. Pietropaolo, C. Andreani, M. Rebai, L. Giacomelli, G. Gorini, E. P. Cippo, M. Tardocchi, A. Fazzi, G. V. Rinati, C. Verona, M. Marinelli, E. Milani, C. D. Frost, and E. M. Schooneveld, “Fission diamond detectors for fast-neutron ToF spectroscopy,” *Eur. Phys. Letters*, vol. 94, p. 62001, 2011.
- [33] <http://www.diamonddetectors.com/>.
- [34] <http://www.isis.stfc.ac.uk/instruments/vesuvio/>.
- [35] A. Galbiati, S. Lynn, K. Oliver, F. Schirru, T. N. B. Marczevska, J. D. ans R. Berjillos, I. Martel, and L. Lavergne, “Performance of monocrySTALLINE diamond radiation detectors fabricated using TiW, Cr/Au and a Novel Ohmic DLC/Pt/Au Electrical Contact,” *IEEE Trans. Nucl. Science*, vol. 56, p. 1863, 2009.
- [36] CAEN S.p.a., Via Vetraia, 11 55049 - Viareggio (LU) - Italy, *Mod. DT5751 - 2/4 Ch. 10 bit 2/1 GS/s Digitizer*. User’s Manual (MUT).

- [37] <http://www.python.org/>.
- [38] <http://www.isis.stfc.ac.uk/instruments/rotax/>.
- [39] ENEA, *Appendix H Report RTI ION-IRP*, 2004. Safety Analysis for the First ITER NB.
- [40] J. Kim, “DD neutron and X-rays yields from high power deuterium beam injectors,” *Nucl. Technol.*, vol. 44, p. 315, 1979.
- [41] W. Moller and F. Roth, *Implantation, retention and release of hydrogen isotopes in solids*. New York: Physics of Plasma-Wall Interactions in Controlled Fusion, 1986.
- [42] D. Brice, B. Doyle, and W. Wampler, “Extended Local Mixing Model for hydrogen retention and isotope exchange,” *Joun. Nucl. Mater.*, vol. 111/112, p. 598, 1982.
- [43] B. Doyle, W. Wampler, and D. Bric, “Temperature dependence of H saturation and isotope exchange,” *J. Nucl. Mater.*, vol. 103/104, p. 513, 1981.
- [44] M. Nocente, G. Gorini, J. Källne, and M. Tardocchi, “Cross section of the $d + {}^3\text{He} \rightarrow \alpha + p$ reaction of relevance for fusion plasma application,” *Nucl. Fusion*, vol. 50, p. 055001, 2010.
- [45] H. Liskien and A. Paulsen, “Neutron production cross sections and energies for the reactions $T(p,n){}^3\text{He}$, $D(d,n){}^3\text{He}$, and $T(d,n){}^4\text{He}$,” *Nucl. Data Tables*, vol. 11, pp. 569–619, 1973.
- [46] G. F. Knoll, *Radiation Detection and Measurements*. John Wiley and Sons, New York, NY, 1979.
- [47] F. Sauli, “GEM: A new concept for electron amplification in gas detectors,” *Nucl. Instr. and Meth. A*, vol. 386, p. 531, 1997.
- [48] G. Charpak, R. Bouclier, T. Bressani, J. Favier, and C. Zupancic, “The use of multiwire proportional counters to select and localize charged particles,” *Nucl. Instr. and Meth. A*, vol. 62, p. 262, 1968.

- [49] J. Benlloch, A. Bressan, M. Capeans, M. Gruwe, M. Hoch, J. Labbe, A. Placci, L. Ropelewski, and F. Sauli, "Further developments and beam tests of the gas electron multiplier," *Nucl. Instr. and Meth. A*, vol. 419, p. 410, 1998.
- [50] J. M. Benlloch, A. Bressan, C. Bttner, M. Capans-Garrido, M. Gruw, M. Hoch, J. C. Labb, A. Placci, L. Ropelewski, F. Sauli, A. Sharma, and Veenhof, "Development of the gas electron multiplier (GEM)," *IEEE Trans. on Nucl. Science*, pp. 234 – 243, 1998.
- [51] S. Bachmann, A. Bressan, L. Ropelewski, F. Sauli, A. Sharma, and D. Mrmann, "Charge amplification processes in the gas electron multiplier," *Nucl. Instr. and Meth. A*, vol. 438, p. 376, 1999.
- [52] A. Bressan, J. Labb, P. Pagano, L. Ropelewski, and F. Sauli, "Beam tests of the gas electron multiplier," *Nucl. Instrum. and Meth. A*, vol. 425, no. 1-2, pp. 262 – 276, 1999.
- [53] G. Corradi, F. Murtas, and D. Tagnani, "A novel high voltage system for a triple GEM detector," *Nucl. Instr. and Meth. A*, vol. 46, p. 128, 2009.
- [54] M. Alfonsi, G. Bencivenni, W. Bonivento, E. Cardelli, A. Cardini, P. de Simone, D. Domenici, F. Murtas, D. Pinci, M. P. Lener, D. Raspino, and B. Saitta, "Production and performance of LHCb triple-GEM detectors equipped with the dedicated cardiac-gem front-end electronics," *Nucl. Instrum. and Meth. A*, vol. 572, no. 1, pp. 12 – 13, 2007.
- [55] W. Bonivento, P. Jarron, D. Moraes, W. Riegler, and F. dos Santos, "Development of the CARIOCA front-end chip for the LHCb muon detector," *Nucl. Instrum. and Meth. A*, vol. 491, no. 1-2, pp. 233 – 243, 2002.
- [56] M. Martone, M. Angelone, and M. Pillon, "The 14 MeV Frascati neutron generator," *Journal of Nuclear Materials*, vol. 212-215, pp. 1661–1664, 2002.

-
- [57] G. Bencivenni, G. Felici, F. Murtas, P. Valente, W. Bonivento, A. Cardini, A. Lai, D. Pinci, B. Saitta, and C. Bosio, “A triple GEM detector with pad readout for high rate charged particle triggering,” *Nucl. Instr. and Meth. A*, vol. 488, pp. 493–502, 2002.

Synopsis of attached papers

- **Paper I**

M.Rebai, G. Gorini, E. Perelli Cippo, A. Pietropaolo, M. Tardocchi, A. Fazzi, E. Milani, G. Verona Rinati, C. Andreani, R. Senesi, C. D. Frost, E. M. Schooneveld, N. J. Rhodes, R. Bedogni and A. Esposito, “Development of high energy neutron counters for the CHIPIR beamline at ISIS-TS2”,
PSI-Report ISSN-Nr. 1019-6447, XIX ICANS Proceeding Conference, Grindelwald - Switzerland, 2010.

The motivations for the diamond detectors development at ISIS is provided. The measurements of the so-called Single Event Effects (SEE) are becoming of great importance to assess the robustness of integrated circuits featuring dimensions of tens of nanometers. Recent experiments performed at ISIS on the VESUVIO beamline to measure the SEE rate in chips of different technologies demonstrate the suitability of the ISIS neutron source for this kind of application. Therefore at ISIS a dedicated beam line for chip irradiation (ChipIr) will be realized. A very important task for ChipIr is the development of suitable neutron beam monitors that can measure the neutron fluence in the energy region above 1 MeV. The first measurements performed at ISIS using a diamond detector as a fast neutron beam monitor are presented.

A description of measurements performed with Bonner spheres is also provided.

- **Paper II**

A. Pietropaolo, C. Andreani, **M. Rebai**, L. Giacomelli, G. Gorini, E. Perelli Cippo, M. Tardocchi, A. Fazzi, G. Verona Rinati, C. Verona, M. Marinelli, E. Milani, C. D. Frost and E. M. Schooneveld, “Single-crystal diamond detector for time-resolved measurements of a pulsed fast-neutron beam”, *Eur. Phys. Letters*, **92**, 68003, 2010 ¹.

The main features of a fast-neutron diamond detector prototype for time-resolved beam measurements at spallation neutron sources are presented. The device features a p-type/ intrinsic/metal Schottky barrier structure where the active (intrinsic) detection layer is a 150 μm thick single-crystal diamond obtained by chemical-vapour deposition. Coupling to fast front-end electronics preserves the excellent timing properties of the device as demonstrated in tests performed at the ISIS spallation neutron source in UK. The diamond detector can provide a localized (mm resolution) fast-neutron fluence measurements required by neutron irradiation experiments, which is not possible to provide, e.g., using Bonner spheres. The case is made for new experiments providing biparametrical (pulse height and time of flight) information using a thicker detector.

¹Paper reprinted with permission from the Europhysics letters; ©Europhysics Letters-European Physical Society.

- **Paper III**

M. Rebai, C. Andreani, A. Fazzi, C.D. Frost, L. Giacomelli, G. Gorini, E. Milani, E. Perelli Cippo, A. Pietropaolo, G. Prestopino, E. Schooneveld, M. Tardocchi, C. Verona and G. Verona Rinati,
“Fission diamond detector tests at the ISIS spallation neutron source”,
Nucl. Phys B (Proc. Suppl.), **215**, 313-315, 2011 ².

Measurements performed using a Fission Diamond Detector (FDD) are described in this paper. The FDD is based on a single crystal diamond, identical to the one described in Paper II, coupled to a uranium converter foil where neutron interaction results in emission of charged fission products detected by the diamond. Thermal and fast neutrons are detected using natural uranium containing both ^{235}U and ^{238}U . Biparametric (pulse height and time of flight) data collection is used to distinguish events from ^{235}U , ^{238}U and from carbon break-up reactions inside the diamond.

- **Paper IV**

L. Giacomelli, **M.Rebai**, A. Fazzi, E. Perelli Cippo, M. Tardocchi, A. Andreani, C. Frost, A. Pietropaolo, E. Schooneveld and G. Gorini,
“Diamond detector for high rate monitors of fast neutron beams”, to appear in Proceedings of the International Workshop on Fusion Neutrons and Sub-critical Nuclear Fission (FUNFI) held at Villa Monastero, Varenna (Italy) September 12-15, 2011.

This paper presents the first results on the use at ISIS of a commercial single crystal diamond detector (SDD) coupled to a fast digital data

²Paper reprinted with permission from Elsevier B. V .; ©Elsevier B.V.

acquisition system. The detector was tested at the ROTAX neutron beam line. The SDD event signal is digitalized at 1 GHz to reconstruct its deposited energy (pulse-height) and arrival time; the event time of flight (ToF) is obtained from the recorded proton beam signal. A fast acquisition is needed because the peak count rate is very high (800 kHz) due to the pulsed structure of the ISIS neutron beam. Measurements at ROTAX indicate that three characteristic regions exist in the biparametric (ToF, pulse-height) spectrum: i) background gamma events of low pulse-heights; ii) low pulse-height neutron events in the energy range $E_n = 1.5-6$ MeV ascribed to neutron elastic scattering on ^{12}C ; iii) large pulse-height neutron events with $E_n > 6$ MeV ascribed to $^{12}\text{C}(n, \alpha)^9\text{Be}$ and $^{12}\text{C}(n, n')^3\alpha$.

- **Paper V**

M.Rebai, G.Croci, M. Cavenago, M. Dalla Palma, G. Gervasini, F. Ghezzi, G. Grosso, F. Murtas, R. Pasqualotto, E. Perelli Cippo, M. Tardocchi, M. Tollin and G. Gorini,
“A neutron diagnostic for high current deuterium beams”,
accepted for publication in *Rev. Sci. Instrum.*, 2011.

In this paper a neutron diagnostic for high current deuterium beams is proposed for installation on the SPIDER test beam facility. The ITER neutral beam test facility under construction in Padova will host two experimental devices: SPIDER, a 100 kV negative H/D RF source, and MITICA, a full scale, 1 MeV deuterium beam injector. Detection of fusion neutrons will be used as a means to resolve the horizontal beam intensity profile. The proposed detection system is called Close-contact Neutron Emission Surface Mapping (CNESM). The diagnostic aims at providing the map of the neutron emission on the beam dump surface by placing a detector in close contact, right behind the dump. CNESM

uses nGEM neutron detectors. These are Gas Electron Multiplier detectors equipped with a cathode that also serves as neutron-proton converter foil. The cathode is made of a thin polythene film (nominal thickness 50 μm) and an aluminium film (nominal thickness 50 μm); it is designed for detection of neutrons of energy > 2.2 MeV with an incidence angle $< 45^\circ$. CNESM was designed on the basis of simulations of the different steps from the deuteron beam interaction with the beam dump to the neutron detection in the nGEM. Neutron scattering was simulated with the MCNPX code. In the paper the results of the detector system simulations are presented.

- **Paper VI**

G. Croci, **M. Rebai** G. Claps, M. Cavenago, M. Dalla Palma, G. Gervasini, G. Grosso, F. Murtas, R. Pasqualotto, E. Perelli Cippo, M. Tardocchi, M. Tollin, G. and Gorini,
“nGEM neutron diagnostic for high power deuterium beams”,
submitted to *Journ. of Instrum.*, December 2011.

The simulated performance and first prototypes tests of the CNESM diagnostic are described. The nGEM cathode is designed to ensure that most of the detected neutrons at a point of the nGEM surface are emitted from the corresponding 40×22 mm² beamlet footprint on the dump front surface. The nGEM readout pads (area 20×22 mm²) will record a useful count rate of ≈ 5 kHz providing a time resolution of temporal structures in the neutron fluency rate to be measured of better than 1 s. The directional response of the nGEM to neutrons is a key to reducing the scattering contribution to the measured neutron flux. First results achieved using small size nGEM prototypes show that these detectors have the directionality property expected from the MCNP simulations. In addition they have a neutron efficiency detec-

tion of about $2 \cdot 10^{-5}$ and their response scales linearly following the intensity of the neutron flux.

Paper I

ICANS XIX,
19th meeting on Collaboration of Advanced Neutron Sources
March 8 – 12, 2010
Grindelwald, Switzerland

**DEVELOPMENT OF HIGH ENERGY NEUTRON COUNTERS FOR THE CHIPIR
BEAM LINE AT ISIS-TS2**

Marica Rebai, Giuseppe Gorini, Enrico Perelli Cippo
*Dipartimento di Fisica "G. Occhialini", Università degli Studi di Milano-Bicocca,
Piazza della Scienza 3, 20126 Milano, Italy*

and

Antonino Pietropaolo
CNISM UdR Tor Vergata, via della Ricerca Scientifica 1, 00133 Roma, Italy

and

Marco Tardocchi
CNR-IFP "Piero Caldirola", Via Roberto Cozzi, 53 20125 Milano, Italy

and

Alberto Fazzi
Politecnico di Milano, Via Ponzio, 34 20133, Milano, Italy

and

Enrico Milani, Gianluca Verona Rinati
*Dipartimento di Ingegneria Meccanica, Università degli Studi di Roma Tor Vergata,
via del Politecnico 1, 00133 Roma, Italy*

and

Carla Andreani, Roberto Senesi
*Dipartimento di Fisica and centro NAST, Università degli Studi di Roma Tor Vergata,
via della Ricerca Scientifica 1, 00133 Roma, Italy*

and

Christopher D. Frost, Erik M. Schooneveld, Nigel J. Rhodes
*Science and Technology facility Council, ISIS Facility, OX110QX Chilton,
United Kingdom*

and

Roberto Bedogni, Adolfo Esposito
INFN, Laboratori Nazionali di Frascati, Via E. Fermi n. 40, 00044 Frascati (RM), Italy

ICANS XIX,
19th meeting on Collaboration of Advanced Neutron Sources
March 8 – 12, 2010
Grindelwald, Switzerland

ABSTRACT

The measurements of the so-called Single Event Effects (SEE) are becoming of great importance to assess the robustness of integrated circuits featuring dimensions of tens of nanometers. SEEs occur when a highly energetic particle (e.g. a neutron present in the environment) causes a disruption of the correct operation of an electronic component by striking its sensitive regions. Commercial-off-the-shelf devices are becoming popular in mission- or safety-critical applications, since they satisfy the designers' need for high-performance computing at moderate prices. However, to exploit such devices, fault-tolerant design techniques must be employed, and extensive analyses are needed to qualify their robustness. Experiments with atmospheric neutrons at different altitudes can be carried out but, due to the low intensity, they require very long periods of data acquisition. Neutron sources represent an opportunity due to the availability of high intensity fluxes which allow accelerated irradiation experiments. Recent experiments performed at ISIS on the VESUVIO spectrometer to measure SEE rate in chips of different technologies demonstrated the suitability of the ISIS source for this kind of application. The PANAREA project aims at the design and construction of a dedicated beam line for chip irradiation: the ChipIr instrument. A very important task for ChipIr design is the development of suitable and effective neutron beam monitors capable of locally measure the neutron fluence in the energy region above 1 MeV up to 800 MeV. In this contribution we will present the first test results obtained with Bonner Spheres and Single Crystal Diamond detectors.

1. Introduction

The growing availability of integrated circuits featuring minimum dimensions of the order of tens of nanometers is affecting properties and design methodologies of digital systems. These digital devices are more susceptible to random faults, known as Single Event Effects (SEEs), which can occur when a highly energetic particle such as a neutron present in the environment, causes a disruption of their correct operation by striking sensitive regions of an electronic device [1]. SEEs have already been identified as a predominant threat to aircraft safety [2] and the effects on electronic components from cosmic radiation is of significant importance for the semiconductor industry [3]. Commercial off-the-shelf devices are becoming popular in mission- or safety-critical applications since they satisfy the designers' need for high-performance computing at moderate prices. However, to exploit such devices, fault-tolerant design techniques must be employed, and extensive analyses are needed in order to qualify the robustness of the devices and systems. Experiments with atmospheric neutrons at different altitudes can be carried out, but due to low intensity, they require very long periods of data acquisition [4] In this context, neutron sources represent an opportunity thanks to the availability of high intensity fluxes, which allow accelerated irradiation experiments. Currently, semiconductor industries perform irradiation tests, for example, at the Los Alamos Neutron Science Center [5] (LANSCE) and TRIUMF [6] neutron sources. Recently, irradiation tests performed on the VESUVIO beam line at ISIS-TS1, have assessed the effectiveness of the facility for this kind of investigations. A new beam line, dedicated to chip irradiation is under construction on TS2 at ISIS and will benefit from the higher fluxes and from a properly designed moderator that will provide a neutron beam closely resembling the atmospheric spectrum but with a flux higher by almost seven order of magnitudes with respect to the atmospheric one. One important aspect in SEE measurement is both the matching of the neutron spectrum with the atmospheric one and the precise measurement of the neutron fluence onto an irradiated chip for the calculation of the SEE cross sections, defined as the ratio of the number of observed SEEs in a test to the neutron fluence. The spectrum of the neutrons may be measured in different detection systems, such as fission chambers [7], activation targets [8]

or Bonner Spheres Spectrometers (BSS) [9]. These devices give a spatially integrated information due to their dimensions, typically of several tens of cm^2 , that prevent to perform localised (mm^2) measurements. While spectral uniformity of a neutron beam could be a reasonable assumption, the intensity uniformity may not, so that the intensity within the beam spot at the irradiation distance from the moderator may show a spatial variation. Moreover in case of multiboards irradiation, the intensity along the beam may differ due to scattering and/or absorption. Thus, a key issue to be addressed is the development of $\sim\text{mm}^2$ -size fast neutron flux monitors, capable of being embedded close to the irradiated chip. In this contribution we report a few test results obtained on the VESUVIO beam line at the ISIS-TS1 with Bonner Spheres and Single Crystal Diamond detectors [10-12].

2. Experiment

The tests with Bonner Spheres and the Single Crystal Diamond detector were performed on the VESUVIO instrument at the ISIS spallation neutron source (Didcot, U.K.). VESUVIO is a neutron spectrometer, with a primary flight path of 11.05 m, facing a 300 K liquid water moderator. The ISIS proton bunch extracted from the synchrotron is characterized by a double pulse 60-80 ns Full Width Half Maximum, separated by about 300 ns. The neutron spectrum from the moderator has a peak in the thermal energy region and a E^β ($-1 < \beta \leq -0.9$)-dependence in the epithermal neutrons region. The BSS is currently the most used, mature and validated technique for neutron dosimetry and spectrometry in complex neutron fields with energy distribution ranging from thermal up to hundreds MeV [13]. The BSS has been used around high-energy particle accelerators [14-17], on high altitude mountains [18] and at flight altitude [19]. Firstly used by Bramblett et al. [14], the BSS has been widely applied for almost 50 years in the field of neutron dosimetry and spectrometry, due to the wide energy range covered, the possibility to choose among different active or passive thermal neutron sensors according to the characteristics of the field to be measured (intensity, time structure, amount of photons), the isotropy of the response and the easy operation. The BSS relies on a thermal neutron detector placed at the center of a moderating sphere of variable diameter (2''- 15''). The central detector counts neutrons that are moderated and thermalized in the sphere. The neutron moderation process within a BS is mainly due to H(n,n)H and C(n,n)C elastic scattering, at energies below 4 MeV. At higher energies, the threshold reactions C(n,n' γ) (threshold \sim 5 MeV), C(n, α) (7 MeV), C(n,n' γ) (8 MeV), C(n,p) (15 MeV), C(n,n' γ) (15.5 MeV), C(n,p) (18 MeV) become important [20]. A set of five-six well chosen spheres of pure polyethylene with diameters from 2'' to 12'' is sufficient to determine neutron spectra from thermal up to 20 MeV. To extend the upper limit up to 10^2 - 10^3 MeV, additional spheres with metallic inserts (Fe, Cu, W, Pb) are needed [18]. At energy $>$ 20 MeV these metals act as (n,xn) radiators and energy shifters, making the detection of the high-energy neutrons possible. Figure 1 reports a picture of the spheres with metallic inserts.

ICANS XIX,
19th meeting on Collaboration of Advanced Neutron Sources
March 8 – 12, 2010
Grindelwald, Switzerland



Figure 1. Bonner spheres with metallic inserts.

The BSS exposures on VESUVIO took place on 9 – 10 May 2008. The proton current ranged between 170 μA and 190 μA . Each sphere was exposed for about 20 minutes. The Dy activation foils were counted and their saturation specific activity, ranging from 10^3 to $10^5 \text{ Bq}\cdot\text{g}^{-1}$, was normalized to the proton current, obtaining a suitable set of input data for the unfolding code FRUIT ver 3.0 [21]. The energy distribution of the neutron fluence rate is shown in Figure 2. As expected, the thermal component is dominating. The slope of the epithermal component is $\alpha=0.94$, in agreement with previous determinations. The evaporation peak is located at about 0.8 MeV. In addition, a very small high-energy peak (less than 1% in terms of fluence) is present at about 100 MeV. The uncertainty of the total fluence value (about $\pm 5\%$) includes the uncertainty of the spectrometer calibration (about $\pm 4\%$, mainly due to the uncertainty of the ^{152}Eu calibration source) and the unfolding uncertainties (about $\pm 3\%$). The latter comes from the propagation of the uncertainties on the input data (counting + response matrix uncertainties) over the unfolding procedure.

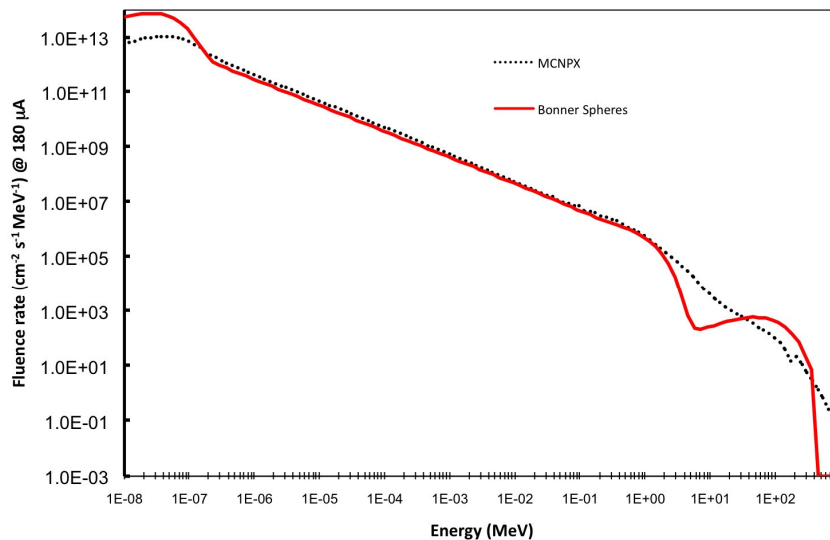


Figure 2: Energy distribution measurement of the neutron fluence rate on VESUVIO normalized to 180 μA proton current (red continuous line), and MCNPX calculation (black dotted line) [9].

The measurements with the diamond detector were done by collecting neutron time of flight spectra (TOF) using a fast (1 ns response time) preamplifier of DBA III type and recording spectra with a fast digital scope from Textronix (2.5 GHz band width and 50 GHz sampling rate). Figure 3 shows the neutron TOF spectrum recorded with the diamond placed at a distance of 11.4 m from the moderator, for a integrated proton current of 2100 μAh .

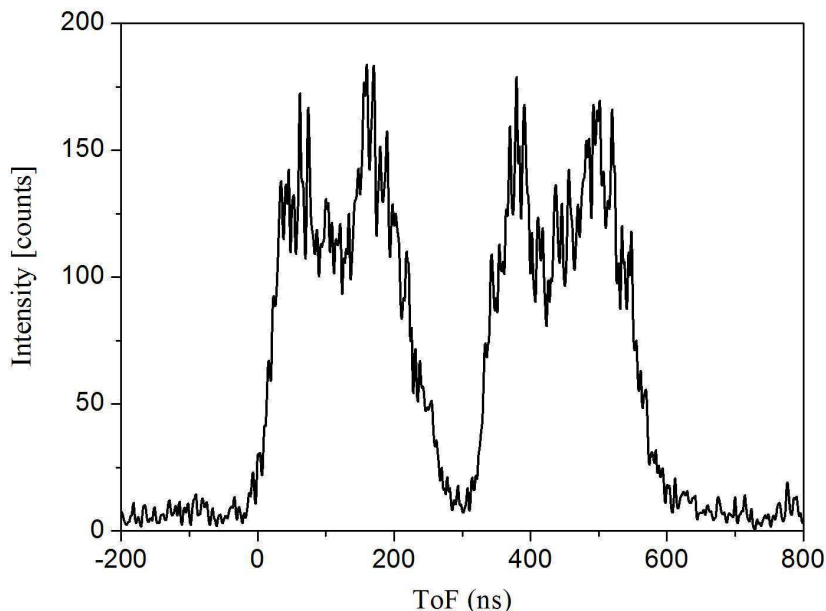


Figure 3: Neutron time of flight spectrum recorded by a single crystal diamond (70 μm thickness) placed into the direct VESUVIO neutron beam at a distance of 11.4 m from the 300 K water moderator

A double structure spectrum can be observed featuring a time gap of about 320 ns that reflects the time structure of the ISIS proton pulse. Each structure of the spectrum has a Full Width at Half Maximum of about 210 ns. Moreover, two time distributions can be observed within each structure of the spectrum with peaks at $t = 62$ ns and 161 ns, the other two being found with about 320 ns delay. A reasonable interpretation could be that the first time distribution peaked at 61 ns and 380 ns are neutrons above 30-40 MeV, while the region around the peaks at 161 ns and 480 ns are neutrons below that energy. This is an effect due to the convolution of the neutron spectrum and n - ^{12}C cross section (mostly the inelastic one) shape. In order to have more precise information about the neutron energy measured by the diamond, biparametric (TOF vs Pulse Height) are going to be analyzed that were collected on the Rotax beam line at ISIS with different electronics set up.

3. Conclusions

An R&D activity is ongoing related to the design of the ChipIr beam line, the ISIS dedicated instrument for chip irradiation. In order to assess the robustness of an electronic

device to Single Event Effects, the fluence onto the irradiated chip is to be determined (assuming an atmospheric like neutron spectrum), preferably close to the irradiation area. Two different detection techniques have been reported: 1) the Bonner Sphere spectrometer technique, that makes use of moderator-based detectors capable to extend neutron fluence measurements up to 800 MeV. A comparison with MCNPX simulations provides an assessment of the potential of this technique to characterize the beam line neutron field. The test results obtained on VESUVIO using a single crystal diamond of 70 μm thickness connected to a fast preamplifier allow for an identification and separation of the contributions of neutrons generated in the double bunch structure provided by the ISIS synchrotron. Despite explorative, these tests clearly show that the single crystal diamonds can be used to assess the spatial uniformity of a neutron beam on the scale of a few mm^2 (4-5 mm^2), a key feature in multiboards test on the ChipIr beam line. In the near future, the analysis of the biparametric data collected on the Rotax beam line and the investigation of the response function of the diamond detectors under irradiation of almost monochromatic neutrons will open the way to the use of these devices as fluence and spectrum monitors as well.

Acknowledgements

This work was supported within the CNR-STFC Agreement concerning collaboration in scientific research at the spallation neutron source ISIS. The financial support of the Consiglio Nazionale delle Ricerche in this research is hereby acknowledged. The CNISM-CNR joint research program is also greatly acknowledged.

References

- [1] J. F. Ziegler and W. A. Lanford, *J. Appl. Phys.* **52**, (1981) 4305; E. Normand, *IEEE Trans. Nucl. Sci.* **43**, (1996) 2742.
- [2] T. J. O’Gorman, J. M. Ross, A. H. Taber, J. F. Ziegler, H. P. Muhlfield, I. C. J. Montrose, H. W. Curtis, and J.L. Walsh, *IBM J. Res. Dev.* **40**, (1996) 3.
- [3] R. C. Baumann, *IEEE Trans. Device Mater. Reliab.* **1**, (2001) 17.
- [4] A. Lesea, S. Drimer, J. J. Fabula, C. Carmichael, and P. Alfke, *IEEE Trans. Device Mater. Reliab.* **5**, (2005) 317.
- [5] <http://lansce.lanl.gov>.
- [6] <http://www.triumf.ca/welcome/index.html>.
- [7] S. P. Platt, Z. Török, *IEEE Trans Nucl Sci* **54** (4), (2007)
- [8] C. Anderani et al. *Appl. Phys. Lett.* **92**, (2008) 114101.
- [9] R. Bedogni et al. *Nucl. Instr. Meth. A* **612**, (2009) 143.
- [10] M. Marinelli, E. Milani, G. Prestopino, A. Tucciarone, C. Verona, G. Verona-Rinati, M. Angelone, D. Lattanzi, M. Pillon, R. Rosa, E. Santoro, *Appl. Phys. Lett.* **90**, (2007) 183509.
- [11] M.D. Lattanzi, M. Angelone, M. Pillon, S. Almaviva, M. Marinelli, E. Milani, G. Prestopino, A. Tucciarone, C. Verona, G. Verona-Rinati, S. Popovichev, R.M. Monterealid, M.A. Vincenti, A. Murari, *JET-EFDA, Culham Science. Fus. Eng. Des.* **84**, (2009) 1156.

ICANS XIX,
19th meeting on Collaboration of Advanced Neutron Sources
March 8 – 12, 2010
Grindelwald, Switzerland

- [12] M. Pillon, M. Angelone, G. Aielli, S. Almaviva, Marco Marinelli, E. Milani, G. Prestopino, A. Tucciarone, C. Verona, G. Verona-Rinati, *J. Appl. Phys.* **104**, (2008) 054513.
- [13] D.J. Thomas, D.J.. *Radiat. Prot. Dosim.* **110 (1-4)**, (2004) 141.
- [14] R. L. Bramblett, R.I. Ewing, T.W. and Bonner., *Nucl. Instr. Meth.* **9**, (1960) 1.
- [15] R. Bedogni, In Proceedings International Workshop on Uncertainty assessment in computation dosimetry – A comparison of approaches. Bologna, Italy, October 8-10, 2007. ISBN 978-3-9805741-9-8.
- [16] M. Violante, L. Sterpone, A. Manuzzato, S. Gerardin, P. Rech, M. Bagatin, A. Paccagnella, C. Andreani, G. Gorini, A. Pietropaolo, G. Cardarilli, S. Pontarelli, C. Frost, *IEEE, Trans. Nucl. Sci.*, **54 (4)**, (2007) 1184.
- [17] R. Bedogni, A. Esposito, M. Chiti., *Radiat. Meas.* **43**, 1113 (2008).
- [18] V. Vylet, J.C. Liu, S.H. Rokni, L.-X. Thai, L.-X.,.. *Radiat. Prot. Dosim.* **70(1-4)**, (1997) 425.
- [19] R. Bedogni, A. Esposito, M. Chiti, M. Angelone, *Radiat. Prot. Dosim.* **126**, (2007) 541.
- [20] B. Wiegel, S. Agosteo, R. Bedogni, M. Caresana, A. Esposito, G. Fehrenbacher, M. Ferrarini, E. Hohmann, C. Hranitzky, A. Kasper, S. Khurana, V. Mares, M. Reginatto, S. Rollet, W. Rühm, D. Schardt, M. Silari, G. Simmer, E. Weitzenegger, *Radiat. Meas.*, in press (2009), B. Wiegel, A V. Alevra., *Nucl. Instr. and Meth. A* **476**, (2002) 36.
- [21] P. Goldhagen, M. Reginatto, T. Kniss, J.W. Wilson, R.C. Singleterry, I.W. Jones, W. Van Steveninck., *Nucl. Instr. and Meth. A* **476**, (2002) 42; R. Bedogni, C. Domingo, A. Esposito, F. Fernández, F., *Nucl. Instr. and Meth. A* **580**, (2007) 1301.

Paper II

Single-crystal diamond detector for time-resolved measurements of a pulsed fast-neutron beam

A. PIETROPAOLO^{1(a)}, C. ANDREANI², M. REBAI³, L. GIACOMELLI³, G. GORINI³, E. PERELLI CIPPO³, M. TARDOCCHI⁴, A. FAZZI⁵, G. VERONA RINATI⁶, C. VERONA⁶, M. MARINELLI⁶, E. MILANI⁶, C. D. FROST⁷ and E. M. SCHOONEVELD⁷

¹ CNISM UdR Tor Vergata - Roma, Italy, EU

² Università degli Studi di Roma Tor Vergata, Dipartimento di Fisica and Centro NAST - Roma, Italy, EU

³ CNISM and Dipartimento di Fisica, Università degli Studi di Milano-Bicocca - Milano, Italy, EU

⁴ Istituto di Fisica del Plasma, CNR - Milano, Italy, EU

⁵ Energy Department, Politecnico di Milano - Milano, Italy, EU

⁶ Dipartimento di Ingegneria Meccanica, Università degli Studi di Roma Tor Vergata - Roma, Italy, EU

⁷ ISIS facility, Rutherford Appleton Laboratory - Chilton, UK, EU

received on 15 September 2010; accepted by R. Voss on 29 November 2010

published online 17 January 2011

PACS 89.20.Bb – Industrial and technological research and development

PACS 29.25.Dz – Neutron sources

PACS 29.30.Hs – Neutron spectroscopy

Abstract – A fast-neutron detector for time-resolved beam measurements at spallation neutron sources is presented. The device features a *p*-type/intrinsic/metal Schottky barrier structure where the active (intrinsic) detection layer is a 150 μm thick single-crystal diamond obtained by chemical-vapour deposition. Coupling to fast front-end electronics preserves the excellent timing properties of the device as demonstrated in tests performed at the ISIS spallation neutron source in UK. The device represents a novel approach in the field of pulsed fast-neutrons spectroscopic techniques. It will find immediate application in localized (mm resolution) fast-neutron fluence measurements required by neutron irradiation experiments at ISIS also envisaging its use for spectrum measurements.



Copyright © EPLA, 2010

Single-Events Effects (SEE) are a concern in areas ranging from avionics to automotive, medical and information technology [1]. SEEs occur when a high-energy neutron (say $E_n > 1 \text{ MeV}$) strikes the sensitive region of an electronic chip, disrupting its correct operation [2–4]. The sensitivity of a chip to SEE is measured by the so-called SEE cross-section, *i.e.* the ratio of the number of SEEs of a given type (*e.g.* Single and/or Multiple Bit Upset) to the neutron fluence onto the chip. Pioneering SEE measurements were done using atmospheric neutrons and several months of data recording due to the low intensity [5,6]. Spallation neutron sources provide a neutron spectrum that resembles the atmospheric spectrum but with enhanced intensities (by a factor $\approx 10^5$ – 10^6), allowing for accelerated testing. Recently a chip irradiation program was launched at the ISIS spallation neutron source [4,7] that will lead to the construction of a dedicated beamline.

Detectors providing intensity and energy spectrum with mm spatial resolution are required to monitor the neutron irradiation at the chip. In this letter we report the first results achieved with a Single-crystal Diamond Detector (SDD) specifically developed for use at a pulsed spallation neutron source. This represents a potential novel approach in the field of fast-neutron detection techniques at these facilities that typically are characterised by the use of large-area (*i.e.* several cm^2) detectors [8]. Diamond is an ideal detector material for the application at hand. Its radiation hardness, low voltage and room temperature operation make it practical in a neutron environment [9]. It is essentially insensitive to γ -rays and visible light, while featuring a relatively large neutron cross-section above $\approx 6 \text{ MeV}$ [10].

The diamonds used in these measurements are grown as small-size single crystals (few mm^2 effective area and sub-mm thickness) by microwave chemical-vapour deposition [11–13]. The SDD structure acts as a

^(a)E-mail: antonino.pietropao1o@roma2.infn.it

p-type/intrinsic/metal Schottky barrier diode. Provided the diamond quality is sufficiently good to minimize recombination and trapping, the effective charge carrier lifetime (τ) is longer than the charge drift time τ_{drift} across the detector given by

$$\tau_{\text{drift}} = \frac{D}{\mu_0 E_D} \left(1 + \frac{\mu_0 E_D}{v_{\text{sat}}} \right). \quad (1)$$

Here D is the depletion layer depth, μ_0 is the electron mobility and v_{sat} is the saturation velocity. Considering that the detector operates in full depletion mode and using the values $D = 150 \mu\text{m}$, $\mu_0 = 2200 \text{ cm}^2 \text{ V}^{-1} \text{ s}^{-1}$, $E_D = 10^4 \text{ V m}^{-1}$ (drift field) and $v_{\text{sat}} = 1.35 \cdot 10^7 \text{ cm s}^{-1}$ [14], eq. (1) gives $\tau_{\text{drift}} \approx 1.5 \text{ ns}$. This short time allows for the use of fast front-end electronics to achieve ns time resolution. For the present measurements a DBA-III (Diamond Broadband Amplifier) was used with response time $\tau = 1 \text{ ns}$ [15], coupled to a digital scope (2.3 GHz bandwidth and 50 GHz sampling rate). The timing properties of SDD + DBA III ($\approx 2.5 \text{ ns}$ FWHM and $< 1 \text{ ns}$ rise time pulses) are quite satisfactory for accurate time-of-flight measurements (ToF) of fast neutrons over flight path lengths $> 10 \text{ m}$ typical of beamlines at ISIS.

The SDD response to fast neutrons is due to neutron interactions in the diamond resulting in the production of charged particles (*e.g.* α -particles). In the neutron energy range up to 20 MeV the main reactions are $^{12}\text{C}(n,\alpha)^9\text{Be}$ and $^{12}\text{C}(n,n)3\alpha$ [9], featuring cross-section values up to a few hundred mb above the threshold energy of 5.71 MeV (fig. 1(a)). The event rate upon detector irradiation with neutrons depends on the local neutron intensity and spectrum. The neutron spectrum available at existing ISIS beamlines is somewhat softer [8] than the atmospheric one, *i.e.* with a weaker relative intensity in the energy range above 100 MeV. This does not prevent the demonstration of the SDD potential for neutron ToF measurements. To this end the SDD was placed in the ROTAX test beamline at ISIS and exposed to a neutron beam from a solid ($T = 95 \text{ K}$) methane moderator at a flight distance of 15.5 m from the main detection position. The neutron spectrum from the moderator is known to fall off roughly as $\approx 1/E_n$ for $E_n > 1 \text{ MeV}$. A second moderator (12 cm water + 6 cm polyethylene slabs) was inserted along the beamline to provide a different neutron energy spectrum at a second detection position located at a flight distance of 16.0 m. The moderator thickness was chosen to attenuate significantly the neutron spectrum below 10 MeV according to attenuation length estimates confirmed by MCNPX simulations [16]. ToF data collected with the SDD at both detection positions are shown in fig. 2(a). All times are relative to the time when the protons hit the ISIS target; *e.g.* the photon flight time is about 50 ns at the two measurement positions. The absence of events at the photon ToF shows the insensitivity of the device to γ -rays from target, an important feature for a reliable neutron detector. The ToF spectrum features a double

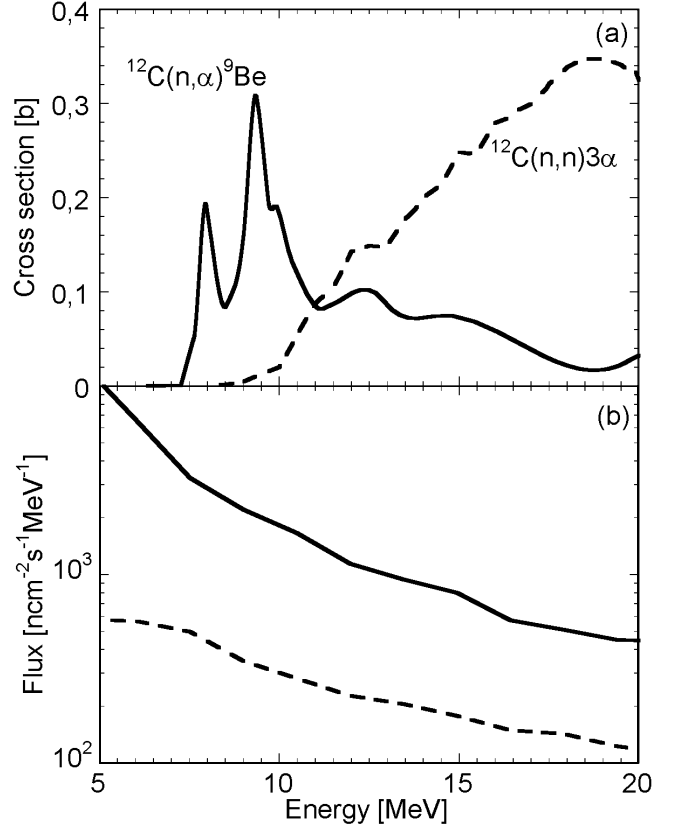


Fig. 1: (a) Cross-section values for the reactions $^{12}\text{C}(n,\alpha)$ and $^{12}\text{C}(n,n)3\alpha$ in the neutron energy range up to 20 MeV. Data from ref. [9]. (b) Neutron spectra before (solid line) and after (dashed line) the moderator simulated with the MCNPX code.

hump shape, due to the ISIS proton beam time structure (fig. 2(b)): two bunches 324 ns apart and 68 ns wide (FWHM), which may be somehow underestimated since it is derived from a beam monitor in the extracted proton beam leading to the target.

Our detector should be able to measure the additional time spread in the neutron ToF spectrum, relative to the intrinsic proton time spread. The SDD data are indeed broader, each hump having a FWHM of about 200 ns at the first detection position and 110 ns at the second position. The two humps are well separated which is due to the insensitivity of the detector to neutrons with $E_n < 6 \text{ MeV}$ (*i.e.* ToF values above $\sim 450 \text{ ns}$). The second moderator is seen to have the expected effect on the neutron ToF: the spectrum is almost unaffected up to 250 ns corresponding to $E_n \approx 20 \text{ MeV}$. At longer flight times substantial neutron attenuation is observed. A quantitative analysis of the spectra collected at the two positions is beyond the scope of the present work. It would require an accurate knowledge of the proton time spectrum of fig. 2(b) which is an accelerator property still under investigation.

The MCNPX code was used to generate a neutron energy spectrum at the two detection positions as shown in fig. 1(b). The resulting ToF spectra can be reconstructed

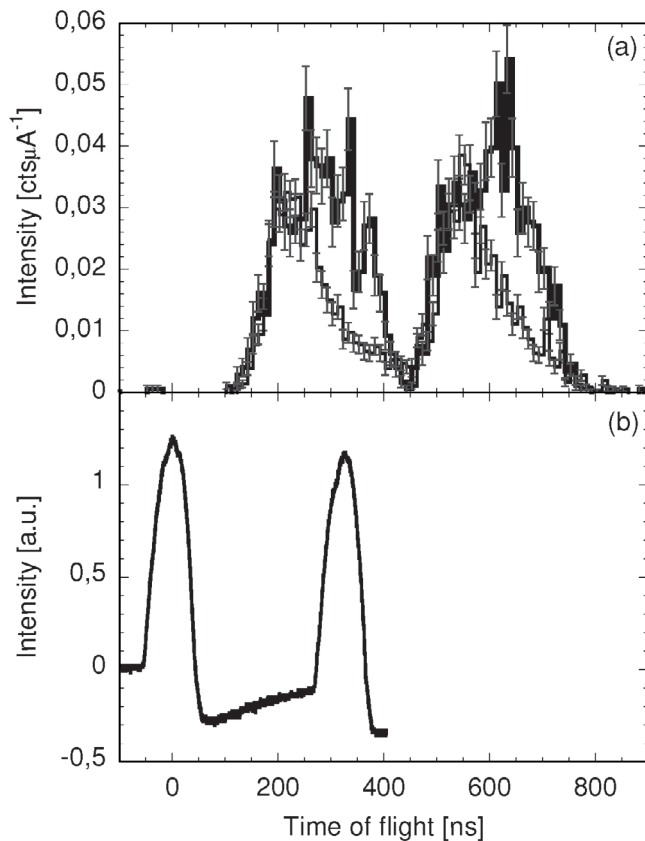


Fig. 2: (a) ToF spectra measured with the SDD at the two detection positions before (thick line) and after (thin line) the moderator described in the text. The data are normalized to the integrated proton current of the two runs which was $I_p = 1761 \mu\text{Ah}$ and $I_p = 3598 \mu\text{Ah}$. for the thick- and thin-line spectra, respectively. Statistical error bars are shown. (b) Time structure of the ISIS proton beam measured with a plastic scintillator placed in the proton beam.

from the cross-sections and neutron fluxes up to 20 MeV (fig. 1), and the energy-ToF Jacobian transformation function. Convolution with a Gaussian function with 68 ns FWHM was also applied to simulate the proton bunch broadening. In fig. 3 the experimental (histogram lines) and simulated (full lines) ToF spectra are shown for the two positions (thick and thin lines, respectively). The relative amplitudes coming out of the MCNPX simulations were not adjusted. The slight overestimation of the low-energy part of the spectrum measured in the first position can be accounted for by a pulse height acquisition threshold effect. Although the precise values threshold settings were not recorded in this experiment, the dashed line in fig. 3 shows the effect of a 3 MeV threshold (actually used in previous experiments), resulting in a ≈ 25 ns shift of the spectrum which improves the agreement between simulated and measured ToF spectra at long flight times. The agreement is not perfect but is satisfactory for the purposes of the present investigation. It suggests that the main features of the SDD response are understood in sufficient detail.

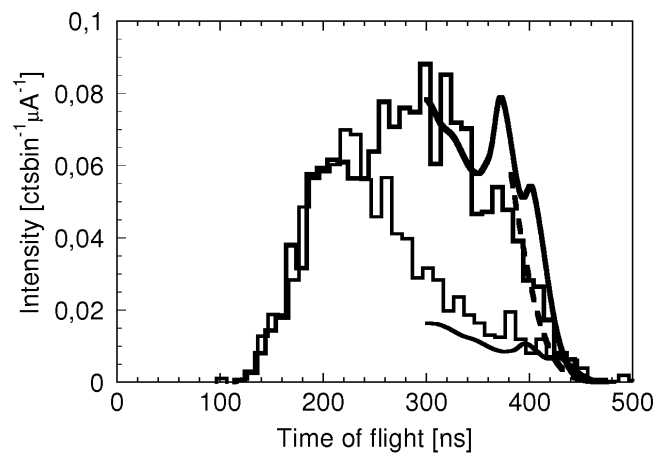


Fig. 3: Time-of-flight spectra measured before (thick histogram line) and after (thin histogram line) the 18 cm thick water + plastic moderator used in the measurements: in order to enhance statistics the two bunches of fig. 2(a) were added up. The continuous lines represent simulated ToF spectra where use was made of the data in fig. 1. The dashed line shows the effect of a 3 MeV pulse height threshold applied to the simulation before the moderator.

The SDD represents a novel approach in the field of fast pulsed neutrons spectroscopic techniques. It has the potential for providing localized neutron fluence and, possibly, neutron energy spectrum measurements at the ISIS pulsed neutron source. The SDD timing properties are quite adequate for neutron time-of-flight measurements. The SDD compact size makes it a promising detector for localized neutron beam monitoring on the mm scale, as required by chip irradiation experiments.

This work was supported within the CNR-CCLRC Agreement No. 01/9001 concerning collaboration in scientific research at the spallation neutron source ISIS. The financial support of the Consiglio Nazionale delle Ricerche in this research is hereby acknowledged. One of the authors (AP) greatly acknowledges the CNISM-CNR joint research program.

REFERENCES

- [1] ZEIGLER J. F. and LANFORD W. A., *J. Appl. Phys.*, **52** (1981) 4305.
- [2] NORMAND E., *IEEE Trans. Nucl. Sci.*, **43** (1996) 2742.
- [3] DODD P. E., SHANEYFELT M. R., SCHWANK J. R. and HASH G. L., in *Proceedings of the International Electron Device Meeting, 2002*, pp. 333–336.
- [4] VIOLANTE M., STERPONE L., MANUZZATO A., GERARDIN S., RECH P., BAGATIN M., PACCAGNELLA A., ANDREANI C., PIETROPAOLO A., CARDARILLI G., PONTARELLI S. and FROST C., *IEEE Trans. Nucl. Sci.*, **54** (2007) 1184.

- [5] BINDER D., SMITH E. C. and HOLMAN A. B., *IEEE Trans. Nucl. Sci.*, **22** (1975) 2675.
- [6] GUENZER C. S., WOLICKI E. A. and ALLAS R. G., *IEEE Trans. Nucl. Sci.*, **26** (1979) 5048.
- [7] ANDREANI C., PIETROPAOLO A., SALSANO A., GORINI G., TARDOCCHI M., PACCAGNELLA A., GERARDIN S., FROST C. D., ANSELL S. and PLATT S. P., *Appl. Phys. Lett.*, **92** (2008) 114101.
- [8] BEDOGNI R., ESPOSITO A., ANDREANI C., SENESI R., DEPASCALE M. P., PICOZZA P., PIETROPAOLO A., GORINI G., FROST C. D. and ANSELL S., *Nucl. Instrum. Methods A*, **612** (2009) 143.
- [9] LATTANZI M. D., ANGELONE M., PILLON M., ALMAVIVA S., MARINELLI M., MILANI E., PRESTOPINO G., TUCCIARONE A., VERONA C., VERONA-RINATI G., POPOVICHEV S., MONTEREALID R. M., VINCENTI M. A., MURARI A. and JET-EFDA CONTRIBUTORS, *Fusion Eng. Des.*, **84** (2009) 1156.
- [10] <http://www-nds.iaea.org/exfor/exfor.htm>.
- [11] MARINELLI M., MILANI E., PAOLETTI A., TUCCIARONE A., VERONA RINATI G., ANGELONE M. and PILLON M., *Appl. Phys. Lett.*, **75** (1999) 3216.
- [12] MARINELLI M., MILANI E., PAOLETTI A., TUCCIARONE A., VERONA RINATI G., ANGELONE M. and PILLON M., *J. Appl. Phys.*, **89** (2001) 1430.
- [13] ALMAVIVA S., MARCO MARINELLI, MILANI E., PRESTOPINO G., TUCCIARONE A., VERONA C., VERONA-RINATI G., ANGELONE M., PILLON M., DOLB-NYA I., SAWHNEY K. and TARTONI N., *J. Appl. Phys.*, **107** (2010) 014511.
- [14] GKOUHAS S., LOHSTROH A. and SELLIN P. J., *Diam. Relat. Matter*, **18** (2009) 1338.
- [15] MORITZ P., BERDERMANN E., BLASCHE K., STELZER H. and VOSS B., *Diam. Relat. Matter*, **10** (2001) 1765.
- [16] <https://mcnpx.lanl.gov/>.

Paper III



Fission diamond detector tests at the ISIS spallation neutron source

M. Rebai^{a*}, C. Andreani^b, A. Fazzi^c, C.D. Frost^d, L. Giacomelli^a, G. Gorini^a, E. Milani^e, E. Perelli Cippo^a, A. Pietropaolo^b, G. Prestopino^e, E. Schooneveld^d, M. Tardocchi^a, C. Verona^e and G. Verona Rinati^e

^aCNISM, Dipartimento di Fisica, Università degli Studi di Milano-Bicocca, and Istituto di Fisica del Plasma, Associazione EURATOM-ENEA-CNR, Milano, Italy

^bDipartimento di Fisica, Centro NAST and CNISM, Università degli Studi di Roma Tor Vergata, Via della Ricerca Scientifica 1, 00133 Roma, Italy

^cEnergy Department, Politecnico di Milano, Via Lambruschini 4, 20156 Milano, Italy

^dSTFC, ISIS facility, Rutherford Appleton Laboratory, Chilton Didcot Oxfordshire, OX11 0QX, United Kingdom

^eDipartimento di Ingegneria Meccanica, Università degli Studi di Roma Tor Vergata, Via del Politecnico 1, 00133 Roma, Italy

A compact device for monitoring of fast neutron fluxes is presented. The device is based on single crystal diamond obtained by the Chemical Vapor Deposition technique coupled to a uranium converter foil where neutron interaction results in emission of charged particles detected inside the diamond. Thermal and fast neutrons are detected using natural uranium containing both ^{235}U and ^{238}U . Biparametric (pulse height and time of flight) data collection was used at the ISIS pulsed neutron source to distinguish events from ^{235}U , ^{238}U and from carbon break-up reactions inside the diamond.

The interaction of high energy cosmic rays with the earth's atmosphere generates a flux of secondary particles including high energy neutrons [1]. Single Event Upsets (SEU) can occur when a high energy neutron, interacting in the sensitive region of an electronic device, disrupts its correct operation [2]. Spallation neutron sources can provide a neutron energy spectrum similar to the atmospheric one, with much higher fluxes for accelerated neutron testing. A new beamline named CHIPIR for SEU studies will be constructed at the ISIS spallation neutron source [3] where experience on neutron irradiation testing is growing [4,5] and new concepts for fast neutron beam monitors are being tested [6]. One line of devel-

opment is the monitoring of the neutron flux on the electronic board or chip which requires compact detectors. Diamond detectors are suitable candidates [7]. They are normally used as Single-crystal Diamond Detectors [8] in which case neutron detection takes place via carbon break-up reactions in the diamond itself. In this paper a composite detector called Fission Diamond Detector (FDD) is presented where a thin ($25\ \mu\text{m}$ thick and $4\ \text{mm}^2$) natural uranium foil is placed in front of a diamond detector grown by microwave-assisted chemical vapour deposition [9,10]. Heavy fragments from neutron induced fission in uranium deposit a large amount of energy (tens of MeV) in the diamond. Fission events are thus recorded together with intrinsic events due to $^{12}\text{C}(n,\alpha)^9\text{Be}$ and $^{12}\text{C}(n,3\alpha)n$ and $^{12}\text{C}(n,n)^{12}\text{C}$ reactions in the diamond. Fission events due to fast neutrons can be separated from other detection events, making

*This work was supported within the CNR-CCLRC Agreement No.01/9001 concerning collaboration in scientific research at the spallation neutron source ISIS. The financial support of the Consiglio Nazionale delle Ricerche in this research is hereby acknowledged.

the FDD a candidate fast neutron flux monitor in CHIPIR.

The neutron production at ISIS relies upon spallation reactions induced by 800-MeV proton bunches accelerated through a synchrotron [11]. Protons are extracted into two bunches (about 320 ns apart) and delivered to a Tungsten-Tantalum target. The extraction frequency is either 10 or 50 Hz and the time-average current is about 200 $\mu\text{A}/\text{h}$. The ROTAX beamline used in the present tests, has a methane moderator at 95 K providing a fast neutron spectrum scaling roughly as $1/E_n$. The FDD was placed at a distance of 15.5 m from the moderator and the diamond bias voltage was 30 V. The natural uranium foil was placed in front of the aluminum contact at a distance of 2 mm leaving a small air gap to ensure insulation without preventing fission fragments from reaching the diamond volume.

The electronic signal chain consisted of a custom made charge preamplifier (integration time of 500 ns), a Timing Filter Amplifier and a N1728 CAEN Waveform Digitizer [12]. Data were collected in biparametric mode, where pulse height and time of each detection event are stored. The CAEN firmware implements a trapezoidal filter [13] to determine the pulse height. Neutron time of flight is determined off line with reference to a proton pulse logic signal which is also stored at every ISIS pulse.

Data were collected for 24 hours, for an integrated proton current of 3578 $\mu\text{A}/\text{h}$.

The data recorded by the FDD detector are shown in figure 1 as a scatter plot. On the vertical axis the pulse height is shown in terms of E_d , the equivalent energy deposited in the detector. On the horizontal axis the time of flight, t_{ToF} , is plotted.

The recorded events can be divided in three areas as shown in the diagram.

- i. Flight times in excess of 1500 ns are associated with neutrons well below the U^{238} fission threshold. These events are due to ^{235}U fission or to α -particles from uranium decay.
- ii. Events with $E_d > 20$ MeV and $t_{\text{ToF}} < 1500$ ns must be associated with heavy fission frag-

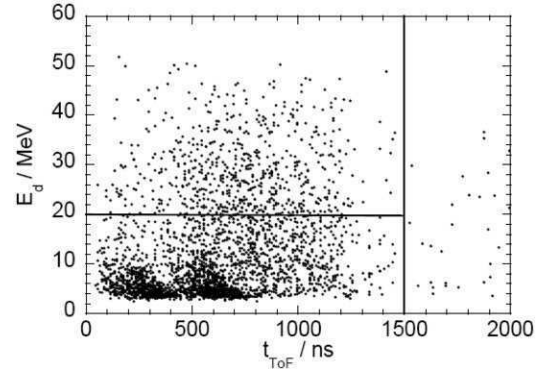


Figure 1. Biparametric (pulse height E_d and time of flight t_{ToF}) scatter plot of data recorded with the FDD detector in the ROTAX neutron beam line at ISIS.

ments from the uranium foil since deposited energies $E_d > 20$ MeV are not observed when the uranium foil is removed from the FDD [8]. The contribution of ^{235}U fission is comparatively low and can be estimated from the event rate measured above 1500 ns; it is thus reasonable to assume that ^{238}U fission by fast neutrons is responsible for the events with $E_d > 20$ MeV and $t_{\text{ToF}} < 1500$ ns.

- iii. At deposited energies $E_d < 20$ MeV and flight times $t_{\text{ToF}} < 800$ ns the dominant reaction mechanism is carbon break-up in diamond, see [8].

The ToF spectrum derived from the data of figure 1 with $E_d > 20$ MeV is shown in figure 2. The TOF spectral shape is significantly different from the one obtained integrating events of $E_d < 20$ MeV [8]. This is due to the dominant contribution of neutrons in the energy range 1 MeV–5 MeV which are detected through the induced fission reactions in ^{238}U since they are below the threshold for reactions with ^{12}C . In order to understand the spectrum in more detail a model calculation can be made. For a pulsed neutron source where all neutrons leave the moderator simultaneously the number of recorded events per unit t_{ToF} can be written as:

$$N(t_{\text{ToF}}) = K \cdot \sigma(E) \cdot \phi(E) \cdot \frac{dE}{dt_{\text{ToF}}} \quad (1)$$

where K is a proportionality constant, σ is the ^{238}U fission cross section, ϕ is the neutron flux

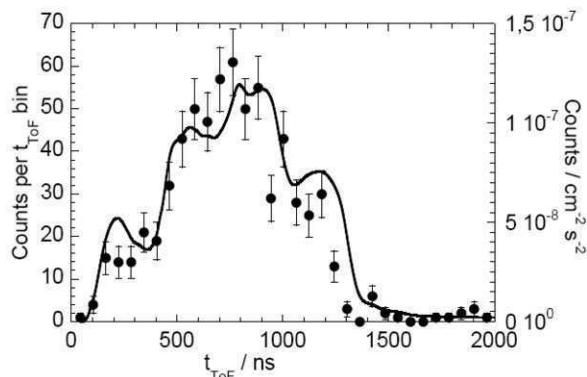


Figure 2. ToF spectrum derived from the data of figure 1 with $E_d > 20$ MeV. Also shown is a simulated t_{ToF} spectrum (see text). The error bars are statistical.

per unit neutron energy (e.g. in units of $\text{cm}^{-2} \text{s}^{-1} \text{MeV}^{-1}$) on the uranium foil and dE/dt_{ToF} is the Jacobian of the energy- t_{ToF} transformation.

In our case the time structure of the fast neutrons leaving the moderator can be described by the measured proton pulse structure, i.e. two Gaussian bunches 320 ns apart. The line in figure 2 is the result of the convolution of the proton pulse structure with the result of Eq. 1 where a reference MCNPX [14] neutron spectrum for the ROTAX beam line was used. The fission cross section from [15] provides values up to $E_n = 200$ MeV. The agreement between data and simulation after adjustment of the constant K is rather good and confirms the identification of the selected events with ^{238}U fission events with little or no contribution from other processes or other types of radiation. It therefore seems feasible to proceed with the development of an FDD optimized for the CHIPIR application. The absolute efficiency of the FDD is much lower than ordinary fission chambers since it scales with the detector surface. It is also substantially lower than Thin Film Breakdown Counters [16] for the same reason. Otherwise the FDD response should be similar to other uranium-based detectors.

In conclusion, first tests of a Fission Diamond Detector prototype at the ISIS pulsed neutron source show that the FDD concept has the potential to be used as a compact fast neutron monitor in irradiation experiments. Biparametric (pulse

height and time of flight) data collection is essential for a correct separation of events from ^{235}U , ^{238}U and from carbon break-up reactions inside the diamond. The FDD is also sensitive to thermal neutrons, a feature that could also find application in accelerated neutron testing of electronic devices.

REFERENCES

1. J.F. Ziegler et al., IBM J. Res. Devel. 40 no. 1 3-1, Jan. 1996.
2. P.E. Dodd and L.W. Massengill, IEEE Trans. Nucl. Sci. 50 no. 3 583-602 Jun. 2003.
3. <http://www.isis.stfc.ac.uk/instruments/ChipIr>.
4. C. Andreani et al., Appl. Phys. Lett. 92 114101 (2008).
5. M. Violante et al., IEEE Trans. Nucl. Sci. 54 1184 (2007).
6. R. Bedogni et al., Nucl. Inst. and Meth. A 612 (2009) 143-148.
7. D. Lattanzi et al., Fus. Eng. and Des. 84 Issues 7-11 (2009) 1156-1159.
8. L. Giacomelli et al., Nucl. Phys. B Proceeding of IPRD10 (2010).
9. M. Marinelli et al., Appl. Phys. Lett. 75 3216 (1999).
10. M. Marinelli et al., Journ. Appl. Phys. 89 1430 (2001).
11. <http://www.isis.stfc.ac.uk/>.
12. CAEN Nuclear Physics, Technical information manual - MOD. N1728A/B 4 CH 100MHz flash ADC - Manual Revision no. 5, NPO: 00118/04:N1728x.MUTx/05 (2007).
13. V.T. Jordanov, G.F. Knoll, Nucl. Instr. and Meth. A 345 (1994) 337-345.
14. <https://mcnpx.lanl.gov/>.
15. <http://www-nds.iaea.org/exfor/exfor.htm>.
16. A.N. Smirnov et al., Report RAL-TR-2010-024, Rutherford Appleton Laboratory, Chilton (UK) 2010.

Paper IV

Diamond detector for high rate monitors of fast neutrons beams

L.Giacomelli^a, M.Rebai^a, E.Perelli Cippo^a, M.Tardocchi^a, A.Fazzi^b,
C.Andreani^c, A.Pietro Paolo^c, C.D.Frost^d, N.Rhodes^d, E.Schooneveld^d and
G.Gorini^a

^a*Dipartimento di Fisica, Università degli Studi di Milano-Bicocca, and Istituto di Fisica del Plasma,
Associazione EURATOM-ENEA-CNR, Milano, Italy*

^b*Energy Department, Politecnico di Milano, Milano, Italy*

^c*Dipartimento di Fisica, Centro NAST, Università degli Studi di Roma Tor Vergata, Roma, Italy*

^d*STFC, ISIS facility, Rutherford Appleton Laboratory, Chilton Didcot Oxfordshire, United Kingdom*

Abstract. A fast neutron detection system suitable for high rate measurements is presented. The detector is based on a commercial high purity single crystal diamond (SDD) coupled to a fast digital data acquisition system. The detector was tested at the ISIS pulsed spallation neutron source. The SDD event signal was digitized at 1 GHz to reconstruct the deposited energy (pulse amplitude) and neutron arrival time; the event time of flight (ToF) was obtained relative to the recorded proton beam signal t_0 . Fast acquisition is needed since the peak count rate is very high (~800 kHz) due to the pulsed structure of the neutron beam. Measurements at ISIS indicate that three characteristics regions exist in the biparametric spectrum: i) background gamma events of low pulse amplitudes; ii) low pulse amplitude neutron events in the energy range $E_{\text{dep}} = 1.5-7$ MeV ascribed to neutron elastic scattering on ^{12}C ; iii) large pulse amplitude neutron events with $E_n > 7$ MeV ascribed to $^{12}\text{C}(n,\alpha)^9\text{Be}$ and $^{12}\text{C}(n,n')3\alpha$.

Keywords: Fast diamond neutron detector, digitized pulse amplitude and ToF measurements, high-energy neutron beam monitor, neutron-gamma energy discrimination.

PACS: 28.50.Dr; 29.27.Fh; 29.30.Hs; 29.40.Wk; 81.05.ug.

INTRODUCTION

High-energy neutron beams can be used to induce and control the neutron chain reaction in sub-critical fission reactor assembly [1]. The neutron beam has to feature energies > 10 MeV to exploit the neutron fission cross sections of the fuel isotopes and of the fission products. Monitoring the incoming neutron beam is a key factor to control and optimize the fission process as it is in more general neutron beam-target experiments.

Another application where the neutron beam fluence and energy need to be monitored is the irradiation of electronic microchips for accelerated experiments on neutron induced single event effects (SEE) [2]. To this aim a new irradiation beam line with neutron energies up to $E_n \approx 800$ MeV is being built at the ISIS spallation neutron source [3]. The microchip dimensions call for small size fast neutron flux monitors such as a single crystal diamond detector (SDD) recently tested on the ROTAX beam

line at the ISIS facility (UK) [4]. The paper reports on the results of the measurement campaign.

EXPERIMENTAL

At ISIS, neutrons are produced by a double bunch structured proton beam of 800 MeV and $\approx 200 \mu\text{A}$ average current on a Ta-W target delivering about 30 neutrons / proton at 50 Hz repetition frequency. The two proton bunches are ≈ 70 ns wide and ≈ 320 ns apart. The SDD was placed in the direct beam at a distance of 14.2 m from the 95 K methane moderator. The neutron energy (E_n) spectrum features a ~ 10 meV peak and a $1/E_n$ tail in the fast neutron region, resembling the atmospheric neutron flux produced by cosmic rays [5][6]. A beam chopper was used along the beam line to remove the low energy component of the neutron beam. The neutron induced SDD signals are mainly due to neutron elastic scattering and to neutron capture reactions $^{12}\text{C}(n,\alpha)^9\text{Be}$ and $^{12}\text{C}(n,n)3\alpha$ depending on E_n [7]. The capture reactions occur for neutron energies $E_n > 7$ MeV. Only the $^{12}\text{C}(n,\alpha)^9\text{Be}$ reaction allows for the full neutron energy deposition within SDD.

The SDD detector is a commercial chemical vapor deposition high purity single crystal diamond (4.6-4.6 mm² surface and 0.5 mm thickness, Au electrodes) purchased from Diamond Detectors Ltd. [8]. It is connected through a fast preamplifier DBAIII [9] to a multi-channel fast digitizer CAEN DT5751 [10]. The preamplifier output pulses feature rise time < 1 ns and FWHM ≈ 2.5 ns. The fast digitizer is USB-connected to a computer and has communication software for settings the acquisition parameters and for data storage. The voltage bias applied in these experiments was $V_{\text{bias}} = +400$ V. The noise level was $\approx \pm 6$ mV and the signal offset was $\approx +30$ mV. The CAEN module was used to record the SDD signal. The proton beam signal from the accelerator was recorded in a separate channel. Each signal was sampled at 1 GHz as a 6 μs long waveform. The maximum signal peak amplitude is 1 V. The SDD waveform usually contains more than one useful detection event. A Python script [11] was developed in order to analyze the signals of the SDD waveform. The waveforms were corrected for offset; for all pulses exceeding the 30 mV threshold the time of flight (t_{ToF}), peak height, and pulse amplitude Q_T (i.e., the signal area) were determined. The t_{ToF} is calculated as difference between the time of the individual signal peak in the SDD waveform and the time of the corresponding proton beam signal. The event deposited energy E_{dep} is obtained from the pulse amplitude Q_T . Observations on the biparametric (t_{ToF} , E_{dep}) spectrum were performed over a period of about 8 days.

DETECTOR STABILITY

The radiation interacting with the SDD gives rise to electrons and holes, which follow the electric field lines of intensity V_{bias} / d (d being the thickness of the SDD depletion layer), and build up the signal at the electrodes. In a SDD, the electrons generate the signal while reaching the anode at $V_{\text{bias}} = +400$ V. The radiation also gives rise to displacements in the SDD crystal that traps the charge. This induces a

local electric field opposite to the one due to V_{bias} , i.e., the polarization of the diamond. To re-establish the performance, it is necessary to switch the V_{bias} off [12].

The measurement results presented here concern two data sets relative to two acquisitions of 17 h and 94 h. V_{bias} was switched on immediately before the two acquisitions started. FIGURE 1 shows the ISIS proton beam current I_p (left hand axis) and the SDD counts (right axis) due to signals with peak height exceeding 150 mV.

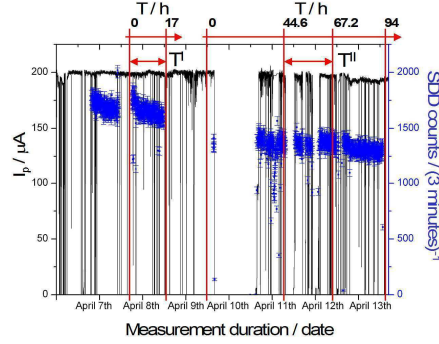


FIGURE 1. ISIS proton beam current I_p (left hand axis) and SDD counts with peak height > 150 mV (right hand axis). Two acquisition periods of 17 h and 94 h are shown on the top together with the two time intervals T^I and T^{II} considered for this study. Each SDD time bin is 3 minute long.

The ISIS proton beam current fluctuations are due to discontinuities in the accelerator operational conditions. The SDD counts decrease with time in the first few hours of operations and are nearly stable afterwards. A possible interpretation of the results would be that, after an initial reduction in sensitivity, the polarization does not affect the SDD performance. However, pulse amplitude and ToF spectra do not feature significant changes associated to the irradiation history (FIGURE 2). This suggests that the observed rate changes may be due to other causes than polarization effects that are presently not understood. Since an irradiation-dependent rate would be an undesirable feature of a beam monitor it will be further investigated in the near future.

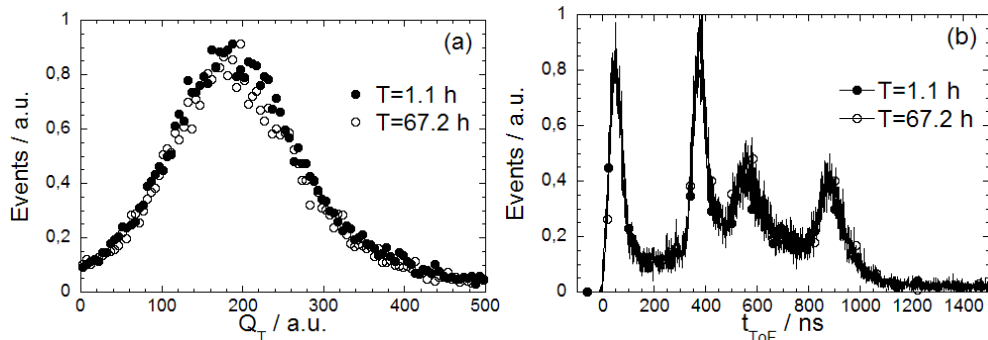


FIGURE 2. Comparison of the normalized pulse amplitude distributions Q_T (a) and of the t_{ToF} spectra (b) at $T = 1.1$ h and at $T = 67.2$ h.

BIPARAMETRIC ANALYSIS

FIGURE 3(a) shows the biparametric (t_{ToF} , E_{dep}) spectrum obtained by adding the data of the two acquisitions periods T^I and T^{II} shown in FIGURE 1 for a total of 114 h. The radiation from a thin foil of natural uranium placed on the detector provided a means to calibrate the energy deposited in the SDD [13][14][15].

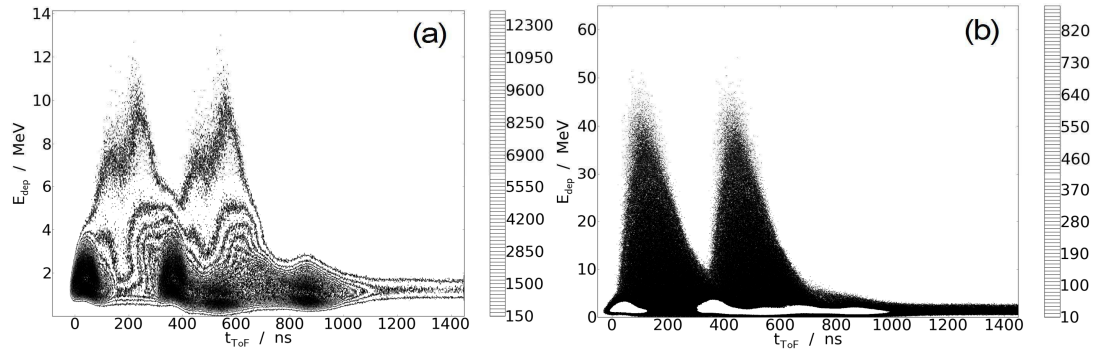


FIGURE 3. Biparametric (t_{ToF} , E_{dep}) contour plot for the 114 h long measurement at the ROTAX beam line (a). The total number of events is $9.1 \cdot 10^7$. (b) same as (a) but with a different grey scale showing the events with high deposited energy.

Different regions are visible in the biparametric spectrum. The peaks at $t_{\text{ToF}} \approx 50$ ns and $t_{\text{ToF}} \approx 370$ ns and $E_{\text{dep}} \approx 1.8$ MeV are interpreted as due to γ rays from the target/moderator assembly. The remaining events are mostly due to elastic and inelastic neutron collisions/reactions with Carbon. Elastic collisions are the main contribution at low deposited energies including the peaks with $t_{\text{ToF}} \approx 550$ ns and $t_{\text{ToF}} \approx 870$ ns and $E_{\text{dep}} \approx 1$ MeV which is associated with the elastic cross section peak at $E_n \approx 3.5$ MeV (see FIGURE 4).

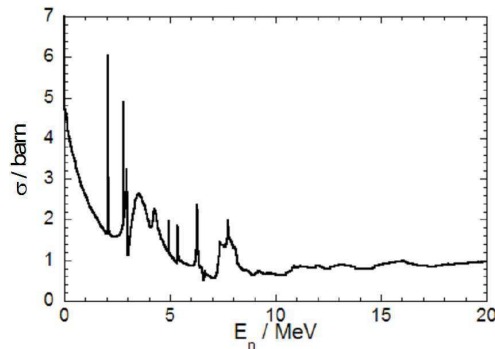


FIGURE 4. Cross section values for neutron elastic scattering on Carbon [7].

The neutron events with $t_{\text{ToF}} > 1000$ ns involve multiple scattering along the beam line collimator before reaching SDD or they are events related to the activation of the detector itself. FIGURE 5 shows the projections of the data in FIGURE 3(a) along the t_{ToF} (a) and E_{dep} (b) axes. In FIGURE 5(a), the double peaks due to prompt γ 's (≈ 70 ns wide) and 3.5 MeV neutrons are clearly recognizable. The log scale energy distribution of the events displayed in FIGURE 5(b) shows events with energy deposition E_{dep} up to 60 MeV. Most of the events have $E_{\text{dep}} < 4$ MeV.

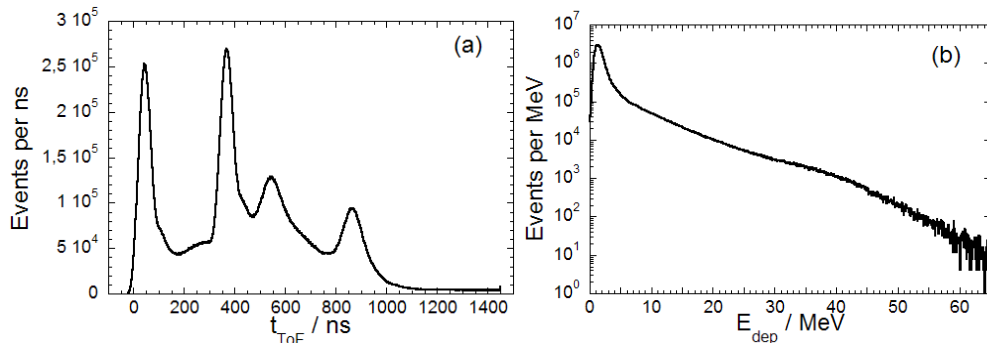


FIGURE 5. t_{ToF} (a) and E_{dep} (b, in log scale) spectra obtained as projection of the biparametric (t_{ToF} , E_{dep}) spectrum of FIGURE 3(a).

CONCLUSIONS

The SDD performance was tested at the ROTAX beam line of the ISIS spallation neutron source. SDD proved capable of detailed measurements of the time structure and energy of the incoming radiation beam. New SDD tests with a mixed (^{239}Pu , ^{241}Am , ^{244}Cm) α source in vacuum and new calculations will be performed to verify these results [13][14][16][17]. New SDD tests are also planned at the VESUVIO beam line at ISIS [18]. The spectroscopic capabilities of the SDD make it an interesting choice as a detector system for neutron experiments where high rate capability is required.

ACKNOWLEDGMENTS

This work was supported within the CNR-CCLRC Agreement No.01/9001 concerning collaboration in scientific research at the spallation neutron source ISIS. The financial support of the Consiglio Nazionale delle Ricerche in this research is hereby acknowledged.

REFERENCES

1. J. Källne *et al.*, contribution to this conference.
2. R.D. Schrimpf and D.M. Fleetwood, <http://www.worldscibooks.com/engineering/5607.html>.
3. <http://www.isis.stfc.ac.uk/instruments/Chipir/>.
4. <http://www.isis.stfc.ac.uk/index.html>.
5. <http://www.jedec.org/standards-documents/docs/jesd-89a>.
6. webstore.iec.ch/preview/infoiec62396-1%7Bed1.0%7Den.pdf.

7. <http://www.nndc.bnl.gov/exfor/endl00.jsp>.
8. Diamond Detector Ltd. BCMS-SCD464650A – BCM.
9. P. Moritz, “Broadband Preamplifiers for Fast Particle Detectors”, GSI - Gesellschaft für Schwerionenforschung mbH, Planckstr. 1, D-64291 Darmstadt, Germany.
10. <http://www.caen.it/csite/CaenProd.jsp?parent=14&idmod=632>.
11. <http://www.python.org/>.
12. M. Angelone *et al.*, “Radiation hardness of a polycrystalline chemical-vapor-deposited diamond detector irradiated with 14 MeV neutrons”, *Rev. Sci. Instrum.* **77**, (2006) 023505. G.J. Schmid *et al.*, “A neutron sensor based on single crystal CVD diamond”, *Nucl. Instr. and Meth. A* **527** (2004) 554-561.
13. A. Pietropaolo *et al.*, “Fission diamond detectors for fast-neutron ToF spectroscopy”, *Europhysics Letters* **94** (2011) 62001.
14. M. Rebai *et al.*, “Fission diamond detector tests at the ISIS spallation neutron source”, *Nuclear Physics B Proceedings Supplements* **215**, Issue 1, (2011) 313-315.
15. <http://physics.nist.gov/PhysRefData/Star/Text/ASTAR.html>.
16. A. Pietropaolo *et al.*, “Single-crystal diamond detector for time-resolved measurements of a pulsed fast-neutron beam”, *Europhysics Letters* **92** (2010) 68003.
17. L. Giacomelli *et al.*, “Diamond detectors for fast neutron irradiation experiments”, *Nuclear Physics B Proceedings Supplements* **215**, Issue 1, (2011) 242-246.
18. <http://www.isis.stfc.ac.uk/instruments/vesuvio/>.

Paper V

A neutron diagnostic for high current deuterium beams^{a)}

M.Rebai^{1b}, M. Cavenago³, G.Croci², M.Dalla Palma³, G.Gervasini², F.Ghezzi², G.Grosso², F.Murtas⁴, R.Pasqualotto³, E.Perelli Cippo¹, M.Tardocchi², M.Tollin³ and G.Gorini^{1,2}

¹ CNISM, Dipartimento di Fisica, Università degli Studi di Milano-Bicocca, Milano, Italy

² Istituto di Fisica del Plasma, Associazione EURATOM-ENEA-CNR, Milano, Italy.

³ Consorzio RFX - Associazione Euratom-Enea sulla Fusione, corso Stati Uniti 4, I-35127 Padova, Italy

⁴ INFN, Laboratori Nazionali di Frascati, Frascati (Roma), Italy.

(Presented XXXXX; received XXXXX; accepted XXXXX; published online XXXXX)

(Dates appearing here are provided by the Editorial Office)

A neutron diagnostic for high current deuterium beams is proposed for installation on the SPIDER test beam facility. The proposed detection system is called Close-contact Neutron Emission Surface Mapping (CNESM). The diagnostic aims at providing the map of the neutron emission on the beam dump surface by placing a detector in close contact, right behind the dump. CNESM uses Gas Electron Multiplier detectors equipped with a cathode that also serves as neutron-proton converter foil. The cathode is made of a thin polythene film and an aluminium film; it is designed for detection of neutrons of energy > 2.2 MeV with an incidence angle $< 45^\circ$. CNESM was designed on the basis of simulations of the different steps from the deuteron beam interaction with the beam dump to the neutron detection in the nGEM. Neutron scattering was simulated with the MCNPX code. CNESM on SPIDER is a first step towards the application of this diagnostic technique to the MITICA beam test facility, where it will be used to resolve the horizontal profile of the beam intensity.

I. INTRODUCTION

SPIDER [1, 2] is a beam test facility to be hosted at the Consorzio RFX site in Padua, Italy, as a first step towards the full scale demonstration of the feasibility of the deuterium beam injectors for the ITER fusion experiment [3]. The main goal of the prototype RF negative ion source SPIDER is to demonstrate the capability of producing a one hour long D^- beam pulse at the current level required by ITER but with a reduced beam energy of up to 100 keV. The 100 keV deuterons will collide against a target (the beam dump) tilted by 30° relative to the beam axis (Figure 1). The SPIDER facility is made of beamlets in a matrix arrangement; the spacing between beamlets at the dump surface is 40×22 mm² and also their footprint is of a similar size. The total beam current of 40 A is spread out over a surface of 1 m² for a reference average current density of 40 A/m² and deuterium flux of 2.5×10^{20} D/m²s. The beam dump is a rectangular panel made of CuCrZr-alloy water-cooled hypervaportrons with an elemental composition of about 99% Cu. The neutron production due to fusion reactions between beam deuterons and deuterons adsorbed in the dump will be a few times 10^{15} neutrons per SPIDER pulse. The neutron source intensity is suitable for diagnostic applications. Here a neutron diagnostic is proposed that is designed to provide the map of the beam intensity with a spatial resolution approaching the size of individual beamlets.

II. CNESM principle

The proposed detection system is called Close-contact Neutron Emission Surface Mapping (CNESM). It is placed right behind the beam dump (Figure 1), as close as possible to the neutron emitting surface.

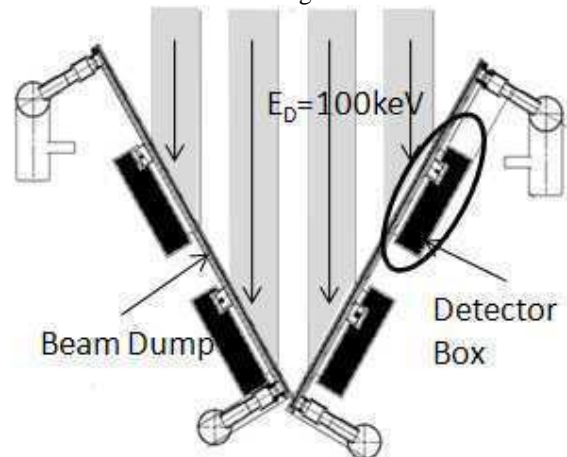


Figure 1: Schematics of the SPIDER beam dump. The beam dump is tilted by 30° relative to the beam axis. The CNESM detectors (black) are placed right behind the beam dump.

The distance between the detection surface and the emitting surface can be as short as $d = 30$ mm; this is crucial in order to provide the map of neutron emission on the beam dump surface with good spatial resolution. The CNESM diagnostics uses nGEM as neutron detectors [4].

^{a)}Contributed paper published as part of the Proceedings of the 14th International Conference on Ion Sources, Giardini-Naxos, Sicily, Italy, September, 2011.

^{b)}marica.rebai@mib.infn.it

These are flat Gas Electron Multiplier (GEM) detectors equipped with a cathode that also serves as neutron-proton converter foil. Each nGEM detector maps the neutron emission from a group of 5x16 beamlets: populating the total beam dump surface would require 16 nGEM detector units. The system is modular meaning that any number of nGEM detectors can be installed. Since the GEM detectors operate at room pressure, they are placed inside a steel containment box connected to the off-vacuum environment outside of the SPIDER vacuum vessel by one pipe containing the electrical cables and the gas pipelets feeding the Ar/CO₂ gas mixture into the nGEM detector. The principle of operation of the nGEM cathode is shown in Figure 2. Incoming neutrons have an energy E_n between 2.45 and 2.85 MeV, depending on the emission angle. They are converted into protons by elastic recoil in a thin polyethylene (CH₂) film. Protons leaving the CH₂ film with enough energy can cross the Al foil and reach the gas. The gas layer is also thin (few mm) compared to the proton range meaning that only a fraction of the proton energy is deposited in the gas and detected.

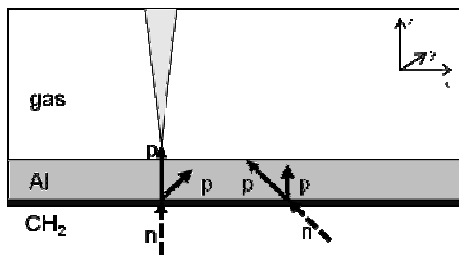


Figure 2 Illustration of how the Al cathode thickness can be used to suppress detection of neutrons with oblique incidence. Neutrons are converted into protons in the polyethylene foil (black). Only one of the four protons in the figure crosses the Al foil (grey) and produces a discharge in the GEM gas.

Since the planar neutron source to be mapped is at some distance from the detection surface, better spatial resolution is achieved if the trajectory of the detected neutrons is not too far from being perpendicular to the cathode surface. Figure 2 illustrates how this is achieved by suitable choice of the Al foil thickness: the 50 μm thick Al foil stops all protons with a recoil angle $\theta_p > 45^\circ$ and/or with a recoil energy $E_p < 2.2$ MeV. Note that the proton recoil energy is $E_p = E_n \cos^2 \theta_p$, where θ_p is the proton recoil angle. This directional response of the nGEM cathode to neutrons is beneficial also for rejecting neutrons reaching the cathode after scattering off the beam dump structure (see below).

The GEM read-out is a simple printed circuit board (PCB): the structure of the readout can be easily adapted to experimental needs, using strips or pads of arbitrary shapes connected to the front-end electronics. The induced signal is fast (10 ns) because it is due to the motion of the electrons in the GEM gas. The maximum effective gain reachable with a single-GEM detector is of the order of 10^3 . Higher gas gain, up to $10^4 - 10^5$, can be achieved assembling more than one GEM foil in cascade at close distance to each other. By increasing the effective gain, GEM detectors can be set to detect lower energy particles

or photons. In general for photons a higher gain (10^4) is required in order to improve the signal/noise ratio. Moreover, the use of a triple GEM allows for splitting of the applied potential, thus reducing the probability of unwanted discharges in the detector. The readout pads will be arranged so as to have two pads (area $20 \times 22 \text{ mm}^2$) per beamlet footprint, for a total of 160 readout channels. Cost-effective readout electronics is available and can indeed manage hundreds of readout channels.

III. MODEL SIMULATIONS

CNESM was designed on the basis of simulations of the different steps, from the deuteron beam interaction with the beam dump to the neutron detection in the nGEM. Deuterium beam interaction was simulated using the TRansport of Ion in Matter (TRIM) program [5]: the trajectories of 10^6 deuterium ions with an initial energy $E_0 = 100$ keV and incidence angle equal to 60° relative to the normal to the CuZrZr-alloy target have been simulated. At least 95% of the deuterons penetrate (by up to 0.8 μm) in the beam dump and can contribute to the neutron emission. The TRIM result was used to determine i) the average deuterium energy and ii) the deuteron deposition rate as function of penetration depth. The latter was used to calculate the (time dependent) deuterium concentration using a so-called Local Mixing Model [6] whereby deuteron migration in the copper alloy is neglected and a local saturation value of 20% [7] is assumed for the deuterium concentration.

The neutron emissivity as a function of penetration depth was then evaluated as $y = \Phi \sigma n_D$, where Φ is the deuterium flux, σ is the energy-dependent $D(d,n)^3\text{He}$ fusion cross section and n_D the implanted deuterium density. A more interesting quantity is the neutron brightness of the source. This is just the line integral of the emissivity over the penetration depth. The brightness reaches a saturation value of about $1.4 \cdot 10^{12} \text{ n/m}^2\text{s}$ 2-3 minutes after the beam is switched on.

The contribution due the anisotropy of the fusion reaction cross section is to peak the neutron emission along the deuteron beam direction and was evaluated analytically. It results in a shift of the neutron field at the detection surface of about 10 mm compared to the ideal case of isotropic neutron emission described before, and can be neglected in the simulations. Other neutron transport effects were investigated using the MCNPX code [8]. The beam dump model used for the simulation is made of two CuCrZn alloy layers and a layer of water in between; the layer thicknesses were chosen in order to reproduce the mass ratio of the cooling water and the copper alloy. About 10% of all neutrons with energy $E_n > 2 \text{ MeV}$ arriving at the nGEM detection surface do so after scattering at least once in the beam dump. Since the direction of scattered neutrons tends to be isotropic they are to a large extent rejected as a result of the directional response of the nGEM cathode. We conclude that neutron transport effects are not expected to perturb the measurement in a significant way.

The energy spectrum deposited in the nGEM gas was also investigated with a MCNP model of the detector. A monoenergetic ($E_n=2.7$ MeV), monodirectional point neutron source was placed at a distance $d=30$ mm from the cathode. The cathode was modelled as a slab composed of a 25 μm thick polyethylene film (CH_2), a 50 μm thick Al foil and a 3 mm GEM gas mixture of Argon (70%) and CO_2 (30%). The resulting energy deposition spectrum is shown in Figure 3 for different neutron incidence angles θ_n . The overall signal intensity drops to almost zero for $\theta_n > 45^\circ$ confirming the directional response of the nGEM cathode to neutrons.

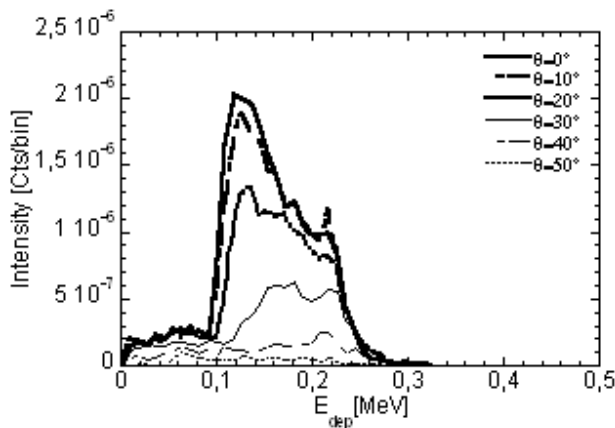


Figure 3: Simulated distribution of proton energy deposited inside the nGEM gas for different neutron incident angles θ_n . The thickness of the Al foil was $t=51$ μm . The intensity is per unit neutron source. The bin width is 10keV.

The energy spectrum rises sharply above $E_d=90$ keV and drops above $E_d=240$ keV. The detailed shape of the distribution within this energy range can be understood by noting that i) the energy loss in the Al foil is a *decreasing* function of the proton energy and ii) the range of the most energetic protons exceeds the GEM gas thickness. The result is that higher energy protons deposit *less* energy in the gas, whereas the maximum deposited energy is achieved by lower energy protons that have a range matching the GEM gas thickness. We can therefore interpret the spectral shape as due to two main components. On the low energy side is a peak due to energetic protons. This component is dominant for lower neutron incidence angles. The second component due to lower energy protons peaks on the high energy side of the distribution. It is dominant for larger incident angles.

The spatial resolution of the measurement is mainly limited by the width (FWHM) of the spatial distribution of recorded events on the nGEM cathode in response to a point neutron source on the beam dump surface. We consider here the width along the X-axis (see Figure 2). A limit case is one of unperturbed propagation of the neutrons from the point source. In this case the intensity at the cathode would have a $1/(x^2+d^2)$ dependence and the FWHM value of about 60 mm would exceed the beamlet dimension (40 mm). The effect of the directional detector response due to the Al foil is to decrease the FWHM value

to about 30 mm. This level of spatial resolution is adequate for unfolding the neutron source intensity from the 2D event map in the nGEM detector.

The CNESM diagnostic is intended for measurement of the neutron emission map. The extent to which the neutron emission map is representative of the deuteron beam intensity distribution on the SPIDER beam dump depends on the deuteron concentration in the dump.

IV. CONCLUSIONS

The proposed CNESM detection system was shown to meet the goal of providing the map of the neutron emission on the beam dump surface. This is achieved by using nGEM detectors equipped with a cathode designed for detection of neutrons of energy $E_n > 2.2$ MeV with an incidence angle $\theta_n < 45^\circ$. CNESM was designed on the basis of simulations of the different steps from the deuteron beam interaction with the beam dump to the neutron detection in the nGEM. We conclude that a CNESM diagnostic based on nGEM detectors will provide beam images with a spatial resolution matching the beamlet footprints and a time resolution < 1 s.

CNESM is a first step towards the application of this diagnostic technique to the MITICA beam test facility, where it will be used to resolve the horizontal profile of the beam intensity. The main difference between SPIDER and MITICA is the x100 larger neutron fluxes expected. This requires a reassessment including further tests of the radiation hardness of the signal readout electronics. The beam energy of 1 MeV and the grazing incidence of the beam with a tilt angle of the beam dump of about 6° are further differences that will require a careful optimization of the detection method.

This work was set up in collaboration and financial support of F4E.

REFERENCES

- [1] P. Sonato et al., this conference.
- [2] R Pasqualotto et al, this conference.
- [3] R. Hemsworth, et al, Nucl.Fusion **49**, (2009).
- [4] B. Esposito, B. Esposito, F. Murtas, R. Villari, M. Angelone, D. Marocco, M. Pillon, S. Puddu, Nucl. Instr. and Meth. A (2009), doi:10.1016/j.nima.2009.06.101
- [5] J.F. Ziegler, SRIM/TRIM code, available online at www.srim.org
- [6] D.K. Brice, B.L. Doyle and W.R. Wampler., J. Nucl. Mater. 111&112 (1982) 598.
- [7] J. Kim, J. Nucl. Technol. 44 (1979) 315.
- [8] <http://mcnp-green.lanl.gov/>

Paper VI

nGEM neutron diagnostic concept for high power deuterium beams

Croci G.^{a,b*}, Rebai M.^c, Claps G.^d, Cavenago M.^e, Dalla Palma M.^f, Gervasini G.^a, Grosso G.^a, Murtas F.^d, Pasqualotto R.^f, Perelli Cippo E.^c, Tardocchi M.^a, Tollin M.^f, and Gorini G.^c.

^a*IFP-CNR, Milano, Italy*

^b*INFN Sez. di Milano-Bicocca, Milano, Italy*

^c*University of Milano-Bicocca, Milano, Italy*

^d*INFN-LNF, Frascati, Italy*

^e*INFN-LNL, Legnaro, Italy*

^f*Consorzio RFX, Associazione EURATOM-ENEA sulla Fusione, Padova, Italy*

E-mail: gabriele.croci@ifp.cnr.it

ABSTRACT: The ITER neutral beam test facility under construction in Padova will host two experimental devices: SPIDER, a 100 kV negative H/D RF source, and MITICA, a full scale, 1 MeV deuterium beam injector. Detection of fusion neutrons will be used as a means to resolve the horizontal beam intensity profile. The neutron detection system will be placed right behind the SPIDER beam dump, as close to the neutron emitting surface as possible thus providing the map of the neutron emission on the beam dump surface. The system uses nGEM neutron detectors. These are Gas Electron Multiplier detectors equipped with a cathode that also serves as neutron-proton converter foil. The cathode is designed to ensure that most of the detected neutrons at a point of the nGEM surface are emitted from the corresponding 40x22 mm² beamlet footprint on the dump front surface. The nGEM readout pads (area 20x22 mm²) will record a useful count rate of 5 kHz providing a time resolution of temporal structures in the neutron fluency rate to be measured of better than 1 s. The directional response of the nGEM to neutrons is a key to reducing the scattering contribution to the measured neutron flux. First results achieved using small size nGEM prototypes shows that these detectors own the directionality property and that experimental results are in agreement with MCNP simulation. In addition they have a neutron efficiency detection of about $2 \cdot 10^{-5}$ and their response scales linearly following the intensity of the neutron flux.

KEYWORDS: ITER-NBI, neutrons, GEM detectors.

*Corresponding author.

Contents

1. Introduction	1
2. CNESM Principle	2
2.1 nGEM Detector: Principle of Operation	3
3. CNEMS Model Simulation	3
3.1 nGEM response simulation	5
4. nGEM Prototypes test	6
4.1 Directionality capability measurements	6
4.2 nGEM Neutron efficiency measurement	8
4.3 Neutron intensity scan measurement	8
5. Conclusions	11
6. Acknowledgement	11

1. Introduction

SPIDER [1],[2] is a beam test facility to be hosted at the Consorzio RFX site in Padua, Italy. It represents the first step towards the full scale demonstration of the feasibility of the deuterium beam injectors for the ITER fusion experiment [3].

The main goal of this prototype is to prove the capability to generate a one hour long D^- beam pulse at the current level required by ITER but with a reduced beam energy (up to 100 keV). The 100 keV deuterons will be dumped against a target (the beam dump) tilted by 30° relatively to the beam axis (Fig. 1). The beam dump is a rectangular panel made of CuCrZr-alloy water-cooled hypervaportrons with an elemental composition of about 99% Cu.

The SPIDER D^- beam is composed of beamlets in a matrix arrangement. Their dimensions at the dump surface are $40 \times 22 \text{ mm}^2$. The total beam current of 40 A is spread out over a surface of $\approx 1 \text{ m}^2$ for a reference average current density of 40 A/m^2 and deuterium flux of $2.5 \times 10^{20} \text{ D/m}^2\text{s}$.

The neutron production due to fusion reactions between beam deuterons and deuterons implanted in the dump will be a few times 10^{15} neutrons per SPIDER pulse. The neutron source intensity is suitable for diagnostic applications.

In this paper a neutron diagnostic designed to provide the map of the beam intensity with a spatial resolution approaching the size of individual beamlets is described. The system uses nGEM neutron detectors. These are Gas Electron Multiplier detectors equipped with a cathode that also serves as neutron-proton converter foil. The cathode is designed to ensure that most of the detected

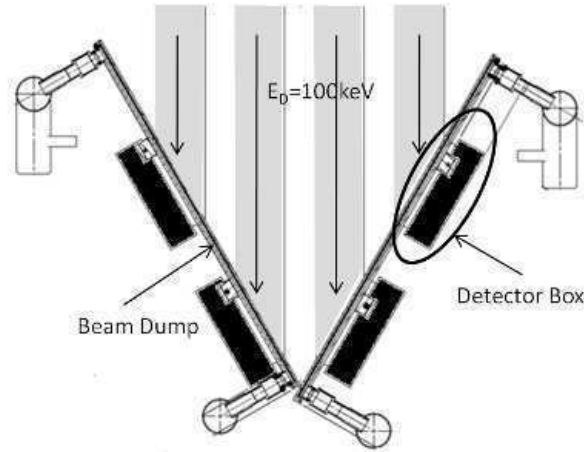


Figure 1. Schematics of the SPIDER beam dump. The beam dump is tilted by 30 degrees relative to the beam axis. The CNESM detectors (black) are placed right behind the beam dump.

neutrons at a point of the nGEM surface are emitted from the corresponding $40 \times 22 \text{ mm}^2$ beamlet footprint on the dump front surface. Results achieved using small size nGEM prototypes in terms of measurements of directionality capability, neutron detection efficiency and response to different neutron fluxes are reported in this paper.

2. CNESM Principle

The proposed detection system is called Close-contact Neutron Emission Surface Mapping (CNESM). It is placed right behind the beam dump (see Fig. 1), as close as possible to the neutron emitting surface. A small distance (about 30 mm) between the diagnostic system and the beam dump is crucial in order to provide the map of neutron emission on the beam dump surface with good spatial resolution.

The detectors to be used in this diagnostic system are nGEM detectors [4]. These are Gas Electron Multiplier (GEM) detectors [5] equipped with a solid-state, fast neutron converter cathode, similarly to what is done for detection of 14 MeV neutrons from fusion plasmas [6]. The goal of each nGEM detector is to map the neutron emission from a group of 5×16 beamlets: populating the total beam dump surface would require a total of 16 nGEM detector units (area $35.2 \times 20 \text{ cm}^2$). Since the GEM detectors operate at room pressure, they are placed inside a steel containment box connected to the outside of the SPIDER vacuum vessel by one pipe containing the electrical cables and the gas pipes feeding the gas mixture into the nGEM chambers.

A triple-GEM detector arrangement [7] will be used in CNESM. The readout pads will be arranged so as to have two pads (area $20 \times 22 \text{ mm}^2$) per beamlet footprint, for a total of 160 readout channels. Cost-effective readout electronics is available and can indeed manage hundreds of readout channels. The front-end chips that will be used to readout all the pads are the CARIOCA-GEM digital chips [8].

2.1 nGEM Detector: Principle of Operation

The principle of operation of the nGEM detector is shown in Fig 2. The cathode of a nGEM detector is composed by two layers: one polyethylene (CH_2) film and one Aluminum layer. The raw material of the cathode is constituted by an aluminum polyethylene sheet nominally $100 \mu\text{m}$ thick. Precise measurements only of the aluminum layer thickness found a mean thickness of $39 \pm 2 \mu\text{m}$: as a consequence the average CH_2 thickness is around $61 \mu\text{m}$. Incoming neutrons have an energy E_n between 2.45 and 2.85 MeV, depending on the emission angle and are converted into protons by elastic recoil in the thin polythene (CH_2) film. Protons leaving the CH_2 film with enough energy can cross the Al foil and reach the gas, thus ionizing it. The drift gas effective thickness (3 mm wide) is narrower than the proton range: only a fraction of the proton energy is deposited in the gas and detected. Primary electrons freed by interacting protons are then drifted to the GEM foils where they are multiplied [9]. The signal (around 50-100 ns duration) generated by the movement of primary and secondary electrons is induced on a padded anode that is connected to the front end electronics.

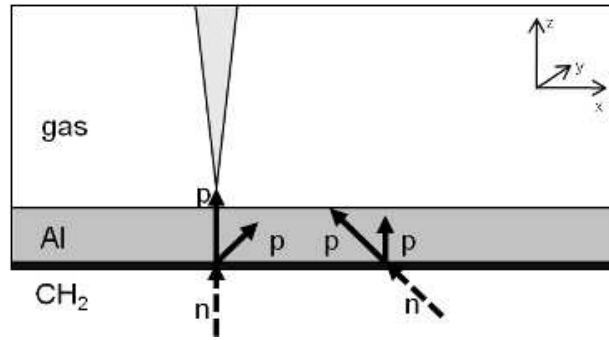


Figure 2. Illustration of how the Al cathode thickness can be used to suppress detection of neutrons with oblique incidence. Neutrons are converted into protons in the polyethylene foil (black). Only one of the four protons in the figure crosses the Al foil (grey) and ionizes the gas, thus liberating primary electrons and generating a detectable signal.

Since the planar neutron source to be mapped is at some distance from the detection surface, better spatial resolution is achieved if the trajectory of the detected neutrons is not too far from being perpendicular to the cathode surface. Figure 2 illustrates how this is achieved by suitable choice of the Al foil thickness: the $40 \mu\text{m}$ thick Al foil stops all protons with a recoil angle $\theta_p > 45^\circ$ and/or with a recoil energy $E_p < 2.1 \text{ MeV}$ ($E_p = E_n \cos^2 \theta_p$). This directional response of the nGEM cathode to neutrons is beneficial also for rejecting neutrons reaching the cathode after scattering off the beam dump structure.

3. CNEMS Model Simulation

CNESM was designed on the basis of simulations of the different steps, from the deuteron beam interaction with the beam dump to the neutron detection in the nGEM. Deuterium beam interaction was simulated using the TRansport of Ion in Matter (TRIM) code [10]: trajectories of 10^6

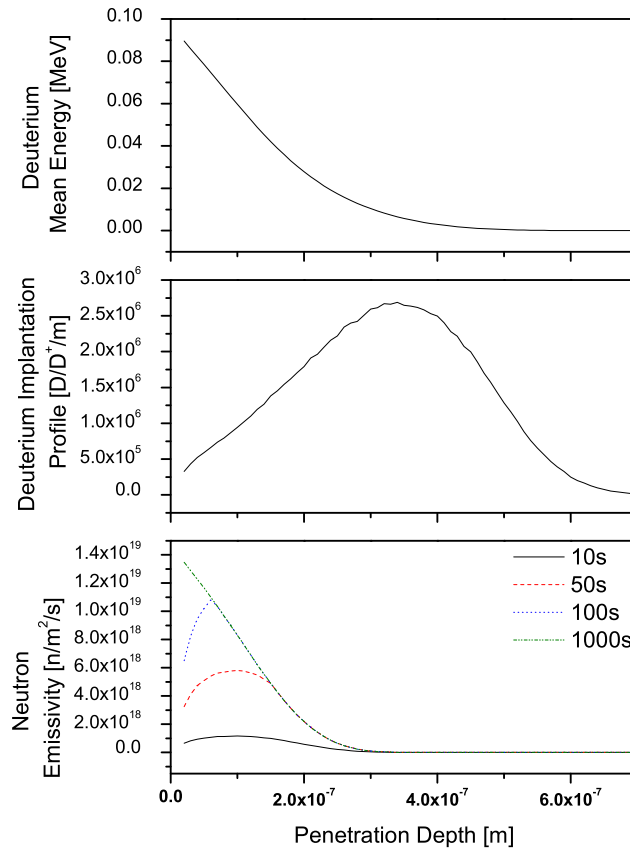


Figure 3. TRIM calculation of deuteron energy (top), deuterium implantation profile (middle) and neutron emissivity at different times (bottom) as a function of penetration depth.

deuterium ions with an initial energy $E_0=100$ keV and incidence angle equal to 60° relative to the normal to the CuZrZr-alloy beam dump have been simulated.

At least 95% of the deuterons penetrate (by up to $0.8 \mu\text{m}$) in the beam dump and will contribute to the neutron emission. The TRIM result was used to determine average deuterium energy and deuteron deposition rate as function of penetration depth (see Fig. 3). The latter was used to calculate the (time dependent) deuterium concentration using a so-called Local Mixing Model [11] whereby deuterium migration in the copper alloy is neglected and a local saturation value of 20% [12] is assumed for the deuterium concentration.

Neutron emissivity as function of penetration depth (see Fig. 3 bottom) was then calculated as $y=\Phi\sigma n_D$, where Φ is the deuterium flux, σ is the energy-dependent $D(d,n)^3\text{He}$ fusion cross section and n_D represents the implanted deuterium density. A more interesting quantity is the neutron brightness of the source, that is the line integral of the emissivity over the penetration depth. The brightness reaches a saturation value of about $1.4 \cdot 10^{12}$ n/(m^2 s) 2-3 minutes after switching on the beam.

The effect of the anisotropy of the fusion reaction cross section is to peak the neutron emission

along the deuteron beam direction: it results in a shift of the neutron field at the detection surface of about 10 mm compared to the ideal case of isotropic neutron emission described before, and can be taken into account in the simulations.

Neutron transport effects in the beam dump were investigated using the MCNPX code [13]. The beam dump model used for the simulation is made of two CuCrZn alloy layers and a layer of water in between; the layer thicknesses were chosen in order to reproduce the mass ratio of the cooling water and the copper alloy. About 10% of all neutrons with energy $E_n > 2\text{MeV}$ arriving at the nGEM detection surface do so after scattering at least once in the beam dump. Since the direction of scattered neutrons tends to be isotropic they are to a large extent rejected as a result of the directional response of the nGEM cathode. We conclude that neutron transport effects are not expected to perturb the measurement in a significant way.

3.1 nGEM response simulation

The energy spectrum deposited (E_{dep}) in the nGEM gas was also investigated with a MCNP model of the detector. A monoenergetic ($E_n=2.7\text{ MeV}$), monodirectional point neutron source was placed at a distance $d=30\text{ mm}$ from the cathode. The cathode was modeled as a slab composed by a $60\text{ }\mu\text{m}$ thick polyethylene film (CH_2), a $t \approx 40\text{ }\mu\text{m}$ thick Al foil and a 3 mm GEM gas mixture of Argon (45%), CO_2 (15%), CF_4 (40%). The resulting energy deposition spectrum is shown in Figure 4 for different neutron incidence angles θ_n . The overall signal intensity drops to almost zero for $\theta_n > 45^\circ$ confirming the directional response of the nGEM cathode to neutrons.

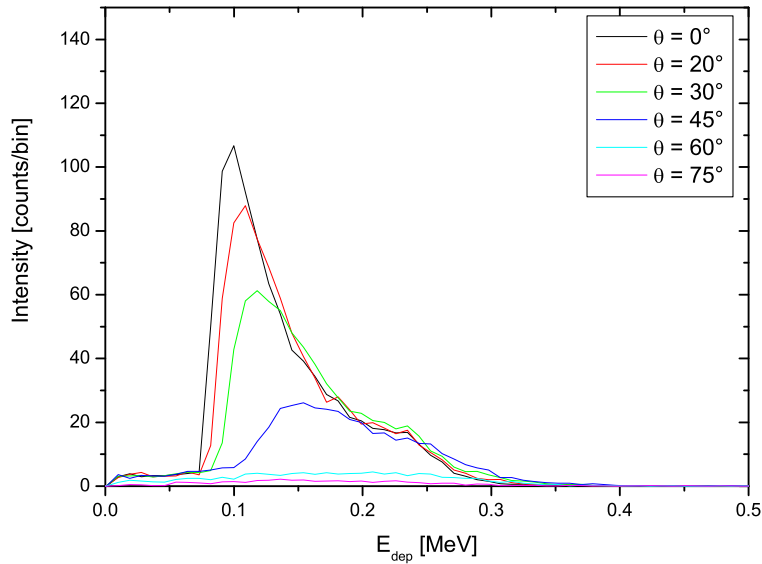


Figure 4. Simulated distribution of the energy deposited by protons inside the nGEM gas for different neutron incident angles θ_n . The thickness of the Al foil was $t=38\text{ }\mu\text{m}$. The intensity is per unit neutron source. The bin width is 10 keV.

The energy spectrum rises sharply above $E_{dep}=90$ keV and drops above $E_{dep}=240$ keV. The detailed shape of the distribution within this energy range can be explained considering that the energy loss in the Al foil is a decreasing function of the proton energy and that the range of the most energetic protons exceeds the GEM gas thickness. The result is that higher energy protons deposit less energy in the gas, whereas the maximum deposited energy is achieved by lower energy protons that have a range matching the GEM gas thickness. We can therefore interpret the spectral shape as due to two main components: on the low energy side there is a peak due to energetic protons (dominant for lower neutron incidence angles) while on the high energy tail of the distributions there is the second component due to lower energy protons (dominant for larger incident angles).

The spatial resolution of the measurement is mainly limited by the width (FWHM) of the spatial distribution of recorded events on the nGEM cathode in response to a point neutron source on the beam dump surface. We consider here the width along the X-axis (see Figure 2). A limit case is one of unperturbed propagation of the neutrons from the point source. In this case the intensity at the cathode would have a $1/(x^2+d^2)$ dependence and the FWHM value of about 60 mm would exceed the beamlet dimension (40 mm). The effect of the directional detector response due to the Al foil is to decrease the FWHM value to about 30 mm. This level of spatial resolution is adequate for unfolding the neutron source intensity from the 2D event map in the nGEM detector.

4. nGEM Prototypes test

Two small area (10×10 cm²) nGEM prototypes have been realized and tested using 2.5 MeV neutrons at the FNG (Frascati Neutron Generator) [14] located in Frascati in Italy (see Fig. 5 and Fig. 6). These are triple GEM detectors equipped with the CH₂ (61 μm) + Al (39 μm) converter cathode. The gaps geometry of these detectors is the same as the one used in Triple GEM LHCb detectors [15] currently installed into LHC at CERN (Drift / Transfer 1/ Transfer 2/ Induction = 3 mm / 1 mm / 2 mm / 1 mm). Both detectors were operated using a gas mixture of Ar/CO₂/CF₄ 45%/15%/40%. The high voltage configuration was generated using the HVGEM [16] NIM module and the potentials were applied to each electrode by means of passive resistive-capacitive filters properly designed for a Triple GEM detector.

The first prototype (hereby called “analog” prototype) has 128 readout pads but just one of these pads is read out using a standard pre-amplifier (Ortec 142 IH), amplifier (Ortec 474), MCA (Ortec Maestro32) chain in order to get pulse height spectra as outputs.

The second one (hereby called “digital” prototype) has all the 128 pads readout by 16 CAR-IOCA chips and is able to measure the counting rate of the detector. All the CARIOCAs are then connected to a custom made FPGA Mother Board [17] that analyzes the LVDS signal coming from the chips. The digital prototype is a complete small version of the full size area nGEM for SPIDER.

4.1 Directionality capability measurements

Since pulse height spectra are needed to measure nGEM directionality properties, the analog detector was employed in this exercise. In order to be able to detect neutrons and to be insensitive to photons, the following electrical configuration was applied to the device: E_d (Drift Field) = E_{T1} (Transfer 1 Field) = E_{T2} (Transfer 2 Field) = 3 kV/cm, E_{Ind} (Induction Field) = 5 kV/cm and $V_{GEM} = \Sigma \Delta V_{GEM} = 970$ V. This configuration corresponds to an effective gain that is about 96.



Figure 5. Analog nGEM prototype installed in the FNG bunker close to the neutron gun.

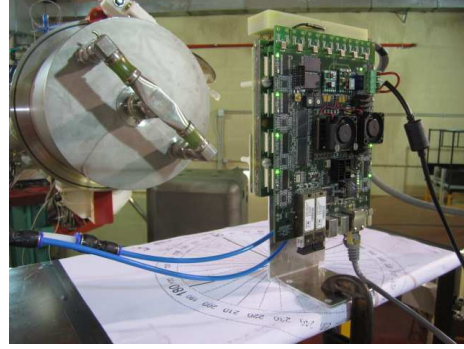


Figure 6. Digital nGEM prototype installed in the FNG bunker close to the neutron gun.

Directionality capability of this small size detector prototype was measured using a 10^8 n/(cm²·s) flux of 2.5 MeV neutrons. The neutron flux is continuously monitored by a NE213 scintillator. The chamber was precisely aligned with the center of the target of the neutron generator and several PH spectra were acquired in order to measure the neutron flux stability (around 5%). The detector was successively tilted (θ_{GEM}) by 10, 20, 30, 45, 60 and 90° with respect to the axis of the neutron generator and a pulse height spectrum was acquired for each tilt angle. Each pulse height spectrum was normalized considering the total number of neutrons generated by the neutron gun measured by the NE213 scintillator. Fig 7 shows the results.

The rising edge on the left is due to the low level discriminator threshold applied in order to filter the electronic noise. Up to a value of 30°, no significant change in the pulse height shape and area is detectable. On the other hand for values of $\theta_{GEM} > 45^\circ$, the counting rate drops suddenly and falls to almost zero for $\theta_{GEM} = 90^\circ$. When the chamber is tilted by an angle $\theta_{GEM} = 90^\circ$, the converter cathode is parallel to the neutron beam except for the effect of beam divergence and small alignment errors: as a consequence almost no interaction between neutron and polyethylene layer is expected and the corresponding measurement can be interpreted as a measurement of the background.

Figure 8 shows the comparison for $\theta_{GEM} = 0^\circ$ between the MCNPX simulated PH spectra for three different aluminum thicknesses (33, 38 and 43 μm) and the measured one.

The difference in the rising edge could be explained by the fact that the experimental data are cut by the discriminator threshold: as a consequence the comparison should be limited to the energy range on the right hand side of the dashed line. In this range all simulations provide a good match to the measured PH spectrum.

In order to measure the directionality capability, PH spectra have been integrated over the threshold represented by a dashed line in Fig 8 corresponding to the experimental data peak. Figure 9 shows the normalized integrated counts under the PH spectra for the experimental and the simulated data.

The measured counts corresponding to $\theta_{GEM} = 90^\circ$ have been subtracted from all the other PH spectra. Both experimental and simulated data have been normalized by dividing each point by the corresponding integrated PH area at $\theta_{GEM} = 0^\circ$.

Both experimental counts and simulated data for $t_{Al} = 38 \mu\text{m}$ are reduced to about 80% of

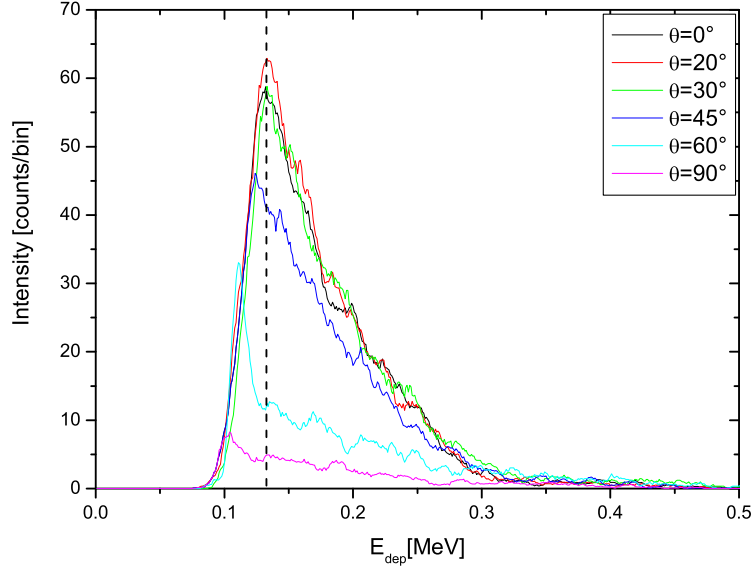


Figure 7. Measured PH spectra at different tilt angles with respect to the neutron generator axis. The bin width is 10 keV. The value of the threshold used to perform PH spectra integration is shown as a dashed line. $V_{GEM} = 970$ V; E_d (Drift Field) = E_{T1} (Transfer 1 Field) = E_{T2} (Transfer 2 Field) = 3 kV/cm, E_{Ind} (Induction Field) = 5 kV/cm; Gas Mixture Ar/CO₂/CF₄ 45%/15%/40%. 1 Pad 12x6 mm² area

the initial value for $\theta_{GEM} = 45^\circ$ while, in the case of $t_{Al} = 43 \mu\text{m}$ and $t_{Al} = 33 \mu\text{m}$, 80% of the initial value is reached respectively for an angle of about 30 and 50 degrees: the $t_{Al} = 38 \mu\text{m}$ simulations is able to reproduce the experimental data. This result confirms the measurement of the bare aluminum layer that reported a value of $39 \pm 2 \mu\text{m}$.

4.2 nGEM Neutron efficiency measurement

The nGEM neutron detection efficiency was measured using the digital prototype since a precise measurement of the nGEM counting rate is necessary. Fig. 10 shows the result of this measurement.

In the plot, two trends can be clearly distinguished: the first one ($V_{GEM} < 1010$ V) is due only to neutron detection while the second one ($V_{GEM} > 1010$ V) is due also to photon detection. This result is consistent with what was measured in [18]: in order to be completely insensitive to gamma rays V_{GEM} should be kept around 970 V. At this V_{GEM} value a neutron detection efficiency of about $2 \cdot 10^{-5}$ was measured.

4.3 Neutron intensity scan measurement

The digital prototype was also employed in the measurement of the nGEM response to different neutron flux intensities as measured by NE213 scintillator. Fig 11 shows the measured nGEM counting rate as a function of the neutron flux on the detector.

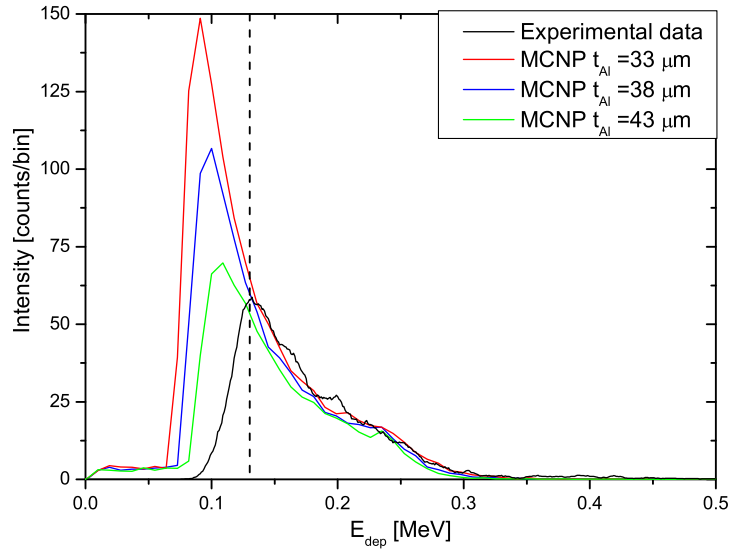


Figure 8. Comparison between the $\theta = 0^\circ$ spectrum of Fig. 7 and MCNP simulated energy deposition spectra for three different aluminum thicknesses and CH_2 thickness = $60 \mu\text{m}$). The bin width is 10 keV. The value of the threshold used to perform PH spectra integration is shown as a dashed line.

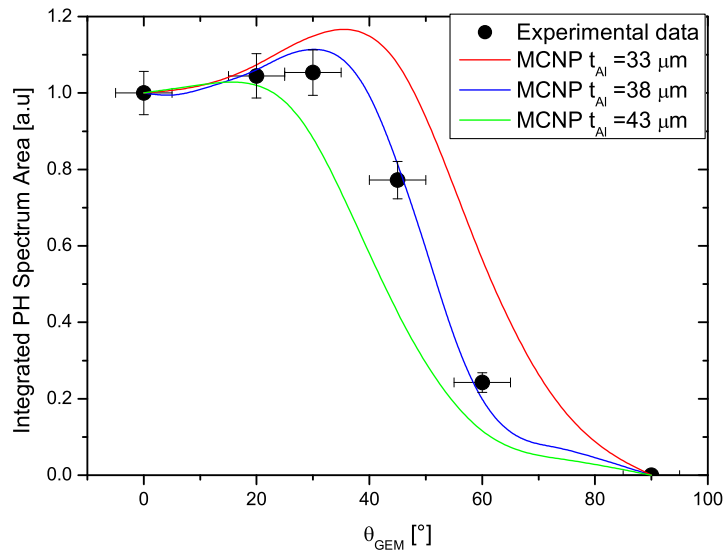


Figure 9. Normalized integrated PH area over threshold shown in Fig. 8 as a function of the tilt angle: comparison between measurements and three MCNP simulations at three different aluminum thicknesses.

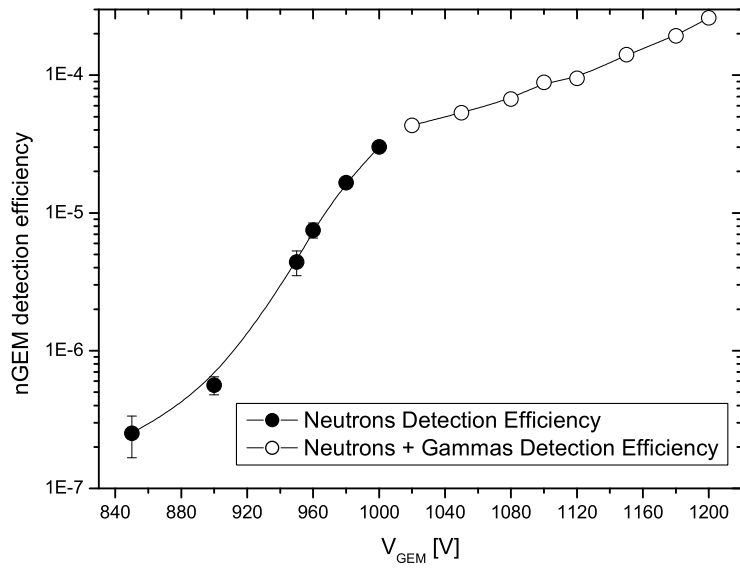


Figure 10. Neutron detection efficiency as a function of V_{GEM} ; $E_d = E_{T1} = E_{T2} = 3$ kV/cm, $E_{Ind} = 5$ kV/cm; Gas Mixture Ar/CO₂/CF₄ 45%/15%/40%.

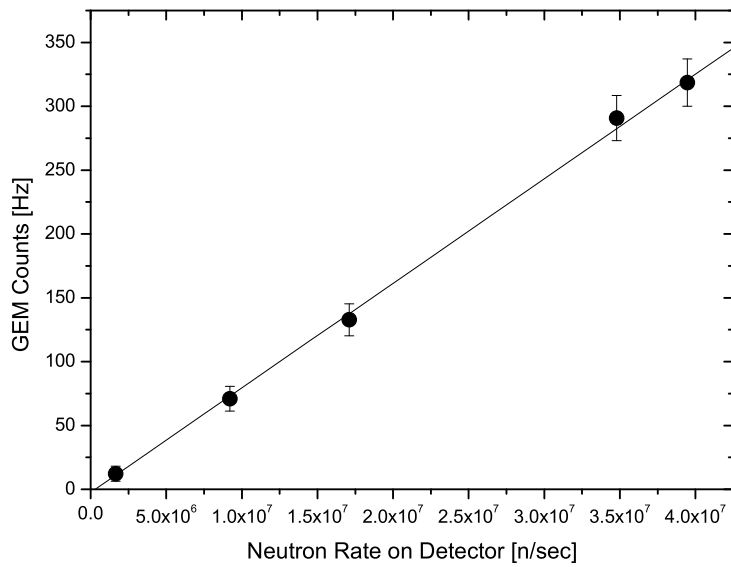


Figure 11. nGEM response as a function of the intensity of neutron flux on the detector; $V_{GEM} = 1020$ V; $E_d = E_{T1} = E_{T2} = 3$ kV/cm, $E_{Ind} = 5$ kV/cm; Gas Mixture Ar/CO₂/CF₄ 45%/15%/40%.

The efficiency measured using the slope of the fitted line is about $2 \cdot 10^{-5}$. The nGEM counting rate scales linearly with the intensity of the neutron beam. This is an essential feature in order to use a nGEM detector as a fast neutron beam monitor in the CNESM diagnostic system.

5. Conclusions

The proposed CNESM detection system was designed in order to meet the goal of providing the map of the neutron emission on the beam dump surface of the SPIDER facility. This is achieved by using nGEM detectors equipped with a cathode designed for detection of neutrons of energy $E_n > 2.1$ MeV with an incidence angle $\theta < 45^\circ$. CNESM was designed on the basis of simulations of the different steps from the deuteron beam interaction with the beam dump to the neutron detection in the nGEM and it will provide beam images with a spatial resolution matching the SPIDER beamlet footprints and a time resolution < 1 s.

First results achieved using small size prototypes show that these detectors possess the required directionality property and that experimental results are in agreement with MCNP simulations. In addition they have a neutron efficiency detection of about $2 \cdot 10^{-5}$, their response scales linearly with the intensity of the neutron flux and, by proper setting of the effective gain, they are insensitive to gamma rays.

CNESM is a first step towards the application of this diagnostic technique to the MITICA beam test facility, where it will be used to resolve the horizontal profile of the beam intensity. The main difference between SPIDER and MITICA is the x100 larger neutron fluxes expected. This requires a reassessment including further tests of the radiation hardness of the signal readout electronics. The beam energy of 1 MeV and the grazing incidence of the beam with a tilt angle of the beam dump of about 6° are further differences that will require a careful optimization of the nGEM detectors features.

6. Acknowledgement

The support of the FNG team of ENEA (Frascati) is gratefully acknowledged. This work was set up in collaboration and financial support of F4E.

References

- [1] P. Sonato, V. Antoni, M. Bigi, G. Chitarin, A. Luchetta, D. Marcuzzi, R. Pasqualotto, N. Pomaro, G. Serianni, V. Toigo, P. Zaccaria and NBI International team, *Design development of SPIDER and MITICA experiments, prototypes of the ITER neutral beam injectors*, 14th International conference on ion sources (ICIS), Conference Proceeding
- [2] R Pasqualotto, G. Serianni, P. Sonato, M. Agostini, M. Brombin, M. Dalla Palma, M. De Muri, E. Gazza, G. Gorini, N. Pomaro, A. Rizzolo, M. Spolaore, and B. Zaniol, *Diagnostic of the ITER neutral test beam facility*, 14th International conference on ion sources (ICIS), Conference Proceeding
- [3] R. Hemsworth, H. Decamps, J. Graceffa, B. Schunke, M. Tanaka, M. Dremel et Al., *Status of the ITER heating neutral beam system* 2009 Nucl. Fusion 49 045006

- [4] Paolo Valente, Giovanni Corradi, Fabrizio Murtas, Marco Pistilli, Diego Tagnani, Basilio Esposito, Daniele Marocco, *Triple-GEM detectors for electron, proton and neutron beam diagnostics*, Nucl. Instr. Meth. A: Available online 20 July 2010, ISSN 0168-9002, 10.1016/j.nima.2010.06.319.
- [5] F. Sauli, *GEM: A new concept for electron amplification in gas detectors*, Nucl. Instr. and Meth. A: Volume 386, Issues 2-3, 21 February 1997, Pages 531-534, ISSN 0168-9002, 10.1016/S0168-9002(96)01172-2.
- [6] M. Tardocchi, S. Conroy, G. Ericsson, J. Frenje, J. Källne, E. Traneus, *The monitoring system of a high performance fusion neutron spectrometer* Nucl. Instr. and Meth. A Volume 485 (2002) 624.
- [7] S. Bachmann, A. Bressan, M. Capeáns, M. Deutel, S. Kappler, B. Ketzer, A. Polouektov, L. Ropelewski, F. Sauli, E. Schulte, L. Shekhtman, A. Sokolov, *Discharge studies and prevention in the gas electron multiplier (GEM)*, Nucl. Instr. and Meth. A: Volume 479, Issues 2-3, 1 March 2002, Pages 294-308
- [8] W. Bonivento, P. Jarron, D. Moraes, W. Riegler, F. dos Santos, *Development of the CARIOCA front-end chip for the LHCb muon detector*, Nucl. Instr. and Meth. A: Volume 491, Issues 1-2, 21 September 2002, Pages 233-243
- [9] S. Bachmann, A. Bressan, L. Ropelewski, F. Sauli, A. Sharma, D. Mörmann, *Charge amplification and transfer processes in the gas electron multiplier*, Nucl. Instr. and Meth. A: Volume 438, Issues 2-3, 11 December 1999, Pages 376-408, ISSN 0168-9002, 10.1016/S0168-9002(99)00820-7.
- [10] J.F. Ziegler, SRIM/TRIM code, available online at www.srim.org
- [11] D.K. Brice, B.L. Doyle, W.R. Wampler, *Extended local mixing model for hydrogen retention and isotope exchange*, J. Nucl. Mat., Volumes 111-112, November-December 1982, Pages 598-605,
- [12] J. Kim. Nucl. Technol., 44 (1979), p. 315
- [13] <http://mcnp-green.lanl.gov/>
- [14] M. Martone, M. Angelone, M. Pillon, *The 14 MeV Frascati neutron generator*, Journal of Nuclear Materials, Volumes 212-215, Part B, September 1994, Pages 1661-1664, ISSN 0022-3115, 10.1016/0022-3115(94)91109-6.
- [15] G Bencivenni, G Felici, F Murtas, P Valente, W Bonivento, A Cardini, A Lai, D Pinci, B Saitta, C Bosio, *A triple GEM detector with pad readout for high rate charged particle triggering*, Nucl. Instr. and Meth. A: Volume 488, Issue 3, 11 August 2002, Pages 493-502, ISSN 0168-9002, 10.1016/S0168-9002(02)00515-6.
- [16] F. Murtas, B. Buonomo, G. Corradi, G. Mazzitelli, M. Pistilli, M. Poli Lener, D. Tagnani, P. Valente, *Applications in beam diagnostics with triple GEM detectors*, Nucl. Instr. and Meth. A: Volume 617, Issues 1-3, 11-21 May 2010, Pages 237-241, ISSN 0168-9002, 10.1016/j.nima.2009.10.039.
- [17] <http://www.infn.it/csn5/joomla/GEMINI/>
- [18] B. Esposito, F. Murtas, R. Villari, M. Angelone, D. Marocco, M. Pillon, S. Puddu, *Design of a GEM-based detector for the measurement of fast neutrons*, Nucl. Inst. and Meth. A: Volume 617, Issues 1-3, 11-21 May 2010, Pages 155-157, ISSN 0168-9002, 10.1016/j.nima.2009.06.101.

Acknowledgments

Finally I would like to thank all the people that I met during these years.

I ringraziamenti sono sempre la cosa più difficile, ma allo stesso tempo più divertente da scrivere: proprio perchè devo divertirmi i ringraziamenti sono l'unica parte di questa tesi ad essere stati scritti in italiano.

Non è facile decidere l'ordine con cui ringraziare le persone ma credo che la prima persona debba essere il mio supervisore, il Prof. Giuseppe Gorini. Grazie di avermi dato la possibilità di svolgere questa tesi, di avermi introdotto nel mondo dei neutroni e di aver facilitato il mio ingresso in un gruppo di cui fino a tre anni fa non conoscevo nemmeno l'esistenza. Grazie per gli insegnamenti, per aver passato le vacanze di natale a correggere la mia tesi e per aver tradotto articoli e tesi dal *marichese* all'*inglese*... Grazie. Il secondo ringraziamento va alla mia famiglia, che da sempre mi fornisce il supporto necessario ad affrontare tutte le situazioni che mi si parano davanti. Grazie per aver avuto la pazienza di sopportarmi anche quando ero intrattabile, stanca e di pessimo umore. Grazie davvero.

Grazie a tutte le mie amiche, Esther, Valentina, Elena, Alice ed Alessandra, che dai tempi del liceo mi stanno vicine. Grazie per non perdere mai le speranze di vederci, anche se è sempre più difficile e sempre più complicato. È bello sapere che comunque vada voi ci siete! Grazie alle mie compagne di pallavolo, per le risate, per le partite, un po' vinte, un po' perse, grazie per i *post*, e spesso anche per i *pre* partita. Grazie a Manuela per le chiacchierate

su skype e per avermi accompagnato in 8 anni di fisica, anche se le nostre strade si sono separate alla fine dell'università sei sempre un'amica con cui parlare di tutto un po'.

Grazie a tutto il gruppo! Ad Enrico, per le chiacchierate sia di lavoro sia di altro, per il supporto tecnico e morale e per aver anche lui partecipato alla correzione dell'inglese di questa tesi. Grazie dei numerosi caffè che in tre anni mi hai offerto, prima o poi pareggerò il conto... Grazie a Marco, per avermi fatto conoscere il mio primo modulo CAEN...chissà come mai, ma c'era sempre una CAEN nuova da far funzionare.. Grazie per le discussioni, da cui sono sempre uscita con qualcosa in più. Grazie a Claudia, a Igor, a Roberta, a Massimo, a Gabriele, a Luca e a Carlo. Grazie a Tonino, per avermi fatto da guida ad ISIS, e per aver sempre avuto una parola di incoraggiamento. Grazie a tutti voi.

Grazie al Prof. Alberto Fazzi, per avermi, con pazienza, aiutato nello sviluppo della catena elettronica dei diamanti, grazie dei preziosi insegnamenti.

Grazie a tutto il gruppo pause del terzo piano! Cristina, Mauro, Davide, Silvia, l'Omone, Davidino e tutte le persone che ho conosciuto in Bicocca in questi tre anni...Un grazie va a Stefanino, espatriato al CERN, grazie per le consulenze informatiche, per la compagnia sul simpatico treno S11 e grazie per l'amicizia.

Infine, non per importanza, ma perchè forse è la persona più difficile e più lunga da ringraziare. Un enorme grazie va a Enzo. Grazie di tutto. Dalle prime parole scambiate sul treno alle numerosissime esperienze vissute insieme in questi due anni (e per quelle che ancora vivremo). Grazie per avuto sempre un parola di conforto, grazie per il supporto morale, per sopportare i miei lunghissimi silenzi e i miei sbalzi d'umore. Grazie perchè arrivare fino a qui non sarebbe stato così bello senza di te. Semplicemente grazie di starmi vicino!

Grazie a tutti quelli che ho nominato e anche a quelli che non ho nominato, grazie per aver reso questi tre anni un viaggio indimenticabile.